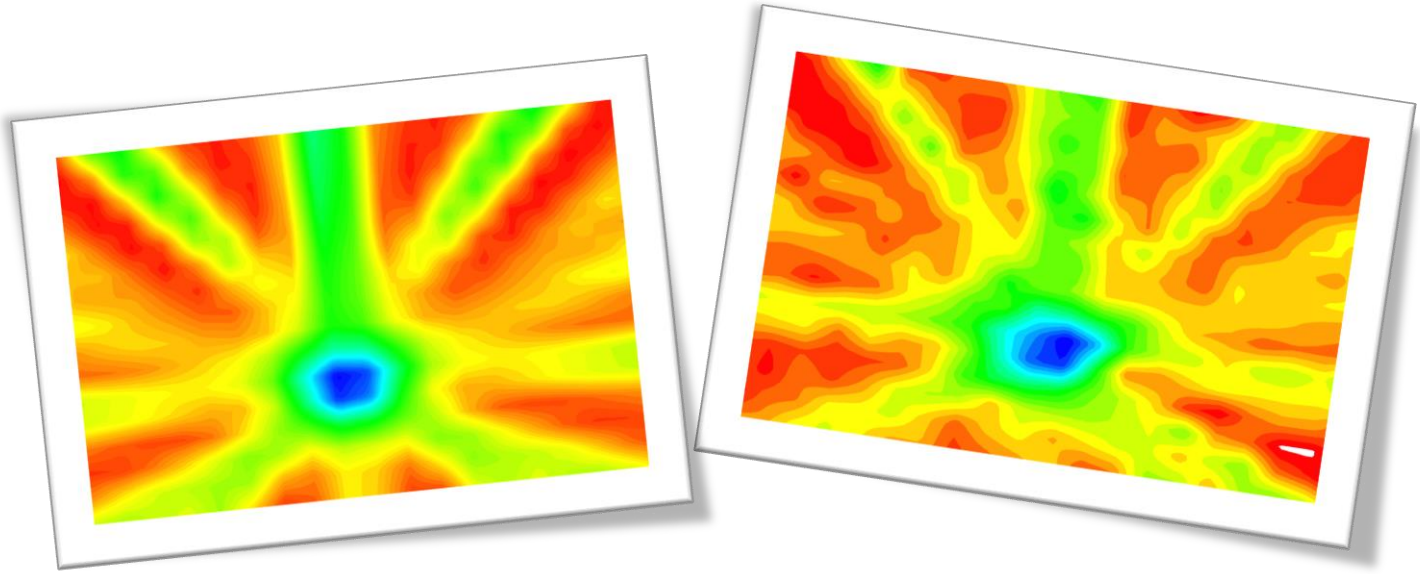

Local Structure and Magnetism of (Ga,Mn)As

Tiago Abel de Lemos Lima
Integrated Masters in Engineering Physics
Department of Physics and Astronomy
2014

Advisor
João Pedro Araújo, Auxiliar Professor, Faculdade de Ciências

Co-advisor
Kristiaan Temst, Associate Professor, Faculteit Wetenschappen, KULeuven

All corrections were determined by the Jury, and only those where performed.

President of the Jury,

Porto, / /

Acknowledgments

"Sure as I am breathing
Sure as I'm sad
I'll keep this wisdom in my flesh
I leave here believing more than I had
And there's a reason I'll be, a reason I'll be back"

– No Ceiling, *Into the Wild*, Eddie Vedder

My MSc ran on more than just the love for physics. A fiery, unbelievable chain of events led me to experience one of the best times in my life so far. Some years back I wouldn't even believe I would be writing this paragraph in CERN, the most fascinating place for physics research in Europe, if not in the world. All this I owe to the people I acknowledge here and to whom I am very, very grateful.

First of all I have to thank my supervisors, Lino and João Pedro, who gave me a fantastic opportunity to move forward in my professional and personal life. All I know about being a physicist I owe it to you, the practical and the theoretical aspects of it, along with all the struggling and failing required for achieving our goals. As in magnetism, some kind of interaction is required for a magnetic state to emerge. Be it through a short-distance mechanism or through a long-distance one, there will always be a regime in which we can achieve such a state. In short, thank you for letting me into this scientific family.

I also must thank Kristiaan Temst and André Vantomme for incorporating me into their research group at the Instituut voor Kern- en Stralingfysika, KULeuven, Ulrich Wahl for the fruitful insights on the Emission Channeling technique and its intricate theoretical framework, and the EC/ISOLDE collaboration team for providing me the opportunity to dwell into the technical parts behind the technique. Also, a big thanks to my office colleagues at the IKS, Valérie, Koen and Nuno for the friendship and all the help with experimental and analysis procedures, as well as for the ever so useful coffee breaks.

None of this would've been possible without the support of my friends. Those who grew up in physics with me, specially João and Mafalda, who shared the international experience with me, but also José Valente, Diogo and Artur; thank you all for the incredible moments, useful insights, homework, studying, stressing, despairing and achieving. You made me strive and fight for what I love in science. A very deep and grateful thank you to Máximo (Filipe), who was always by my side and helped me in every personal aspect of my life. Also David, Armando, Artur, Dora and Daniela, and all my other national and international friends, thank you for all the laughs and good times as well as the fantastic experiences.

O maior agradecimento devo à minha família. Ao meu pai, mãe, irmão e irmãs devo aquilo que sou, pela confiança que sempre têm em mim; por todo o carinho, amor e saudade, e apoio incondicional, mesmo quando isso envolve estar longe de vocês. Com vocês aprendi a encarar a vida com um sorriso na cara e a tirar partido de todos os momentos da minha vida. E aprendi algo ainda mais importante: a união e o amor conseguem superar qualquer limitação. Muito, muito obrigado!

I am mostly grateful to my family, for their trust, care and love, as well as their unconditional support, even when it involved me staying away from you. You taught me to experience life with a smile in my face, enjoying every little and simple moment. With you I learned that love and unity can overcome any limitation. Thank you so much!

As *Paulo Coelho* says in *The Pilgrimage*, *"the boat is safer anchored at the port; but that's not the aim of boats"*, my last and deepest appreciation goes to the person that ultimately made me lift my anchor and set sail. Jana, with you I learned that no distance is large enough and no time is long enough when the wait is worth the price. These last months were filled with work but also with art and music, cuisine and cocktails, trips and tumbles... A compendium of happiness and love in every little moment we shared, and for which I am very grateful. Let's keep sailing together.

They say that sometimes you have to skip a beat to find your rhythm, especially if, like me, you tend to lose it easily. And we all know that the best songs don't have only one rhythm... Keeping many rhythms is likely to be a challenge, but in the end if you don't play the song, who will?

Tiago

September 2014

Abstract

Throughout the years, dilute magnetic semiconductors (DMS) have emerged as promising materials for semiconductor-based spintronics. In particular, (Ga,Mn)As has become the model system in which to explore the physics of carrier-mediated ferromagnetism in semiconductors and the associated spintronic phenomena, with a number of interesting functionalities and demonstrated proof-of-concept devices. It constitutes the perfect example of how the magnetic behavior of DMS materials is strongly influenced by local structure.

In this thesis, we address key aspects of the interplay between local structure and ferromagnetism of (Ga,Mn)As. We unambiguously identify the lattice site occupied by interstitial Mn as the tetrahedral interstitial site with As nearest neighbors T_{As}. We show, furthermore, that the T_{As} is the most energetically favorable site regardless of the interstitial atom forming or not complexes with substitutional Mn. We also evaluate the thermal stability of both interstitial and substitutional Mn sites occupied by Mn for two representative Mn concentrations (1% and 5%), and its influence on the material's structure and magnetism. We show that compared to the substitutional Mn, interstitial Mn becomes mobile at lower temperatures, for both low (1%) and high (5%) Mn concentration. Moreover, the diffusion temperatures are lower for the high concentration than for the low concentration case. These diffusion temperatures are concentration dependent, with aggregation of impurities occurring for the high concentration at lower temperatures than for the low concentration. These findings translate into two key conclusions: at typical growth temperatures (200-300°C) the interstitial Mn is mobile for high concentration (5%) but not for low concentration (1%); and substitutional Mn impurities become mobile in a temperature regime that is well below what has been previously reported. We also observe a decrease in the activation energy for the diffusion of both substitutional and interstitial impurities with increasing Mn concentration. This decrease has a different origin for each case: for substitutional diffusion, with activation energies of 2.3-2.6 eV at 1% Mn to 1.9-2.0 eV at 5% Mn, a vacancy-assisted mechanism occurs that is favored with increasing impurity concentration; for interstitial diffusion, with activation energies of 1.5-2.1 eV at 1% Mn to 1.3-1.8 eV at 5% Mn, as charge screening effects become stronger with increasing Mn (and consequently carrier)

concentration, interstitial Mn defects are effectively “neutralized”, and therefore experience lower migration barriers. Additionally, we conducted a comprehensive study of the local structure and magnetism in the different diffusion regimes. We show that annealing at 200°C promotes the passivation of the interstitial Mn for 5% Mn (Ga,Mn)As, as an increase in T_C and magnetization is observed. No improvement is observed in the 1% Mn case, which can be understood from the absence of interstitial impurities incorporated during growth for this concentration regime. Annealing at 300°C induces the precipitation of Mn into Mn-rich regions for both concentrations studied, with no signs of ferromagnetism. Finally, annealing at 600°C led to the formation of well-defined secondary-phases in both concentrations, consistent essentially of superparamagnetic MnAs nanoclusters of two types: zincblende and hexagonal NiAs-type.

The results presented in this thesis are direct evidence for the complex interplay between the local structure and the carrier-mediated ferromagnetism present in this DMS system. It constitutes an important step in the understanding of the fundamental physics behind (Ga,Mn)As, motivating a wider investigation of other dilute magnetic semiconductors within the III-Mn-V family.

Key-words

Dilute magnetic semiconductors; GaAs; Mn; Emission Channeling; local structure; magnetism; ferromagnetism; superparamagnetism; secondary-phase; clusters; doping; impurities; lattice location; phase-segregation; diffusion; X-ray diffraction; extended X-ray absorption fine structure; magnetometry.

Resumo

Ao longo dos anos, semicondutores magnéticos diluídos (DMS) aparecem como materiais promissores para a spintrónica baseada em semicondutores. Em particular, (Ga,Mn)As tornou-se o sistema modelo no qual explorar a física do ferromagnetismo mediado por portadores de carga em semicondutores e entre outros fenómenos associados à spintrónica, com uma panóplia de funcionalidades interessantes e dispositivos prototípicos. Este material constitui o exemplo perfeito de como o comportamento magnético de materiais DMS é fortemente influenciado pela sua estrutura local.

Nesta tese, abordam-se aspetos sobre a interação entre a estrutura local e o ferromagnetism do (Ga,Mn)As. Em primeira mão, identifica-se inequivocamente a posição ocupada pelo intersticial de Mn na rede cristalográfica como sendo uma posição intersticial coordenada tetraedricamente por átomos de As T_{As}. Mostra-se, ainda, que esta posição T_{As} é a posição mais energeticamente favorável, independentemente do interstitial formar complexos com o substitucional ou não. Em segunda mão, averigua-se a estabilidade térmica das impurezas de Mn em ambas as posições substitucional e intersticial para duas concentrações representativas (1% and 5%). Verifica-se que os intersticiais de Mn tornam-se móveis a temperaturas mais baixas que o substitucional, para ambas as concentrações. Por outro lado, demonstra-se ainda que as temperaturas de difusão para a mais alta concentração são inferiores às de menor concentração. Estas temperaturas de difusão são então dependentes da concentração, verificando-se que a agregação das impurezas ocorre a temperaturas inferiores para a maior concentração de Mn que para a menor. Duas conclusões chave podem ser daqui retiradas: a temperaturas típicas de crescimento deste material (200-300°C) o Mn intersticial é móvel para a alta concentração (5%) contrariamente à baixa concentração (1%); e o Mn substitucional começa a difundir num regime de temperaturas bastante inferior ao relatado na literatura. Observa-se ainda um decréscimo na energia de ativação com o aumento da concentração de Mn, para a difusão de ambas as impurezas substitucionais e intersticiais. Este decréscimo tem diferentes origens: no caso da difusão do Mn substitucional, com energias de ativação de 2.3-2.6 eV para 1% Mn e 1.9-2.0 eV para 5% Mn, o aumento de concentração favorece a difusão assistida por lacunas

de Ga; no caso da difusão do Mn intersticial, com energias de ativação de 1.5-2.1 eV para 1% Mn w 1.3-1.8 eV para 5% Mn, o aumento da concentração (e consequentemente dos portadores de carga) favorece efeitos de blindagem elétrica (*charge screening*), em que a energia de migração do Mn intersticial decresce devido à "neutralização" da sua carga. Por último, realizou-se um estudo compreensivo sobre a estrutura local e o magnetismo em diferentes regimes de difusão. Mostra-se que um recozimento térmico a $200°$C leva à passivação do Mn interstitial no caso da maior concentração de Mn (5%), através do aumento da T_C e da magnetização. Tal aumento não ocorre para concentração de 1% de Mn, devido à ausência de Mn intersticial incorporado durante o crescimento das amostras neste regime de concentrações. Realizando um recozimento térmico à temperatura de $300°$C verifica-se uma precipitação das impurezas em regiões ricas em Mn em ambas as concentrações estudadas, aniquilando o ferromagnetismo. Uma última temperatura de recozimento térmico foi realizada a $600°$C, na qual se verifica a formação de fases secundárias bem definas em ambas as concentrações. Estas fases secundárias consistem essencialmente em aglomerados de MnAs superparamagnéticos de dois tipos: zincblende e hexagonal do tipo NiAs.

Os resultados apresentados nesta tese são prova direta das complexas interações existentes entre a estrutura local e o ferromagnetismo mediados por portadores de carga presentes neste semicondutor magnético diluído. Consistem assim num passo importante na compreensão dos princípios físicos fundamentais por detrás do (Ga,Mn)As e motivam uma investigação mais abrangente direcionada a outros semicondutores magnéticos diluídos semelhantes, dentro da família dos III-Mn-V.

Palavras-chave

Semicondutores magnéticos diluídos; GaAs; Mn; Emission Channeling; estrutura local; magnetismo; ferromagnetismo; superparamagnetismo; fases secundárias; aglomerados; dopagem magnética; impurezas; lattice location; segragação de fase; difusão; difração de raios-X; espectrografia de absorção de raios-X; magnetometria.

Contents

List of Figures

List of Tables

Glossary

ADF	Annular dark field
CERN	Centre Européen pour la Recherche Nucléaire
DFT	Density function theory
DMS	Dilute magnetic semiconductor
DOS	Density of states
DW	Debye-Waller
EC	Emission channeling
ESRF	European Synchrotron Radiation Facility
EXAFS	Extended x-ray absorption fine structure
FC	Field cool
FET	Field effect transistor
FM	Ferromagnetic
FWHM	Full width at half maximum
GIXRD	Grazing-incidence diffraction
GMR	Giant magnetoresistance
HDD	Hard-drive disk
HRXRD	High-resolution x-ray diffraction
IB	Impurity band
LED	Light emitting diode
LT-MBE	Low-temperature molecular beam epitaxy
MIT	Metal-to-insulator transition
MTJ	Magnetic tunnel junction
NRA	Nuclear reaction analysis
NN	Nearest neighbor
PIXE	particle-induce x-ray emission
RBS	Rutherford backscattering
RKKY	Ruderman-Kittel-Kasuya-Yosida
SQUID	Superconducting quantum interference device

SP	Secondary-phase
SPM	Superparamagnetic
SR-XRD	Synchrotron radiation x-ray diffraction
STEM	Scanning transmission electron microscopy
TEM	Transmission electron microscopy
XAFS	X-ray absorption spectroscopy
XAFS	X-ray absorption fine structure
XRD	X-ray diffraction
ZB	Zincblende
ZFC	Zero-field cool

Preface

This thesis is the result of experimental research performed at the Instituut voor Kern-en Stralingfysika of KULeuven and is the culminating point of the author's Integrated Masters on Engineering Physics, taught at the Faculty of Sciences of the University of Porto. It was developed under the supervision of Dr. Lino Pereira (lino.pereira@fys.kuleuven.be), Prof. Dr. João Pedro Araújo (jearaujo@fc.up.pt), and Prof. Dr. Kristiaan Temst (kristiaan.temst@fys.kuleuven.be), integrated in the joint research efforts of IFIMUP–IN in Porto, Portugal and IKS in Leuven, Belgium.

In the first three chapters the field of diluted magnetic semiconductors is introduced, along with an outline of the research performed in the framework of this MSc. Chapter 4 presents the results obtained for this research and their subsequent analysis. At the end of the thesis, a general conclusion summarizes the results and discusses their implications on the future of the field.

Introduction

> *"In a marriage of quantum physics, information theory, and nanoscale engineering, quantum information science endeavors to build machines that can use the power of quantum mechanics for practical purposes."*
>
> – David D. Awschalom, 2013 [1]

Since the dawn of the humanity, information has been one of the main drives of evolution. Sharing information has led to the creation of numerous languages over time, ever in the way of improving *communication* between ourselves. For millenia communication between us was of a short-range, requiring a message carrier in order to communicate over long distances, eventually taking days or weeks to deliver a message. In the last century(ies) we have reached a stage where communication has surpassed these physical boundaries, nowadays enabling the sharing of incredibly vast amounts of information, accessible by a simple touch. Digital communication has become a pillar of modern society.

Digital communication only became possible due to the technological advances on *electronics*. The unceasingly increasing amount of transistors in the last 50 years, packed by billions in very small integrated circuits or chips, led to the outstanding speed and performance of every modern electronic device. Processing speed and integration density of silicon chips has been increasing exponentially, doubling every eighteen months according to *Moore's law*. However, physical limits are being reached as currently used materials are reaching their functional limits. In other words, the use of electron *charge* and its transport in conventional electronics, the very same principles as in the first transistor created fifty years ago, is reaching a *cul-de-sac*.

A possible solution comes in upgrading electronics by introducing an additional degree of freedom, such as the electron *spin*. By using two fundamental properties of the electron or simply by using spin alone, *spintronics* promises a new generation of devices with various advantages over conventional electronics: non-volatile and faster operating devices, increased integration densities and reduced power consumption along with new ways of

processing information [2]. Some examples of spintronic devices are spin-polarized LEDs, spin-field effect transistors (FETs), and spin-based qubits for quantum computing [1].

Spintronics first emerged in 1988, upon the discovery of the giant magnetoresistance (GMR) effect in spin-valve structures by Albert Fert and Peter Grünberg, which earned them the Nobel Prize in Physics in 2007. GMR-based spin-valves quickly made their way into our daily lives in the form of read heads of hard-disks (HDD), revolutionizing data storage technology. These GMR-based spin-valves were quickly replaced in the read-heads of HDDs by magnetic tunnel junctions (MTJ), which are based on the tunnel magnetoresistance effect. These systems are operated in a very close proximity to the spin-valves, with a main difference of using a thin insulator spacer instead of a metallic one.

In spite of revolutionizing data storage technology, this first generation of spintronics (magnetoelectronics) has created a bottleneck in the way current devices manage information: data is stored in *metal-based* magnetic devices, while data processing takes place in *semiconductor-based* electronic devices. The data exchange between these two units costs time and energy, which could be saved if data storage and processing would be integrated in the same device. However, semiconductors currently used in integrated circuits, transistors and lasers, consist mainly of silicon (Si), gallium arsenide (GaAs) and gallium nitride (GaN) – which are non-magnetic materials – while, on the other hand, digital storage devices resort to ferromagnetic materials such as iron (Fe), cobalt (Co) and nickel (Ni) – non-semiconducting materials. Furthermore, combining the two types of materials into a functional heterostructure has been proven to be difficult due to the different crystal structures of magnetic materials and semiconductor materials [3]. The alternative is then to use materials which combine ferromagnetic and semiconducting behavior [4], i.e. evolving from *metal-based* to *semiconductor-based* spintronics.

Dilute magnetic semiconductors emerge as a pioneering development in semiconductor-based spintronics: in a similar fashion to electrical doping in insulating or nearly insulating materials to make them conducting, incorporating magnetic ions into non-magnetic semiconductors so that they become ferromagnetic. With already 30 years of an exciting history, generation after generation of ever increasing Curie temperature, dilute magnetic semiconductors have captured the attention of the semiconductor and magnetism communities. Promising and yet puzzling developments, with hundreds of publications every year, led the field to be considered as one of the most controversial research topics in material science and condensed-matter physics today.

1 Literature Review

This chapter introduces the field of dilute magnetic semiconductors (dms) and more specifically the properties of narrow-gap DMS (Ga,Mn)As. A short motivation and definition of the field is presented in section 1.1.1, followed by an overview of the history of DMS research motivating the work presented in this thesis (section 1.1.2). In the last section 1.2 we describe the current understanding on structure and magnetism of (Ga,Mn)As.

1.1 Dilute Magnetic Semiconductors

1.1.1 Definition

Magnetic semiconductors are materials in which ferromagnetism coexists with semiconducting behavior and have been studied since the 1960s. The first generation is considered by most the true *ferromagnetic semiconductors* consisting of materials containing magnetic elements in their chemical formula, in which the ferromagnetic order is established in the magnetic (periodic) sublattice. These materials were extensively studied from late 1960s to early 1970s, manifesting various interesting properties, such as red-shift of the bandgap upon the onset of ferromagnetic order, but their crystal structures are incompatible with conventional electronics. Additionally, the synthesis of these materials is rather unwieldy and difficult to reproduce. The low Curie temperatures ($T_C < 100$ K) make them of little use in practical applications, which require a ferromagnetic behavior persistent up to typical device operation temperatures (room temperature and above).

Dilute magnetic semiconductors (dms) are magnetic semiconductors in which ferromagnetism is introduced by incorporating magnetic atoms into nonmagnetic semiconductors, in similarity with electrical doping, which makes insulating materials conducting by incorporating donor and acceptor impurities. In these materials, magnetic impurities are distributed randomly, substituting a few percent of the atoms in the host matrix of the nonmagnetic semiconductor. Accordingly, a *magnetic impurity* is an atom or ion of an element which is different from the host's constituents and carries a non-vanishing magnetic moment. The

magnetic moments may originate, e.g. in unfilled 3*d* or 4*f* shells of transition metals and rare earths, respectively.

Dilute magnetic semiconductors can be divided into two classes: *intrinsic* and *non-intrinsic*. These are dependent on two conditions that define the usefulness of the DMS material: (i) the localized magnetic moments must order ferromagnetically and this ordering must be attained up to typical operation temperatures (room temperature and above); (ii) the ferromagnetic state is associated with spintronic functionality, e.g. spin-polarized carriers and electric field control of magnetization. However, efficient spin-polarization of the carriers requires that these must be involved in the order mechanism (carrier-mediated ferromagnetism), automatically excluding materials in which the ferromagnetic order and the semiconductor bands are independent of each other, as is the case of materials composed of small ferromagnetic precipitates embedded in the semiconductor matrix.

Therefore, *intrinsic* DMS materials exhibits a random incorporation of magnetic impurities while in *non-intrinsic* DMS materials these impurities segregate into impurity-rich regions or even in secondary phases.

1.1.2 History of dilute magnetic semiconductors

The first generation of diluted magnetic semiconductors emerged in the early 1980s and consisted of Mn-doped II-VI alloys of the form $A_{1-x}M_xB$, such as $Cd_{1-x}Mn_xTe$ and $Hg_{1-x}Mn_xTe$ (cf. white region in figure 1.1 on the facing page). These materials were very attractive for their easily tunable lattice and band parameters, suitable for heterostructure devices, as well as their very efficient Mn-related electroluminescence, appealing for optoelectronic applications [5]. Despite these alluring properties these materials were dominated by antiferromagnetic superexchange, leading to antiferromagnetic or spin-glass ordering.

A decade later, in the early 1990s (highlighted light gray in figure 1.1 on the next page), the development of nonequilibrium epitaxial growth using low-temperature molecular beam epitaxy (lt-mbe) allowed to overcome the low solubility of transition metal impurities in III–V semiconductors, leading to the first boom in the area of Diluted Magnetic Semiconductors. This second generation of DMS materials consisted mainly of *narrow-gap* III-V semiconductors, such as InAs and GaAs which are well established materials widely used in the electronics and optoelectronics industries with a wide range of applications. In 1992, Ohno *et al.* discovered ferromagnetism up to $35\ \mathrm{K}$ in Mn-doped InAs ($In_{1-x}Mn_xAs$) grown by LT-MBE [6] eventually leading to the development of Mn-doped GaAs ($Ga_{1-x}Mn_xAs$), with even higher Curie temperatures [7]. The Mn impurities introduced in these semiconductors

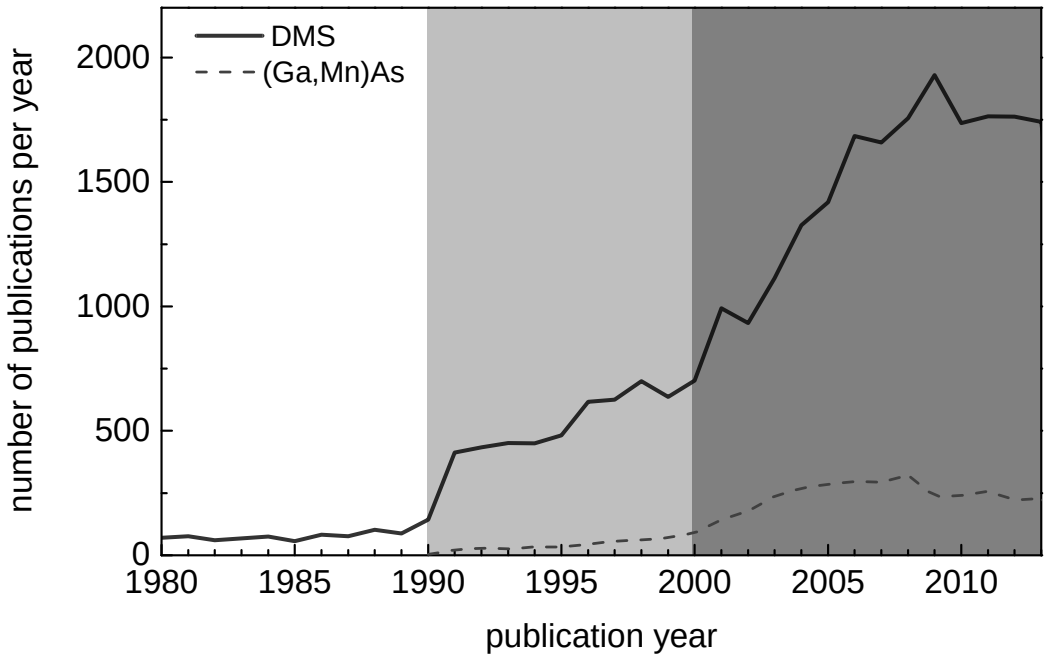

Figure 1.1: Number of publications per year, obtained from "Web of Science" using the keywords "magnetic" and "semiconductor" in the search field *Topic* (black curve) and using "(Ga,Mn)As" and "dms" (dark-gray curve). The white region corresponds to a period where the first generation of diluted magnetic semiconductors emerged. The gray regions indicate the two following generations of DMS materials, with the rise of narrow-gap and wide-gap DMS materials, respectively.

act as acceptors, substituting for the group III elements. With high Mn concentrations (up to $x \sim 0.10$), a high concentration of free holes is present, mediating the ferromagnetic interaction between the localized Mn moments. This carrier-mediated ferromagnetism in $In_{1-x}Mn_xAs$ and $Ga_{1-x}Mn_xAs$ opened the door to new studies on spin-based phenomena in semiconductor devices, such as spin-polarized light emission [8] and electrical and optical control of the magnetization [9, 10]. Furthermore, $Ga_{1-x}Mn_xAs$ is considered one of the best candidates for technological implementation of DMS materials due to the strong technological background on GaAs, its higher Curie temperature (around $200\ \mathrm{K}$) [11, 12, 13, 14] compared to $In_{1-x}Mn_xAs$ ($90\ \mathrm{K}$) [15], and due to its diverse interesting functionalities deriving from its carrier-mediated ferromagnetism and demonstrated in various proof-of-concept devices [16]. Despite major development over the last (almost) 20 years, further increase in Curie temperature faces difficult technical challenges [11, 17].

In the turning of the century, a new type of DMS materials turns up leading to the boom highlighted in dark gray in figure 1.1. While narrow-gap materials such as Mn-doped GaAs and InAs continued to be intensively studied, a third generation of DMS materials emerged in the last decade with the prediction of high-temperature ferromagnetism in wide-

gap oxides and nitrides, such as ZnO and GaN, doped with 3*d* transition metals. The main difference between this new generation and the previous is the bandgap of the host semiconductor: InAs and GaAs are *narrow-gap* semiconductors while ZnO and GaN are *wide-gap* semiconductors. Based on the p-d Zener model, Dietl *et al.* predicted that highly p-type Mn-doped ZnO and GaN could attain a T_C above room temperature [18]. Soon after, the first reports on high temperature ferromagnetism emerged, the first being Co-doped TiO_2 by Matsumoto *et al.* [19] and calculations of stable high-temperature ferromagnetism in ZnO by Sato *et al* [20]. These materials were already intensively studied for their exquisite properties as semiconductors and led to a wide array of applications in electronics (e.g. transparent electrodes and thin film transistors), piezoeletronics (e.g. self-powered nanofibers) and optoelectronics (e.g. LEDs, field emitters). The prediction that these same materials would be suited to display high-temperature ferromagnetism was a surprise and extended their range of applicability to spintronics, therefore propelling the research on wide-gap DMS. Extensive investigations were performed by various groups in order to find the conditions under which room-temperature ferromagnetism emerged leading to a rapidly growing number of reports of wide-gap DMS materials at and above room temperature (cf. reviews [21, 22, 23]), in particular, materials like Co- and Mn-doped ZnO and Mn- and Fe-doped GaN which exhibited ferromagnetism even in the absence of additional doping and are highly compatible with existing semiconductor heterostructure technology [24]. However none of these findings have been confirmed and reproduced by other groups and none has resulted in the demonstration of a device structure working at room temperature. Issues of irreproducibility and instability became evident, with the origin of the ferromagnetism highly debated, resulting in the identification of a number of non-intrinsic sources for the observable room-temperature ferromagnetism: contamination [25, 26], measurement artifacts [25, 26], and formation of ferromagnetic precipitates [27, 28]. Moreover, various comprehensive studies on carefully characterized materials with respect to phase purity found only paramagnetism [29, 30], antiferromagnetic interactions [31, 32, 33, 34], or at best ferromagnetic order with very low T_C (e.g. $T_C < 10\ \mathrm{K}$ in Mn-doped GaN [35]).

On the present day, the DMS field can be divided between narrow- and wide-gap materials. While *narrow-gap* DMS materials, such as Mn-doped InAs and GaAs, are widely accepted to exhibit intrinsic carrier-mediated ferromagnetism, their Curie temperature remains well below room temperature. *Wide-gap* DMS materials appear to exhibit ferromagnetic behavior at and above room temperature, but its origin and usefulness are highly contested. Understanding and devising ways to improve the T_C on narrow-gap DMS materials, while understanding the origin and conditions under which high-temperature ferromagnetism in wide-gap DMS materials constitute major challenges in the DMS field.

A series of accomplishments in this field accounts, to a large extent, for spreading of spintronic research over virtually all materials families, such as derivatives of FeAs-based superconductors, e.g. (K,Ba)(Zn,Mn,Fe)$_2$As$_2$ [36], high Néel temperature semiconductors, e.g. LiMnAs [37] and topological insulators, in which ferromagnetism might be mediated by Dirac electrons, e.g. (Bi,Mn)$_2$Te$_3$ [38].

> *" However, independently of the progress in achieving a high-T_C system, (Ga,Mn)As and related compounds (...) will continue to constitute an important playground for exploring novel phenomena, functionalities, and concepts at the intersection of semiconductor physics and magnetism."*
>
> – Tomasz Dietl, Hideo Ohno, 2014 [39]

1.2 Structure and magnetism of Mn-doped GaAs

The ternary III–V semiconductor (Ga,Mn)As, combining semiconducting properties with magnetism, has become a representative diluted magnetic semiconductor giving rise to a possible integration of electronic and magnetoelectronic devices prospective for future spintronic applications [39, 40, 41]. As one the most widely studied DMS, (Ga,Mn)As is the perfect example of how the magnetic behavior of DMS materials is strongly influenced by local structure.

In typical high Curie temperature (Ga,Mn)As thin films (several % Mn regime) the majority of the Mn impurity atoms substitute for Ga atoms (Mn$_s$), while a minority fraction occupies interstitial sites (Mn$_i$) [17, 42]. Substitutional Mn impurities provide both the localized magnetic moment and the itinerant holes that mediate the magnetic coupling, whereas interstitial Mn impurities have a twofold compensating effect: (i) magnetic, as there is an antiferromagnetic coupling between Mn$_i$ and Mn$_s$ pairs through a superexchange interaction, and (ii) electric, since double donor Mn$_i$ compensates Mn$_s$ acceptors [17, 43, 44, 45]. Another compensating impurity that may be present in high-T_C (Ga,Mn)As thin films is the Arsenic antisite (As$_{Ga}$) [46, 47], where As atoms occupy Ga substitutional sites. This defect is formed during growth by low-temperature molecular beam epitaxy (LT-MBE). The As$_{Ga}$ antisites are stable up to $\sim 450^oC$ [48], which is well above the transition temperature from a uniform diluted magnetic semiconductor to a multiphase structure with metallic MnAs and other precipitates. Therefore, the number of As$_{Ga}$ defects has to be minimized during MBE growth, by precisely controlling the stoichiometry of deposited epilayers [47]. On the other hand, the Mn$_i$ impurity concentration can be significant in as-grown structures, with an

increasing fractions for higher Mn concentrations [17, 44]. It has however, a higher mobility than the antisites and can be removed by low temperature annealing [44, 49].

As we will see through out this thesis, the magneto-electronic behavior of (Ga,Mn) As is defined mainly by the concentration of Mn impurities: the self compensation by Mn_i for a given Mn_s concentration determines the hole concentration, the Fermi level and the effective Mn_s concentration (of non-compensated Mn_s moments). The existence of such a crucial role of Mn_i is clearly reflected in the effect of Mn_i concentration on the two figures of merit: Curie temperature (T_C) and magnetization [14, 17, 42]. However, the exact dependency is still subject of debate [14, 39, 41, 42], which is directly linked to the debate on the basic mechanisms of magnetic interaction in Mn-doped III-V DMS (valence-band p-d exchange versus impurity-band d-d superexchange) [39, 41, 42, 50]. Ultimately, the balance between Mn_i and Mn_s concentrations may in fact determine which of the two mechanisms dominates in a given (Ga,Mn)As film.

1.2.1 Ferromagnetic interactions in Mn-doped GaAs

Two fundamentally opposing theoretical points of view have developed over the years of researching (Ga,Mn)As: the mean-field Zener model and the impurity band model.

The Zener model was first proposed in 1951 by Clarence Zener [51] as a model for the role of band carriers in promoting ferromagnetic ordering between localized spins in magnetic metals. By the *sp-d* exchange coupling to the localized spins, the spin subbands split forcing a redistribution of the carriers and thus lowering their energy allowing for ferromagnetic ordering to emerge. In accordance to the Ruderman-Kittel-Kasuya-Yosida (RKKY) quantum mechanical treatment, the sign of the resulting interaction between localized spins oscillates with the spin-spin distance, indicating that the RKKY and Zener models are equivalent within the continuous and mean-field approximation [52]. These approximations are valid as long as the period of RKKY oscillations $R = \pi/k_{\mathrm{F}}$ is large compared to an average distance between localized spins. Hence, for DMS systems the mean-field Zener model reveals itself as a simpler approach, as for these materials the distance between the carriers is of the same magnitude as the distance between spins, i.e. $p \lesssim xN_0$, where p is the carrier density, x the impurity concentration and N_0 the number of impurity atoms. Microscopic models of the electronic structure of metallic (Ga,Mn)As assert a localized character of the five Mn_s *d* orbitals forming a moment $S = 5/2$ and describe hole states in the valence band using the Kohn-Luttinger parameterization for GaAs [53] and a single constant J_{pd} which characterizes the exchange interaction between Mn_s and hole spins.

The exchange interaction follows from hybridization between Mn d orbitals and valence band p orbitals. Accordingly, and in particular in (Ga,Mn)As, holes are considerably more efficient in mediating spin-dependent interactions between localized spins, due to a higher density of states (DOS) and to larger exchange coupling to Mn spins. In other words, by coupling with a localized Mn $3d^5$ moment, a $2p$ valence band hole will become spin-polarized, and since holes are weakly localized in the (Ga,Mn)As lattice they'll interact with other Mn moments, leading to ferromagnetic ordering [18]. This approach was shown to successfully describe a number of properties observed in ferromagnetic dms, in particular in (Ga,Mn)As. These properties are the ferromagnetic transition temperature T_C, predicted to increase monotonically with effective Mn concentration x_{eff} and with carrier density with no fundamental limit to T_C below room temperature, magnetization, spin polarization of the hole liquid and magneto-crystalline anisotropy with its strain and temperature dependence, amongst others (cf. reviews [16, 39, 41]).

In particular, the effect of strain on magnetic anisotropy in (Ga,Mn)As can be tuned by using different substrates and buffer layers in (Ga,Mn)As films leading to an in-plane or out-of-plane magnetic anisotropy [54]. In some cases, uniaxial anisotropy is also present in-plane between the $[100]$ and the $[110]$ directions and even between crystallographically equivalent axes ($[110]$ and $[\bar{1}10]$) [55, 56].

The impurity band model states that the magnetism is mediated by localized impurity-derived states [49]. In this picture, and within the relevant hole concentration range, the impurity band and valence bands are not merged, and the Fermi level is located within the impurity band (IB) and, therefore, T_C will depend on the localization of these states: states in the center of the IB are extended and maximize T_C, while states towards the top or bottom of the IB are more localized, reducing T_C. In other words, the $3d$ holes that lie in the IB hop between the localized Mn impurities, mediating the ferromagnetic ordering between the latter. In this model, the Curie temperature is independent of the effective Mn concentration while, ironically, the presence of interstitial Mn impurities is essential for the localization of the Fermi level inside the impurity band.

In fact, Dobrowolska *et al* [42], by combining ion channeling measurements with magnetization, transport and magneto-optical data, observed a non-monotonic variation of T_C up to a rather high nominal concentration of Mn in (Ga,Mn)As, consistent with the IB model. However, this effect was only studied in the insulator side of the metal-to-insulator transition (MIT) and was soon contested by other groups. In a more recent review, Wang *et al* [14], armed with nearly the same analysis techniques, disputed the results of the latter report, by demonstrating that the carrier density in annealed (Ga,Mn)As films can be compared

to the substitutional Mn acceptor concentration, i.e. in weakly compensated systems, with weakly confined holes, T_C and electrical conductivity do not tend to zero. This report is not consistent with the picture of a Fermi level located in an isolated impurity band, but with the previously well established *p-d* Zener model.

1.2.2 Compensation by interstitial Mn

Despite this central role in understanding the magnetism in (Ga,Mn)As, and consequently of Mn-doped III-V DMS materials, interstitial Mn is far from being a well understood defect. As seen in the previous section, T_C increases with effective Mn concentration, which takes into account the balance between the fractions of Mn substituting for Ga (Mn_s) and on the interstitial sites (Mn_i). Mn_s is responsible for the localized magnetic moments and the itinerant holes that mediate the ferromagnetic coupling, whereas Mn_i has a two-fold compensation effect: magnetic, as Mn_i couples antiferromagnetically with Mn_s, and electrical, since double donor Mn_i compensates Mn_s acceptors. As a result, the effective concentration x_{eff} of Mn impurities that effectively contributes to the observable ferromagnetism in (Ga,Mn)As, is smaller than the nominal concentration x by twice the Mn_i concentration x_i, $x_{\text{eff}} = x - 2x_i$. Accordingly, the hole concentration *p* should be smaller or of the order of this effective concentration, $p \lesssim x - 2x_i$.

Despite the Mn concentration that can be incorporated in high-quality (Ga,Mn)As has been increased throughout the years up to 20%, T_C saturates at ~ 200 K for concentrations $x = 10\%$ [57]. The highest T_C and p values achieved in (Ga,Mn)As are obtained after annealing close to growth temperature, around $\sim 200°$C [11, 58]. Transport measurements have shown a partial activation by annealing that results from the out-diffusion of a compensating defect with a low thermal stability, with an activation energy of $E_a = 0.7$ eV [44]. This report was supported by *ab initio* calculations yielding similar activation energy for Mn_i [17, 44]. In fact, by annealing around this temperature the Mn_i diffuses to the surface where it is passivated, partaking in the formation of a antiferromagnetic MnO thin film [13, 44, 59] or an MnAs monolayer, if the surface is capped with an As layer [60]. However, a significant fraction of the introduced Mn still remains inactive, as $x_{\text{eff}} < x$ and $p < x$ after annealing. It became generally accepted that Mn_i was the low temperature diffuser, establishing the belief that pure substitutional Mn doping can be achieved by low temperature ($\sim 200°$C) thermal annealing. Since then, research focused on increasing the concentration of magnetically active Mn in order to achieve T_C above room temperature, however facing technical challenges in achieving concentrations beyond $x \approx 0.10$ with maximum $T_C = 185$ K [11, 14, 17].

Overcoming this solubility limit with alternate growth and/or post-processing methods would unlock the possibility of increasing T_C above the current maximum, allowing for the realization of possible room temperature ferromagnetism in $Ga_{1-x}Mn_xAs$.

1.2.2.1 Lattice Location

There are several interstitial sites in the zincblende structure of GaAs – tetrahedral(T), bond centered (BC), anti-bonding (AB) among others (cf. figure 1.2 on the following page). Experimental techniques commonly used to identify lattice sites of impurities in crystalline solids are either based on channeling of charged particles (ions or electrons) or on probing the atomic environment of the impurity atom, e.g. in X-ray absorption fine structure (XAFS) techniques.

The first reports on Mn impurities lattice location are on pure Ga-substitutional incorporation (by XAFS [61]) and mixed Ga-substitutional and T interstitial occupancy (by ion channeling [62] and XAFS [63]), with the majority of the atoms in substitutional sites. Although consistent with Mn_i occupying tetrahedral (T) interstitial sites, the measurements did not allow to discriminate between the two nonequivalent T sites in zincblende GaAS: coordinated by four Ga atoms (T_{Ga}) or by four As atoms (T_{As}) [64, 65]. More recently, xafs experiments confirmed the mixed occupancy and identified the T_{Ga} interstitial site [66, 67]. On the theoretical side, *ab initio* calculations yielded lower energy for Mn in T_{As} sites compared to T_{Ga} [44], which is consistent with the expectation of having the Mn cations coordinated by As anions. However, XAFS is not well suited to distinguish elements with similar atomic numbers, as is the case for Ga and As, especially in cases of multi-site occupancy (substitutional and interstitial) where the site to be identified is in fact the minority one (interstitial). Transmission electron microscopy measurements using (002) diffracted beam indicated that the Mn_i predominantly occupy the T_{As} site [46]. Pioneering work using X-ray scattering techniques to probe dopant lattice location reported comparable T_{Ga} and T_{As} occupancies [68, 69, 70]. Coexisting T_{Ga} and T_{As} occupancies would suggest that the Mn_i lattice site depends on the presence of neighboring Mn_s atoms, i.e. that isolated Mn_i and Mn_i in Mn_i-Mn_s pairs occupy different T sites. This is however in contradiction with density functional theory (DFT) calculations which predicted that, for typical ferromagnetic (Ga,Mn)As samples (where the Mn_s concentration is the large majority over that of Mn_i), T_{As} is the most stable site for Mn_i regardless of being isolated, in Mn_i-Mn_s pairs, or even in Mn_s-Mn_i-Mn_s triplets [71].

Solving this inconsistency would allow for a better understanding of the mechanisms of

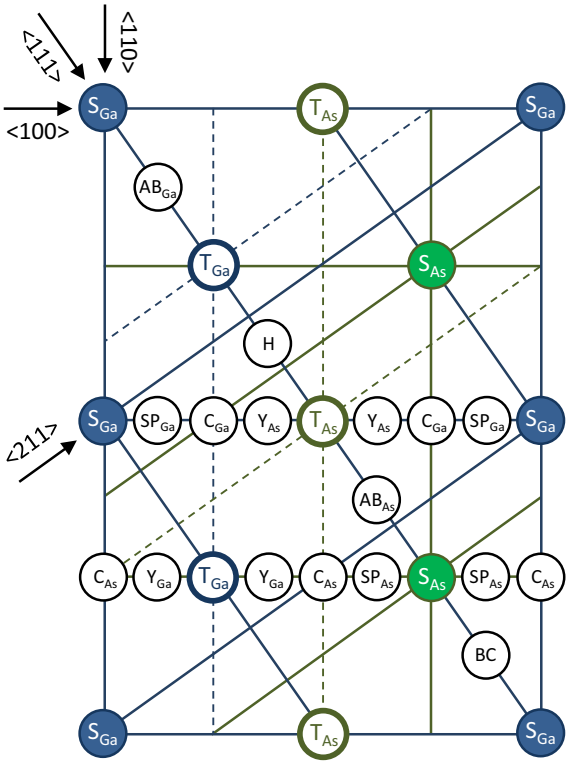

Figure 1.2: The $\{110\}$ plane in GaAs zincblende lattice, showing the following sites: the substitutional Ga (S_{Ga}) and As (S_{As}) sites; the tetrahedral interstitial sites with Ga (T_{Ga}) and As (T_{As}) nearest neighbors; interstitial sites along the $<111>$ direction, i.e. the bond center (BC), antibonding Ga (AB_{Ga}), antibonding As (AB_{As}), and the hexagonal site (H); and the interstitial sites along the $<100>$ direction, in either Ga or As rows, i.e. the split interstitials (SP_{Ga} and SP_{As}), the "C" sites with C_{2v} symmetry (C_{Ga} and C_{As}), and the "Y" sites (Y_{Ga} and Y_{As}). Along the $<100>$, $<111>$, $<110>$ and $<211>$ directions, the rows of Ga and As atoms are indicated (lines), as the rows of the T_{Ga} and T_{As} sites (dashed lines). Note that, along the $<111>$ direction, the substitutional (S_{Ga} and S_{As}) and tetrahedral interstitial (T_{Ga} and T_{AS}) sites are all located on the same row; along the $<100>$ direction, S_{Ga} is on the same row as T_{As}, and S_{As} is on the same row as T_{Ga}.

electric and magnetic compensation by Mn_i which, as introduced above, plays a central role in the behavior of (Ga,Mn)As. Establishing the lattice location of Mn in (Ga,Mn)As requires the use of a technique which can unambiguously distinguish the two T sites. In fact, the Emission Channeling technique is uniquely suited to address this problem (cf. section 3.2 on page 16), and was used in a recent study on GaAs in the very low concentration regime ($x < 0.05$ at. %) with different doping (undoped, p-type and n-type) [65, 64] to identify the lattice location and thermal stability of Mn impurities. In these reports, the Mn impurities were found to occupy mainly the substitutional site with a fraction on the T_{As} interstitial site. This interstitial diffuses around $400°$C, by converting into substitutional Mn, a much higher temperature than reported in literature [44, 17]. However, these experiments were

performed on GaAs within the very low Mn doping regime ($x < 0.05$ at. %), which has a different local structure than (Ga,Mn)As, i.e. the presence of a higher concentration of Mn impurities might have a strong influence in the diffusion and stability of interstitial Mn.

1.2.3 Mn aggregation and secondary phases formation

As mentioned above, annealing Mn-doped GaAs at $\sim 200\ ^{\circ}\mathrm{C}$ typically increases T_C. However, comparing T_C after thermal annealing at temperatures between 160°C and 220°C, it was found that T_C actually decreases with increasing annealing temperature [11]. Further increasing the annealing temperature ($> 280^{\circ}$C) eventually leads to an actual decrease of T_C. This is indicative of a second occurring process, with an activation energy slightly above that of the out-diffusion of the compensating defect. This second process has been suggested to be related to Mn aggregation (or segregation). It is however unclear what type of aggregation it is, i.e. whether it is only chemical or also structural. Ion-channeling experiments have shown that part of the substitutional Mn converts to a random fraction at 282°C, most likely due to cluster formation [62]. This indicates that phase segregation starts already at relatively low temperatures. *Ab initio* studies on the substitutional Mn diffusion have shown that Ga vacancies act as an efficient trap for Mn_s to diffuse and that the clustering rate increases along temperature and/or Mn concentration, effectively decreasing T_C [72]. Furthermore, at large Mn concentrations clustering takes place already during sample growth.

On the other hand, by annealing at relatively high temperatures ($> 500^{\circ}$C) the precipitation of Mn impurities onto a MnAs secondary phase becomes evident [73]. Based on high-resolution X-ray diffraction (HRXRD) and grazing-incidence diffraction (GIXRD) it was reported the co-existence of two different types of MnAs secondary phases [74] in samples annealed at $700\ ^{\circ}\mathrm{C}$ (Ga,Mn)As: small, coherent with GaAs matrix, zincblende (ZB) MnAs nanoclusters – chemical segregation – and bigger, lattice-distorting, NiAs–type (hexagonal) MnAs nanoclusters – consistent with chemical and structural segregation. In the following years, these two types of clusters have been extensively characterized [75, 76, 77, 78]. Transmission electron microscopy (TEM) experiments [77] and X-ray absorption spectroscopy (XAS) [79] have shown that upon thermal annealing at $500\ ^{\circ}\mathrm{C}$, only Mn-rich zincblende (Mn,Ga)As clusters (~ 3 nm) are formed which are coherent with the GaAs matrix. These coherent (Mn,Ga)As nanoclusters were shown to be ferromagnetic above room temperature, with a $T_C \sim 360$ K, as the local concentration of Mn reaches the expected $x \sim 20\%$, that would allow for (Ga,Mn)As to be ferromagnetic at room temperature as well. Annealing at 600°C has been demonstrated to lead to the precipitation of well defined

hexagonal NiAs–type MnAs nanoclusters [75, 76, 77, 78]. While these nanoclusters are significantly bigger ($20-45$ nm) than the ZB nanoclusters ($3-8$ nm), they are strained in the GaAs structure and also display ferromagnetism, however with a lower Curie temperature ($T_C \sim 300$ K). Using aberration-corrected tem and aberration-corrected annular dark-field (ADF) STEM it was shown that when annealing (Ga,Mn)As thin films at temperatures above $400°$C both ZB and NiAs–type nanoclusters form along with adjacent As nanocrystals and voids [80, 81]. On another study, the presence of nanoclusters in (Ga,Mn)As was shown to increase in two orders of magnitude the coercivity of the material without significantly reducing T_C [82].

All in all, in order to efficiently obtain high-T_C (Ga,Mn)As thin films the growth temperature must be decreased as Mn concentration increases [17, 83], in order to avoid secondary phase formation.

> *"The case of (Ga,Mn)As is an optimistic reminder that the complex defect physics of these systems is an opportunity not a warning. The magnetic properties of any diluted magnetic semiconductor ferromagnet can be improved by understanding and learning to control defects."*
>
> – A. MacDonald, P. Schiffer and N. Samarth, 2005 [84]

2 Objectives and outline

This work addresses the current goals and challenges facing the narrow-gap DMS field, and in particular the research on (Ga,Mn)As ferromagnetic thin films, which were described in section 1.2. The objectives of this work and corresponding research approach are summarized as follows.

(A) To determine the lattice location of interstitial Mn in (Ga,Mn)As. The goal is to identify unambiguously the interstitial Mn site in ferromagnetic (Ga,Mn)As, using the emission channeling technique (described in section 3.2). The results and implications on the understanding of the fundamental devices behind the compensation by interstitial Mn in (Ga,Mn)As films are described in section 4.1 on page 27.

(B) To study the thermal stability and diffusion of Mn impurities in (Ga,Mn)As. The objective is to investigate the thermal stability of Mn impurities in (Ga,Mn)As doped with different Mn impurity concentrations (1% and 5%), and describe its diffusion behavior upon thermal annealing at various temperatures. Results are presented in section 4.2 on page 41.

(C) To investigate the structure and magnetism of annealed (Ga,Mn)As. The aim of is to ascertain the different structural and magnetic properties of (Ga,Mn)As within the ferromagnetic regime (as-grown and annealed at $200\ ^{\circ}\mathrm{C}$) and within the secondary phase regime (annealed at $300\ ^{\circ}\mathrm{C}$ and at $600\ ^{\circ}\mathrm{C}$). Results are presented and discussed in section 4.3 on page 55.

3 Experimental techniques

This chapter describes the experimental techniques used in this work. The (Ga,Mn)As samples were grown by low-temperature molecular beam epitaxy (LT-MBE) by the Nottingham group (U.K.) [83]. Sample characterization was carried out using synchrotron radiation X-ray Diffraction (SR-XRD) in order to determine the structure and secondary phase formation (cf. section 3.1), Extended X-Ray Absorption Fine Structure (EXAFS) to probe the local structure of Mn impurities, Electron Emission Channeling (EC) to study the lattice location of Mn impurities (cf. section 3.2 on the following page) and Superconducting Quantum Interference Device (SQUID) magnetometry to investigate the magnetic properties (cf. section 3.3 on page 25).

Albeit in this chapter we present a description of the experimental setups, only for the Emission Channeling technique a detailed description is given, as it is an unique and unconventional technique. The experimental procedure and data analysis of the EXAFS experiment is not given, since the experiments and subsequent analysis were not performed by the author. The remaining techniques were applied following standard systems and protocols and, therefore, only a small description is provided.

3.1 Synchrotron Radiation X-Ray Diffraction

The interaction of X-rays with the crystal lattice of a material allows us to extract information on the lattice. Such is the purpose of X-ray diffraction (XRD) techniques. The most commonly used technique is the θ-2θ scan in Bragg-Brentano geometry, where a sample is tilted towards an X-ray beam over an angle θ and a detector is rotated over the angle 2θ so that the Bragg diffraction criterion is fulfilled for planes that are parallel to the sample stage, provided they have the correct d-spacing determined by the wavelength of the X-rays and the 2θ angle of the detector through the Bragg rule $2d \sin\theta = n\lambda$. However, it is important to be aware of the limitations of this standard technique, as the used geometry will result in a signal which *only* depends on the crystal planes *parallel* to the sample stage surface, and thus any information on the occurrence or orientation of other planes is lost. In other

words, in an epitaxial thin film the diffraction peaks of the substrate and of the film will be much more intense than the peaks from a secondary phase with a random orientation. For the study of materials which can be provided as a powder, this raises no problems, as the statistical distribution of the plane orientations will be uniform (resulting in random orientation of the crystal planes), but for epitaxially grown samples with a secondary phase a lot of information will be missed.

In θ-2θ geometry the intensity of a diffraction peak is significantly influenced by the amount of material contributing to the diffraction. In order to probe the orientation of an eventual secondary phase on a single crystal thin film, the use of another diffraction geometry is required. In this work we resorted to the grazing incidence X-ray diffraction (GIXRD) geometry, where the sample is irradiated by X-rays at a small angle, so that these probe only the thin film, effectively increasing the contribution of the thin film to the signal. An advantage of GIXRD is that the electric field at the critical angle is amplified making the signal stronger. In other words, for a single-crystal in GIXRD geometry the Bragg condition is not fulfilled for the substrates peaks. The measurement results then solely on the contribution of diffraction from polycrystalline secondary phases.

The XRD measurements presented in this work were performed on the BM20B-Rosendorf beamline [85] at the European Synchrotron Radiation Facility (ESRF) in Grenoble, France, using an incident photon energy of 11.5 keV, corresponding to a wavelength of $\lambda = 1.0789$ Å. A symmetrical θ-2θ scan was performed in the range $15°$-$80°$, with a high resolution (HRXRD) scan in the range of the first diffraction of the substrate peak, $20.5°$-$22.5°$. Additionally, asymmetrical GIXRD measurements were performed with an incident angle of $1.5°$. Both measurements were recorded using a linear 1D Mythen detector with 1280 channels, with a measurement resolution of $0.01°$.

3.2 Electron Emission Channeling

The electron emission channeling technique has been developed for the study of the lattice site location of impurities in single-crystals and offers a number of advantages when compared to other techniques. Because it relies on the direct comparison between experimental and calculated (2-dimensional) patterns, it provides unambiguous and quantitative lattice location superior to more conventional implementations of ion-channeling techniques such as Rutherford backscattering spectrometry (RBS), particle-induced X-ray emission (PIXE) and nuclear reaction analysis (NRA). Additionally, not relying on elastic recoil like the widely used conventional RBS, it allows a better identification of impurity atoms lighter than the

major constituents of the material, even in cases of multi-site occupancy, with much higher sensitivity (down to 10^{12} $\mathrm{at.cm^{-2}}$), particularly suited for dilute systems, like the one studied in this work.

3.2.1 Principles

The emission channeling technique makes use of the charged particles emitted by a decaying radioactive isotope. These particles are emitted isotropically during decay and are channeled along the screened Coulomb potential of atomic rows and planes. Along low-index crystal directions of single crystals, this anisotropic scattering results in well-defined channeling or blocking effects. Because these effects strongly depend on the initial position of the emitted particles, they lead to emission patterns which are characteristic of the lattice sites occupied by the probe atoms.

Channeling was first introduced by Lindhard in 1965 [86] and is referred to as the mechanism by which atomic rows and planes steer energetic charged particles along major crystal axis and planes. Because the motion of energetic charged particles in a solid is mainly determined by their Coulomb interaction with the (screened) nuclear charges in the lattice, one can expect that particle propagation is very different among these three types of directions. The general principles described for the channeling of heavy, positive ions apply to the channeling of electrons, which are lighter and negatively charged. Changing the sign of the propagating particle's charge is equivalent to changing the sign of the Coulomb potential: negatively charged particles "see" as channels the rows of nuclear charges instead of the space in between. However, although providing an intuitive insight in the elementary phenomena, the classical approach of Lindhard does not describe quantitatively *electron* emission channeling, in which quantum effects must be taken in account. Details on the theoretical aspects of emission channeling can be found, for example, in [87].

The principle of *emission* channeling is slightly different than conventional channeling techniques that rely on the use of an external *ion beam* and its interaction with the impurity atoms in the host lattice, like RBS, PIXE or NRA, in the sense that the channeled particles are emitted from *within* the crystal by a radioactive isotope of the impurity element under study. The emission channeling technique can be applied using either α or electron (β^- or conversion electrons) emitters. In the latter case, the technique is known as electron emission channeling, for which the requirement of *stability* [1] determines that the *channeling*

[1] The principle of stability requires that the particle does not approach the rows of atoms too closely, otherwise, instead of a gentle steering via the interaction with the row of atoms, the particle experiences wide-angle deflections in head-on collisions with individual atoms

and *blocking* effects depend on the initial position and direction of the emitted particle with respect to the lattice, which in turn depends on the lattice site occupied by the radioactive impurity. Figure 3.1 illustrates how such electron *channeling* and *blocking* enable the distinction between, for example, substitutional versus interstitial impurities.

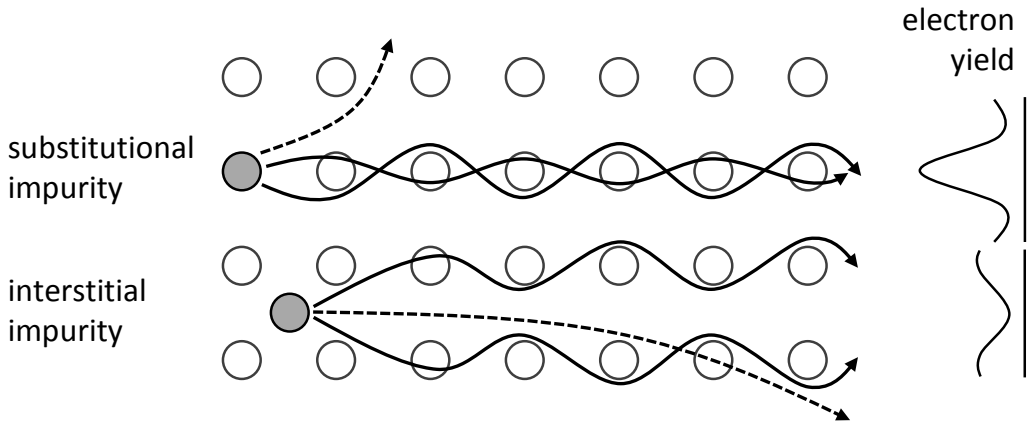

Figure 3.1: Schematic representation of *channeling* and *blocking* effects for substitutional versus interstitial electron emitter impurity. The trajectories of *channeled* (bound state) and *blocked* (free state) electrons are represented by solid lines and dashed lines, respectively. The electron yield profiles as a function of emission angle towards the crystal axis (1-dimensional angular scans) are represented on the right for substitutional versus interstitial emitters.

The electron emission channeling experiments described in this worked were performed at the on-line isotope separator facility ISOLDE at CERN [88] and can be summarized in four steps:

1. The single crystal or epitaxial thin film is implanted with radioactive electron (β^- or conversion electrons) emitting isotopes, occupying certain lattice site(s) [89].

2. A fraction of the emitted electrons are channeled along the crystal axes and planes and leave the sample surface describing anisotropic emission patterns which are characteristic of the emission site and the channeling axis.

3. These anisotropic emission patterns are recorded using a position-sensitive detector around selected crystallographic axes.

4. The lattice site(s) of the impurities is determined by fitting these 2-dimensional experimental patterns with theoretical ones.

In the remainder of this section a short description of the experimental aspects of the

electron emission channeling technique (steps 2 to 4) is presented. More details on the experimental aspects of emission channeling can be found, for example, in [87, 90, 91, 92].

3.2.2 Experimental setup

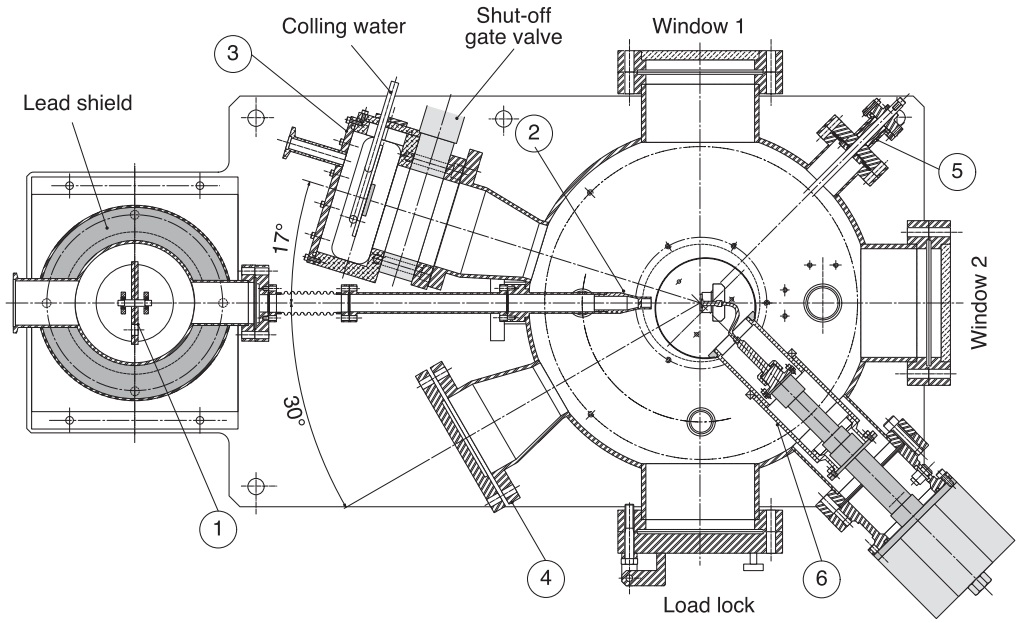

Figure 3.2: Emission Channeling Short Lived Isotopes (EC-SLI) chamber horizontal cross section: 1 – lead shield and rotatable disk with collimator holes; 2 – fixed aperture removable collimator; 3 – fast Si pad ($28 \times 28\ \mathrm{mm}^2$) electron detector block mounted on the DF17 flange; 4 – spare detector flange DF30; 5 – displaceable Faraday cup mechanism; and 6 – cryogenic block, cryogenic shields, and cold finger. Taken from [88].

Emission channeling experiments can be performed either on-line or off-line. In on-line experiments, the emission channeling measurements are performed *in-situ*, i.e. in the same chamber as the radioactive implantations. This is necessary for experiments involving relatively short-lived isotopes, i.e. with half-lives of a few hours and below. In off-line experiments, the sample is transferred to an emission channeling setup after implantation with the (long-lived) probe isotope. The concept of such a setup is rather simple and relies on the ability to detect, as a function of angle, electrons emitted from the sample in the vicinity of a crystallographic axis. The three basic components are a high-vacuum chamber, a goniometer to rotate the sample holder, and a position-sensitive electron detector (figure 3.2).

Inside a vacuum chamber ($< 10^{-5}\ \mathrm{mbar}$), the sample is mounted vertically, facing the

detector, oriented in such a way that electrons emitted from the sample in the vicinity of a selected crystallographic axis reach the position-sensitive detector. The geometry of the chamber is such that it allows for the emission yield to be recorded as a function of angle in the form of 2-dimensional (2D) patterns. A two-axes goniometer allows the sample to be moved along the vertical direction and around two rotation axes (φ and θ) with a typical angular precision of about $0.05°$-$0.1°$. Note that, because 2D position-sensitive detectors are used, the accuracy of the goniometer does not affect the angular resolution of the measurements. The sample holder is equipped with a tungsten wire resistive heating device, which allows for the measurements to be performed at elevated temperatures and/or after *in-situ* vacuum annealing up to 900°C [88]. The principle of operation of the position-sensitive detectors is based on integrating an array of separate detector cells (pads or pixels) on a single Si chip and individually contacting them on the surface by a pattern of conducting and insulating layers. The square-shaped sensitive area is $28.6 \times 28.6\ \mathrm{mm}^2$ and consists of 22×22 pixels (thus each of $1.3 \times 1.3\,\mathrm{mm}^2$). The multiplexed readout of all pads is triggered if the signal on the detector back plane, which is common to all pads, exceeds an externally set lower threshold. This readout procedure limits the count rate of the device to a maximum of about 4000 events/s.

3.2.3 Angular resolution

The experimental angular resolution is a key parameter in the quantitative analysis of emission channeling patterns and is dependent on a series of parameters. For a position-sensitive detection system, it depends on the distance d between sample and detector, the position resolution of the detector, which may vary with energy and nature of the incoming particles, and on the size and shape of the projected beam spot. Assuming that both the position resolution of the detector and the projected beam spot distribution can be approximated as two-dimensional isotropic Gaussian distributions with standard deviations σ_d and σ_b, respectively, the total angular resolution is given by

$$\sigma_{ang} \approx \arctan\left(\frac{\sqrt{\sigma_d^2 + \sigma_b^2}}{d}\right) \approx \frac{\sqrt{\sigma_d^2 + \sigma_b^2}}{d} \tag{3.1}$$

In most experiments, d is set to $\approx 30\ \mathrm{cm}$ in order to cover an angular range of $5°$-$6°$, the relevant range in typical emission channeling patterns. When the channeling effects are very sharp, e.g. for high energy β^- decays, and a higher angular resolution is thus required, d can be set to $\approx 60\ \mathrm{cm}$, which increases the angular resolution by roughly a factor of 2. Since, in either case, the resolution is limited by the size of the pixels ($\sim 1,3\ \mathrm{mm}$), it makes

little difference to use a beam spot which is much smaller. As a trade-off between position resolution and beam transmission, a $1\ \mathrm{mm}$ beam spot is typically used, which requires beam collimation during implantation. Assuming that the standard deviations associated with the beam spot (σ_b) and the pixels (σ_d) are about half of their sizes, the angular resolution σ_{ang} is approximately 0.16° for $d = 30\ \mathrm{cm}$ and 0.08° for $d = 60\ \mathrm{cm}$.

3.2.4 Data analysis procedures

Quantitative lattice location of the radioactive probes is obtained by fitting the theoretical patterns to experimental ones. In the following, we discuss the relevant input parameters for the calculations and describe the fitting procedure.

3.2.4.1 *Manybeam* calculations

Using the *manybeam* program developed by Hofsäss and Lindner [87, 90, 91] and modified by Wahl [92] the theoretical emission patterns can be calculated. This program calculates the angle-dependent emission channeling yields for any emitter lattice position along any crystallographic direction (typically for an angular range of 0° to 3° from the axes in steps of 0.05°).

The starting point for a *manybeam* calculation is the crystallographic structure of the host material. The 3-dimensional structure can be determined experimentally using X-ray diffraction and is well established for the materials used in this work. The *manybeam* formalism uses the 2-dimensional projections with respect to the channeling axes, which can be obtained from the 3-dimensional structures published in the literature. Another important input parameter is the vibration amplitude of the crystal atoms. The one-dimensional root mean square (rms) vibration amplitude u_1 can be determined experimentally from the Debye-Waller factors in X-ray absorption or diffraction experiments. Published values are used as input for the *manybeam* calculations.

The actual displacement amplitudes are obtained from fitting the experimental patterns with theoretical ones calculated for a set of different rms displacement values. Large deviations (tenths of Å) from these reference values can be associated with static displacement of the impurity due to lattice relaxation in its vicinity. Such lattice relaxation may be caused by the impurity itself (a foreign atom that disturbs the crystal periodicity) or by the interaction between the impurities and neighboring native defects (vacancies and interstitials), i.e. impurity-defect complex formation. In principle, such impurity displacements are better

described by a static displacement from the high-symmetry site. However, such relaxation effects may displace the impurities in various directions and by various distances, depending on the specific local structure of each impurity. The measured emission pattern can thus be a superposition of a distribution of sites in the vicinity of a high-symmetry site. In such cases, the occupied site may be relatively well described by the high-symmetry site with an rms displacement larger than the thermal vibration amplitude.

The output of the *manybeam* calculations, for a given material, channeling axis and impurity isotope, is a two-dimensional emission pattern for each impurity lattice site and rms displacement u_1. These patterns are *smoothed* using a Gaussian with $\sigma \simeq 0.1^\circ$ to account for the contribution of the 1 mm beam spot to the experimental angular resolution (see section 3.2.3). Higher values of σ may be used in order to account for, e.g., crystal mosaicity and extended damage due to high fluence implantation. The size and shape of the detector pads is taken into account by averaging over the simulated yield falling within the angular range $(0, 26^\circ \times 0, 26^\circ)$ of one pixel, resulting in the final theoretical emission pattern $\chi^{theo}(\theta, \phi)$. As an example, figure 3.3 on the facing page shows the simulated emission patterns for ^{56}Mn, in different sites of the GaAs zincblende structure, around different crystallographic directions according to the sites described in figure 1.2 on page 10.

3.2.4.2 Fitting procedures

The *FDD* program was developed by Wahl [93] to perform the quantitative analysis of the experimental 2D patterns $\chi^{exp}(\theta, \phi)$ by fitting a linear combination of the calculated yields $\chi^{theo}(\theta, \phi)$. The fitting routines allow up to n occupied sites according to:

$$\chi^{exp}(\theta, \phi) = S \left[f_{rand} + \sum_{i=1}^{n} f_i \chi_i^{theo}(\theta, \phi) \right] \tag{3.2}$$

where S is a scaling factor and f_i denotes the fraction of emitter atoms occupying the i^{th} site. The random fraction f_{rand} accounts for emitter atoms which do not contribute significantly to the anisotropy of the pattern. These can be either located on sites with very low crystal symmetry or in heavily damaged (or even amorphous) surroundings or have a random occupation of several minority lattice sites. Because the sum of all the fractions must amount to 1, f_{rand} is given by

$$f_{rand} = 1 - \sum_{i=1}^{n} f_i. \tag{3.3}$$

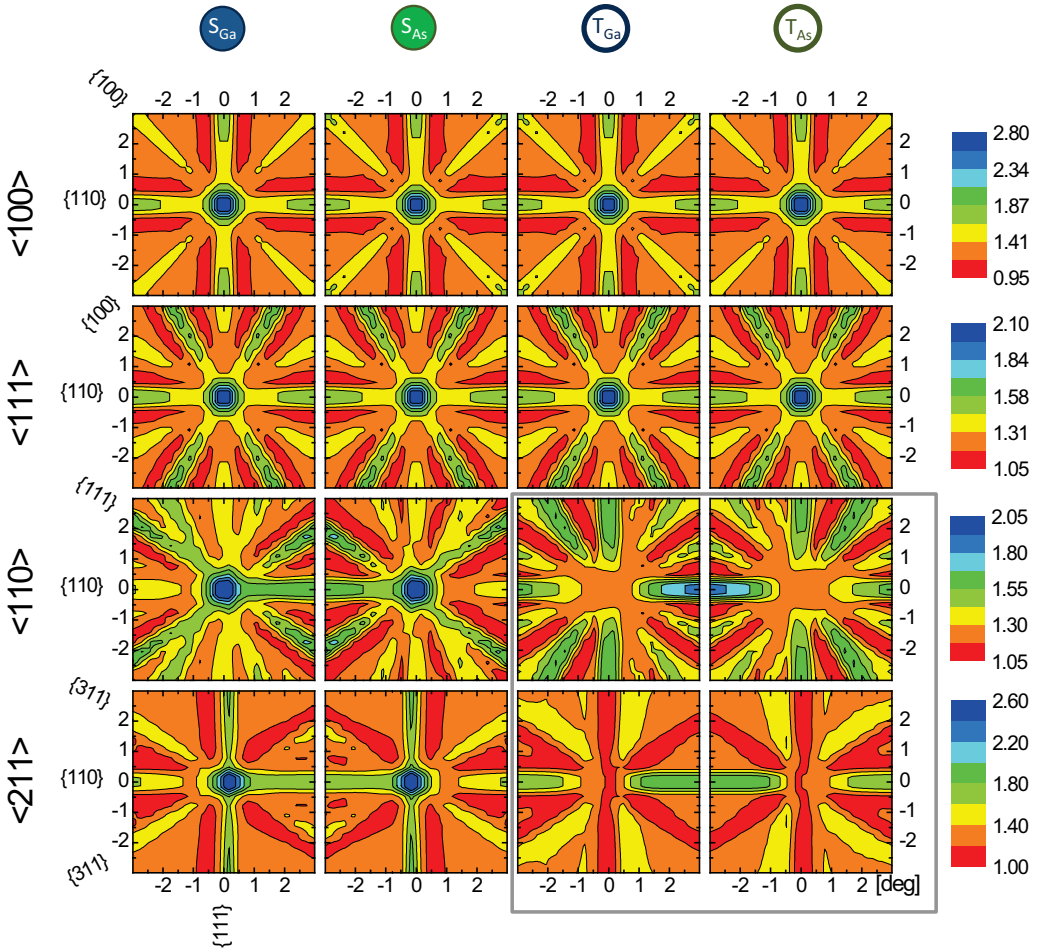

Figure 3.3: Simulated channeling patterns for ^{56}Mn, β^- emitter, on substitutional Ga sites (S_{Ga}), substitutional As sites (S_{As}), and the two T interstitial sites (T_{As} and T_{Ga}) in the GaAs zincblende structure. Note that the patterns for all sites along the $<100>$ and $<111>$ directions are identical because they are located within the same atomic rows for these directions (cf. figure 1.2 on page 10).

Using non-linear least squares fitting routines, *FDD* determines the best fit values of S, f_i, x_0, y_0 and ϕ_0 simultaneously. Parameters x_0 and y_0 are the coordinates of the channeling axis on the detector plane (i.e. the "center" of the pattern) and ϕ_0 is an azimuthal rotation angle of the pattern with respect to the channeling axis. S, x_0, y_0 and ϕ_0 are always allowed to vary in order to provide correct normalization of the experimental spectra and to achieve optimum translational and azimuthal orientation with respect to the detector. Typically only up to three different sites are considered in the fit, as the fitting routine loses sensitivity with increasing number of sites, i.e. with increasing number of f_i degrees of freedom.

3.2.4.3 Scattered electron background correction

In an emission channeling experiment, two types of electrons reach the detector: *direct* and *scattered* electrons. Those with initial direction in the vicinity of the detection axis are *direct* electrons. The number of *direct* electrons is roughly given by the ratio between the solid angle Ω spanned by the detector relative to the beam spot and the full 4π solid angle into which all the electrons are (almost) isotropically emitted, i.e. $\Omega/4\pi$ of the total number of decays. However, the number of detected electrons is always larger than this estimate. The additional *scattered* electrons are not emitted towards the detector initially, but still reach it after being scattered. The scattering event may occur inside the sample, when an electron is scattered by the host atoms, or outside the sample, by setup parts (including backscattering from sample holder). These *scattered* electrons constitute an additional isotropic background in the experimental emission yields, which is not taken into account in the theoretical framework of channeling that is implemented in the *manybeam* program. The problem is different for conversion electrons and β^- particles:

Conversion electron decay. For a pure conversion electron decay, it is possible to deduce the total scattering background from the experimental energy spectrum. While, for direct electrons, the energy spectrum consists of a set of narrow peaks at well defined energies, the scattered electrons form tails at lower energies due to the energy lost in the scatter process. It is thus possible to correct for this scattering background by estimating (integrating the counts in the tails) and subtracting it from the experimental yields.

Beta decay Because such a simple estimate is not possible for β^- decays, with continuous energy spectra, De Vries [94] developed the computer program *Pad* based on the Geant4 toolkit (a set of libraries and tools to simulate the interaction of energetic particles with matter) [95, 96]. Using the Monte-Carlo method, *Pad* simulates the propagation of electrons emitted from the sample and, among the ones that reach the detector, distinguishes the direct from the scattered ones. This requires detailed input information: the sample's geometry and composition, the β^- decay energy spectrum (isotope-specific) and the exact geometry of the setup, i.e. the position, shape and composition of the setup parts. From the *Pad* simulations it is possible to estimate the background correction factor f as:

$$f = \frac{\text{total electrons}}{\text{total electrons} - \text{scattered electrons}} = \frac{\text{total electrons}}{\text{direct electrons}}. \tag{3.4}$$

This f factor can be used to correct the experimental patterns before the fitting or, equivalently, as a rescaling factor of the fractions determined from it.

3.2.5 Experimental details

In this work, two different types of emission channeling experiments are presented: on-line experiments with implantation of radioactive ^{56}Mn and off-line experiments with implantation of ^{73}As. The on-line experiments where performed using the Emission Channeling – Short Lived Isotopes (EC-SLI) setup and measured *in-situ* [88]. The radioactive decay mode for ^{56}Mn is presented in equation (3.5).

$$^{56}\mathrm{Mn} \rightarrow \ ^{56}\mathrm{Fe} + \beta^{-} + \nu_e \tag{3.5}$$

The off-line experiments were performed with the long-lived isotope ^{73}As (decay mode in equation (3.6)), with *off-situ* measurements. For these experiments the setup described in ref. [97] was used, making use of a detector with a different sensitivity, adjusted to the decay rate of ^{73}As. The specific experimental details for each of the EC experiments performed are presented in the following chapter 4, in the corresponding sections.

$$^{73}\mathrm{As} + \beta^{-} \rightarrow \ ^{73}\mathrm{Ge} + \nu_e \tag{3.6}$$

3.3 Superconducting Quantum Interference Device magnetometry

DMS materials are usually in the form of thin films ($< 1\ \mu\mathrm{m}$) or implanted layers, displaying a small magnetic moment which is further decreased by the low concentration of magnetic dipoles and their small magnetic moment (in many cases, only a fraction of a Bohr magneton). The magnetic moment of a typical DMS sample is usually between 10^{-7} and 10^{-4} emu (10^{-10} and $10^{-7}\ \mathrm{A\,m^2}$), thus requiring the high sensitivity of a Superconducting Quantum Interference Device (SQUID) magnetometry.

A SQUID magnetometer measures the magnetic moment of a sample by moving it through a superconducting detector coils. The detector coils are connected to the SQUID through superconducting wires, allowing the current from the detection coils to inductively couple to a SQUID sensor (based on a Josephson junction). As the sample moves through the detection coils, the magnetic moment of the sample induces an electric current in the detection coils. The detection coils, the connecting wires and the SQUID input coil form

a closed superconducting loop. Any change in the magnetic flux in the detection coils produces a change in the persistent current in the detection circuit, proportional to the change in magnetic flux. Since the SQUID works as a highly linear current-to-voltage converter, the variations in the current in the detection coils produce corresponding variations in the SQUID output voltage which are proportional to the magnetic moment of the sample.

In a fully calibrated system, measurements of the voltage variation as the sample is moved through the detection coils provide a highly accurate measurement of the magnetic moment of the sample (with a resolution down to 10^{-8} emu). However, magnetic contamination and measurement artifacts must be carefully taken into account in the range below 10^{-4} emu range. In order for SQUID magnetometry to be used as a reliable tool for the detection of ferromagnetism in DMS materials, it is necessary to develop methods and procedures which ensure that the magnetic signal originating from contamination and other artifacts can be reproducibly kept below a well defined value. Such methods are described in detail in ref. [98].

The SQUID magnetometry measurements presented in this work were performed on rigorously cleaned samples (according to [98]) and consisted mainly in magnetization measurements (a) as a function of applied magnetic field and (b) as a function of temperature. In (a), measurements were performed at 5 K and at room-temperature (300 K) along the easy axis ([100] direction) with applied magnetic fields between -2600 mT and 2600 mT. Saturation magnetization was determined by performing a linear fit at high applied magnetic field. All magnetization curves as a function of applied magnetic field presented in this work were subjected to a fit and corrected to the diamagnetic background of the samples. In (b), remanence and zero-field cool/field cool (ZFC-FC) curves were measured with increasing temperature in the range 5-300 K. Remanence was measured at an applied field of 2 mT, after cooling in a saturating magnetic field – this magnetic field was applied to compensate an eventual negative residual field in the magnet of the SQUID; the ZFC-FC magnetization curves were measured at an applied magnetic field of 10 mT, with the same magnetic field for the field cooling.

4 Results and discussion

This chapter presents the results obtained in this work and their subsequent discussion. It is divided in three parts: first, in section section 4.1, we deal with the identification of the lattice location occupied by the interstitial Mn impurities in ferromagnetic (Ga,Mn)As; second, in section 4.2, we study the thermal stability and diffusion behavior of both substitutional and interstitial Mn impurities in two different concentration regimes – low concentration (1% Mn) and high concentration (5% Mn); and third, in section 4.3, we perform the structural and magnetic analysis of (Ga,Mn)As within the ferromagnetic and secondary-phase regimes (also for 1% and 5% Mn).

4.1 Identification of the interstitial Mn site

As seen in section 1.2.2.1, the interstitial Mn impurities in ferromagnetic (Ga,Mn)As occupy mainly T interstitial sites on the zincblende lattice of (Ga,Mn)As. There are, however, two different T sites, coordinated by different nearest neighbor atoms, Ga or As, and the occupancy of these sites by the interstitial Mn is ambiguous. Emission channeling is an unique technique specially suited to tackle this ambiguity as it provides doubtless distinction between T_{Ga} versus T_{As} sites in the GaAs (zincblende) lattice – a direct structural effect related to the mirror-asymmetry of selected crystal axes (typically $<211>$ or $<110>$) [65]. The EC technique has been previously applied to determine the lattice location of Mn in GaAs in the ultra-low doping regime ($< 0.05\%$ Mn) [64, 65], showing a major occupancy by the interstitial Mn impurities of the T_{As} sites when compared to the T_{Ga}. In this section we address the first objective outlined in chapter 2, i.e. using the emission channeling (EC) technique (described in section 3.2 on page 16), we pretend to determine the exact lattice site occupied by Mn_i in ferromagnetic, high Curie temperature (Ga,Mn)As thin films.

4.1.1 Experimental details

Two separate experiments were performed on the lattice location of radioactive ^{56}Mn (half-life $t_{1/2} = 2.56$ h) implanted into a (Ga,Mn)As thin film grown by molecular beam epitaxy (MBE) [83]. Experiment A consisted of implanting a $Ga_{0.94}Mn_{0.06}As$ thin film (25 nm thick, grown directly on the GaAs substrate) with ^{56}Mn to a fluence of 2×10^{12} cm^{-2}, at an energy of $E = 40$ keV, and a beam angle of $60°$ with respect to the surface normal. The high implantation angle was chosen in order to maximize the fraction of ^{56}Mn probes implanted in the (Ga,Mn)As thin film, i.e. minimizing implantation into the substrate. The near-Gaussian depth profile simulated using SRIM-2008 [99] is characterized by a peak concentration $x_p = 6.2 \times 10^{17}$ cm^{-3} (≈ 0.003 atomic %, i.e. a negligible increase in Mn concentration), a projected range (average depth) of $R_p = 17$ nm and a straggling of $\sigma = 11$ nm, with an estimated $< 27\%$ of the ^{56}Mn probes implanted into the GaAs substrate. Experiment B consisted of implanting a $Ga_{0.95}Mn_{0.05}As$ thin film (200 nm thick, grown on a $200\mathrm{nm}$ AlAs buffer layer, on a GaAs substrate) with ^{56}Mn to a fluence of 7×10^{12} cm^{-2}, with an energy of $E = 30$ keV and an angle of $17°$ (resulting in a peak concentration of $x_p = 2.4 \times 10^{18}$ cm^{-3}, a projected range of $R_p = 21$ nm and a straggling of $\sigma = 11$ nm, i.e. with all the ^{56}Mn probes within the film).

In order to monitor the degree of disorder upon implantation of the radioactive probes and subsequent annealing, we also determined the lattice location of As using radioactive ^{73}As ($t_{1/2} = 80$ d) – experiments C and D. These experiments consisted of implanting similar samples as in experiment B with ^{73}As to a fluence of 5×10^{13} cm^{-2}, with an energy of $E = 50$ keV and an angle of $10°$ (resulting in a peak concentration of $x_p = 1.5 \times 10^{19}$ cm^{-3}, a projected range of $R_p = 26$ nm and a straggling of $\sigma = 13$ nm, i.e. with all the ^{73}As probes within the film).

experiment	ion	annealing	E [keV]	θ [°]	$R_p \pm \sigma$ [nm]	x_p [cm^{-3}]
A	^{56}Mn	3 h air	40	60	17 ± 11	6.2×10^{17}
B	^{56}Mn	10 min vacuum	30	17	21 ± 11	2.4×10^{18}
C	^{73}As	3 h air	50	17	26 ± 13	1.5×10^{19}
D	^{73}As	10 min vacuum	50	17	26 ± 13	1.5×10^{19}

Table 4.1: Summary of the experimental details of experiments A, B, C and D. E represents the implantation energy, θ is the implantation angle, R_p and σ are the projected range and straggling of the implanted ions respectively, x_p is the peak concentration of the implanted layer.

Emission channeling measurements were carried out in the as-implanted state and after annealing at $200°$C: in air for 3 hours in experiments A and C; in vacuum ($< 10^{-5}$ mbar) for

10 min in experiments B[1] and D. Experiments A and B (with relatively short-lived ^{56}Mn) were performed on-line while experiments C and D (with the longer-lived ^{73}As) were performed off-line. Table 4.1 on the facing page summarizes the experimental details for each of the described experiments.

In experiments B, C and D, four axes were measured ($<100>$, $<111>$, $<110>$ and $<211>$), typical of emission channeling experiments on host semiconductors with cubic structure (cf. e.g. [64, 65]). In experiment A, the measurements were limited to the $<211>$ axis, which as will be shown below is sufficient to unambiguously determine the site occupancy (at least when combined with experiment B, where all four axes were measured).

The implantation parameters, film thickness and annealing time of experiment A were carefully chosen to allow us to determine the lattice site(s) occupied by interstitial Mn in a stage of annealing for which approximately half had been removed (correlated with magnetic characterization below (cf. section 4.1.3).

4.1.2 Interstitial Mn site

As a representative example, in figure 4.1 on the next page, (a-h) shows the experimental β^- emission patterns of experiment B after thermal annealing (10 min in vacuum), along the four measured directions (a–d), as well as the best fits of theoretical patterns (e–h).

Similarly, in figure 4.1 on the following page, (i-l) compares experimental patterns (i,j) and best fit (k,l) for experiment A (only the $<211>$ direction), both before and after annealing (3 h in air). In figure 4.1 on the next page, (m-o) qualitatively illustrates how the mirror asymmetry of the {110}-planar channeling measured in the vicinity of the $<211>$ direction (horizontal plane in the figure) allows us to distinguish between T_{As} and T_{Ga} sites: after subtracting from the experimental data the fitted component occupying the substitutional Ga S_{Ga} sites, the asymmetry of the residual {110}-planar channeling corresponds to that of T_{As}, i.e. stronger channeling on the left versus right in (o) of figure 4.1, which is the opposite of T_{Ga}.

Quantitative analysis is provided by numerically fitting the data to calculated patterns, as described in section 3.2.4, from which the fractions of the ^{56}Mn atoms in the different lattice sites are obtained – compiled in figure 4.2 (a) for experiments A and B. Here we observe that while the interstitial Mn fraction is unaffected by the 10 min vacuum annealing (experiment

[1] In this section we consider solely the as-grown and the $200°$C annealing step for the purpose of this experiment. In the next section 4.2 we will consider the remaining annealing steps performed for the detailed diffusion study.

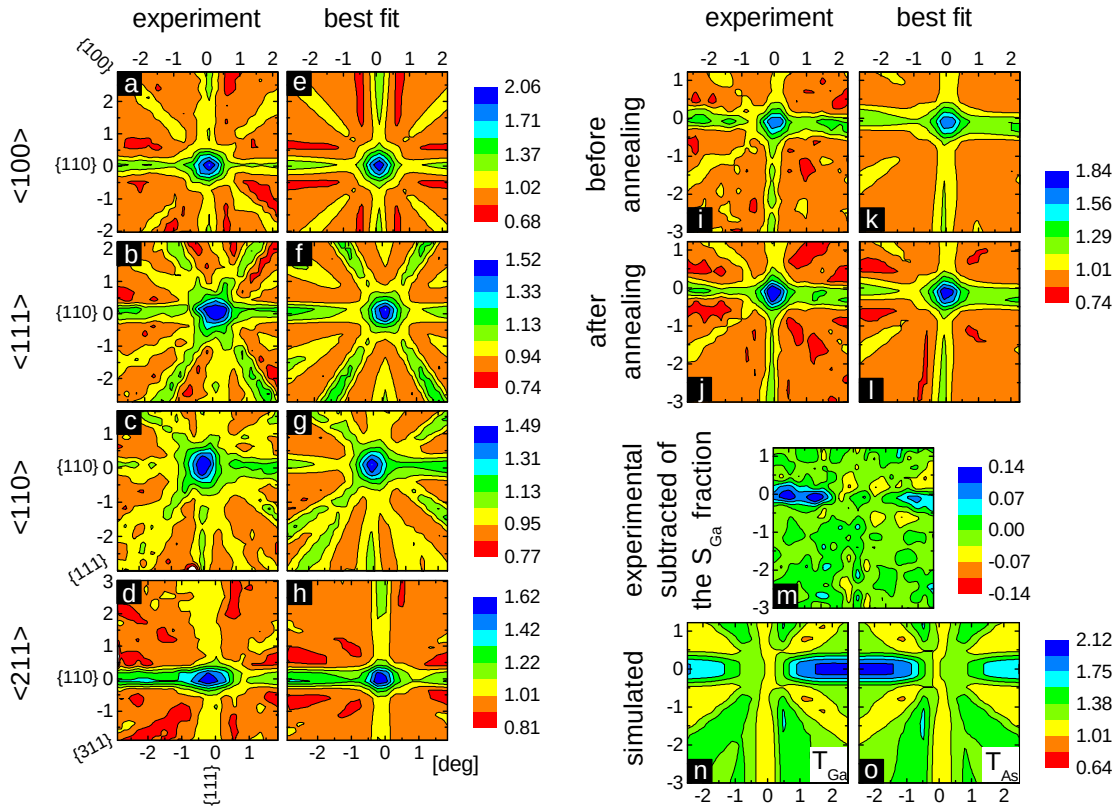

Figure 4.1: (a–d) Experimental β^- emission patterns of experiment B after thermal annealing (10 min, in vacuum), along the four measured directions, and best fits of theoretical patterns (e–h). The best fit is obtained for 71% of the ^{56}Mn atoms on S_{Ga} (Mn_{Ga}) and 25% on T_{As} (Mn_i) sites. (i-l) Experimental patterns (i,j) and best fit (k,l) for experiment A (only the $<211>$ direction), before and after annealing (3 h, in air). The best fits are obtained for 64/77% of the ^{56}Mn atoms on S_{Ga} (Mn_{Ga}) and 25/15% on T_{As} (Mn_i) sites before/after annealing. (m) Experimental pattern (j) after subtraction of the fitted S_{Ga} component. (n,o) Simulated patterns for ^{56}Mn on T_{Ga} and T_{As} sites, respectively.

B), annealing for 3 hours in air decreases it by almost a factor of 2. This is consistent with our magnetometry measurements (cf. next section 4.1.3), and with the Mn_i annealing kinetics previously reported based on transport and magnetometry measurements [44, 17].

We also observe an increase in substitutional fraction upon annealing in both experiments A and B, which we attribute to the recovery of disordered regions (created upon implantation), rather than interstitial Mn being converted to substitutional. This is confirmed by experiments C and D, where we see a comparable increase of the substitutional As fractions (cf. section 4.1.4).

Figure 4.2 (b) illustrates the technique's sensitivity specifically for the case of T_{As} versus T_{Ga} occupancy, by showing for experiment A (after annealing) the error associated with the

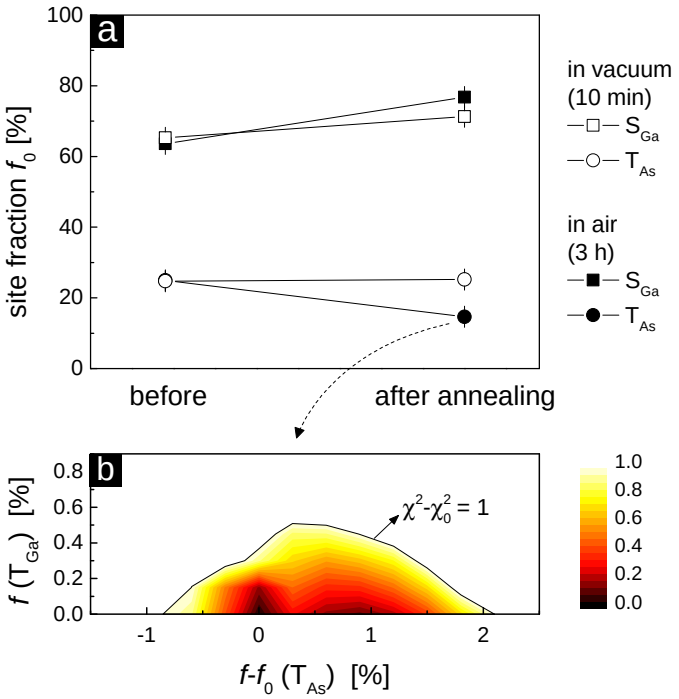

Figure 4.2: a) Fractions of ^{56}Mn atoms on S_{Ga} and T_{As} sites in experiments A and B. b) Error associated with the fit ($\chi^2 - \chi_0^2$, with χ_0^2 being the value for the best fit), for experiment A after annealing, as the fractions f on T_{As} and T_{Ga} sites are varied in the vicinity of the best fit values f_0 (15% for T_{As} and 0% for T_{Ga}), leaving all other fit parameters free. The contour corresponds to $\chi^2 - \chi_0^2 = 1$.

fit (χ^2) as the fractions on T_{As} and T_{Ga} sites are varied in the vicinity of the best fit values (15% for T_{As} and 0% for T_{Ga}, with χ_0^2), leaving all other fit parameters free. The contour corresponds to $\chi^2 - \chi_0^2 = 1$, giving standard deviations of 2% for the T_{As} fraction and of 0.5% for T_{Ga}. Note that the percentages are with respect to all the ^{56}Mn, i.e. even if there is indeed T_{Ga} occupancy within the technique's sensitivity, it is for all purposes negligible. Vanishing T_{Ga} occupancy (with comparable standard deviation) is found both before and after annealing, both in experiments A and B.

It is important to note that the determined site-fractions correspond to the implanted radioactive ^{56}Mn probes, which are not necessarily (and most likely are not) the same as those of the stable ^{55}Mn atoms incorporated during MBE growth. The goal of these experiments was not to determine the absolute fraction of interstitial Mn in (Ga,Mn)As, but to evaluate the stability of the possibly occupied interstitial sites, which we will discuss in section 4.1.5.

4.1.3 Magnetic properties

It is well known from literature that the interstitial Mn (Mn_i) is a *double donor* [100, 62], with self-compensating effects on (Ga,Mn)As: as a donor impurity it compensates holes created by acceptor impurities and by coupling antiferromagnetically (AFM) with substitutional Mn impurities, it compensates the overall magnetic moment [43, 45, 101], effectively reducing the magnetization and Curie temperature (T_C) of the material.

As seen in the previous section, by performing post-growth annealing at a temperature around $200°$C, the Mn_i fraction can be reduced. In experiment A we observe a decrease of the fitted ^{56}Mn interstitial fraction by about a factor of two. In order to correlate this reduction with the magnetic properties we performed SQUID magnetometry measurements on the samples used for experiment A, i.e. on (Ga,Mn)As doped with 6% Mn as-grown and annealed at $200°$C in air.

4.1.3.1 Magnetic anisotropy

In order to accurately estimate the interstitial fraction reduction, we first measured the saturation magnetization of the annealed sample along four magnetically non-equivalent directions: [100]/[010], [110], [$\bar{1}$10] and [001].

direction	M_{sat} $[\mu_B/\mathrm{Mn}]$
[100]/[010]	3.19
[110]	3.03
[$\bar{1}$10]	2.61
[001]	0.13

Table 4.2: Saturation magnetization M_{sat} measured with applied magnetic field along four non-equivalent directions at a temperature of 5 K in (Ga,Mn)As annealed at $200°$C in air.

As shown in table 4.2, the axis in our annealed sample displayed the highest saturation magnetization is the [100]/[010] (in-plane) while the hard axis is out-of-plane [001]. Anisotropy is also found in-plane (cf. sec. 1.2.1): we observe higher saturation magnetization along the [100] direction than the [110] direction. In addition we observe that along two crystallographically equivalent axes we obtain different saturation magnetization values – we observe a higher value for the [110] direction than for the [$\bar{1}$10] direction. A possible explanation for this puzzling anisotropy between two crystallographically equivalent directions is given in ref. [102].

Figure 4.3 on the next page depicts the nearest neighbor Mn dimers residing along a GaAs

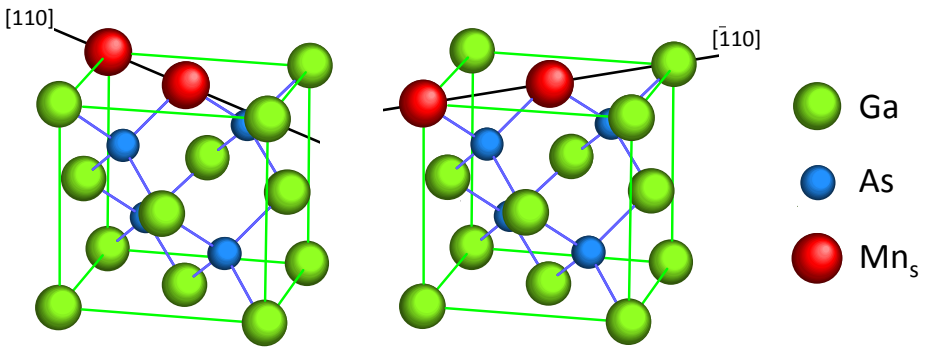

Figure 4.3: Mn dimers on the (001) GaAs surface. If residing along the [110] direction, are not bridged by an As atom. Such bonding exists for [$\bar{1}$10] dimers, resulting in the formation energy.

(001) surface along the [110] and [$\bar{1}$10] axes. In the [$\bar{1}$10] case the two Mn ions are bound to the same As atom, whereas for the dimer along the [110] axis they are connected to different As atoms, implying that these two directions are not equivalent at the surface. In contrast, for bulk dimers there is an As bridge for these two cases – one below, one above the dimer plane. Since the Mn-Mn interaction is brought about by *p-d* hybridization (cf. section 1.2.1) one can expect a higher binding energy for the [$\bar{1}$10] pair compared to the [110] case. Thus, when growing (Ga,Mn)As films, if barriers for Mn diffusion along the surface are sufficiently small, a nonvolatile asymmetry in the pair distribution will set in the whole film during the epitaxy, giving rise to the observed magnetic anisotropy [103].

4.1.3.2 Saturation magnetization and T_C

Determined the easy axis, we now proceed with a detailed magnetic characterization of our as-grown and annealed samples. Magnetization measurements as a function of applied magnetic field at a temperature of 5 K, and as a function of temperature, with an applied field of 1 mT after a field cooling under a saturation field of 100 mT, were performed and are presented in figure 4.4 on the following page. The data presented in this figure has been normalized to the number of Mn atoms present in each of the samples (cf. section 4.1.3.3).

In figure 4.4 (a) we observe a clear increase in the saturation magnetization from the as-grown to the annealed sample, which we will discuss next in terms of Mn_i. In addition, the shape of the hysteresis loop changes, with a dramatic decrease in remanence and coercive field in the annealed sample when compared to the as-grown sample which can be attributed to a changing magnetic anisotropy [54, 103, 104]. In figure 4.4 (b) we represent the measured magnetization as a function of temperature, with an applied field of 1 mT

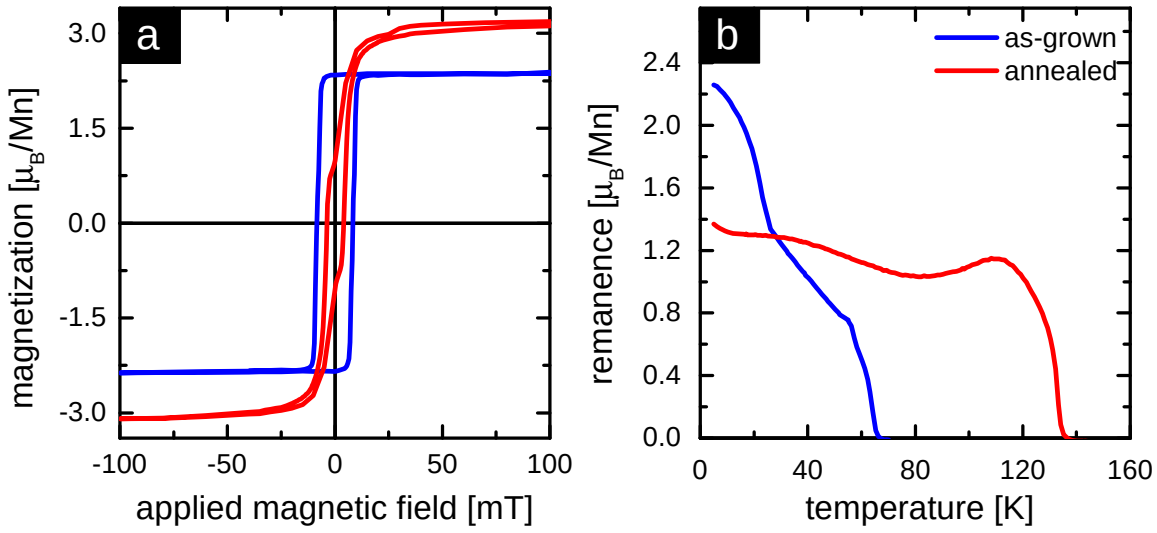

Figure 4.4: Magnetization data before (as-grown film) and after annealing for 3 h in air (experiment B): (a) magnetization as a function of applied magnetic field at 5 K; (b) magnetization as a function of temperature, with an applied field of 1 mT after field cooling under a saturation field of 100 mT.

after field cooling under a saturation field of 100 mT. We observe a clear increase of T_C from the as-grown to the annealed sample, due to the partial removal of Mn_i. The non-monotonic temperature dependence of the magnetization results from the different temperature dependence of the different magnetic anisotropy contributions [54, 103].

4.1.3.3 Estimation of the interstitial fraction

Based on the magnetization data it is possible to estimate the interstitial fraction. In (Ga,Mn)As the Mn impurity atoms occupy mainly substitutional sites, corresponding to a fraction f_s, with a fraction f_i in interstitial sites. The substitutional Mn (Mn_s) fraction contributes to the total magnetic moment of the material while the interstitial fraction compensates this by coupling antiferromagnetically with it. Consequently we can consider that the magnetically active fraction of the sample is then given by $f_a = f_s - f_i$

The net magnetization of a sample, which we measure using e.g. SQUID magnetometry, is $M = N_a\mu$ where N_a is the number of active substitutional Mn moments, i.e. not compensated by interstitial impurities, and μ is the magnetic moment per Mn atom. N_a is then $N_a = Nf$, where N is the total number of Mn atoms in the (Ga,Mn)As film. The value of N

for each sample can be estimated based on the number of Ga atoms N_{Ga} in the film[2]:

$$N = xN_{Ga} = xN_A \frac{m}{M_{\mathrm{GaAs}}} \frac{V_{film}}{V_{sample}} \tag{4.1}$$

where, N_A is Avogadro's number, m is the sample's mass, M_{GaAs} is the molar mass of GaAs, V_{film} and V_{sample} are the volume of the film and the sample respectively. The ratio V_{film}/V_{sample} is given by the ratio of the film's thickness vs. the sample's thickness h_{film}/h_{sample}.

Making use of the relation $f_s + f_i = 1$[3] we obtain $M = \mu N(1-2f_i)$, which can be transformed into:

$$f_i = \frac{1}{2}\left(1 - \frac{M}{N\mu}\right) \tag{4.2}$$

Using the reported magnetic moment per uncompensated Mn impurity $\mu = 4\ \mu_B/\mathrm{Mn}$ [105, 17], and the measured magnetization of the samples, we can obtain the estimated interstitial fractions for the as-grown and for the annealed cases from equation (4.2).

sample	M_{sat} $[\mu_B/\mathrm{Mn}]$	T_C [K]	f_i [%]
as-grown	2.36	67	20
annealed	3.19	137	10

Table 4.3: Experimental details for 6% Mn (Ga,Mn)As as-grown and annealed at $200°$C for 300 hours. Saturation magnetization along the $[100]$ direction M_{sat}, Curie temperature T_C and estimated interstitial fraction f_i

Table 4.3 summarizes the measured saturation magnetization, T_C and estimated interstitial fraction f_i for the as-grown and the annealed sample. As expected, a significant increase of the Curie Temperature from as-grown to the annealed sample is observed as well as an increase in saturation magnetization, yielding a reduction of the interstitial fraction by a factor of 2, in agreement with our emission channeling data (cf. section 4.1.2).

4.1.4 Damage recovery upon annealing

As mentioned in section 4.1.1, experiments C and D (^{73}As emission channeling) were designed to assess the degree of disorder induced upon implantation of the radioactive probes and subsequent annealing, and therefore help the interpretation of experiments A and B.

[2] Since the Mn concentration is quoted with respect to the Ga stoichiometry.
[3] Only substitutional and interstitial positions are occupied by the Mn impurities.

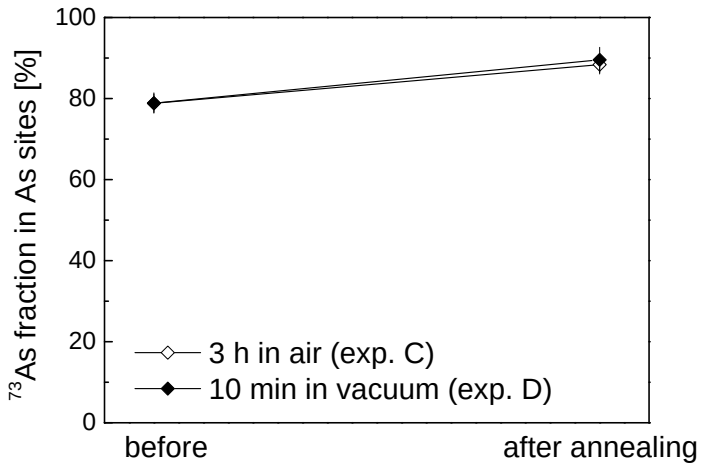

Figure 4.5: Fractions of ^{73}As impurity atoms in S_{As} sites in experiments C and D.

Figure 4.5 shows the fitted fractions of ^{73}As impurity atoms in S_{As} sites in experiments C and D. In both experiments, thermal annealing induces the recovery of damaged regions created upon implantation, leading to an increase in substitutional ^{73}As fraction. An analogous increase was observed for the substitutional ^{56}Mn fraction in experiments A and B, which therefore can also be interpreted as due to lattice recovery, as mentioned in section 4.1.2.

Figure 4.6 (a-d) represents the experimental β^- emission patterns of experiment C before thermal annealing along the four measured directions, and best fits of theoretical patterns (e-h). The best fit is obtained for 79% of the ^{73}As atoms on S_{As} sites whether the reminder 21% is located in low-symmetry sites, most likely in disordered regions created upon ^{73}As implantation.

4.1.5 Interstitial site stability: T_{As} vs. T_{Ga}

The key finding in this section is that interstitial Mn occupies only T_{As} sites, with negligible (if any) T_{Ga} occupancy, for essentially three thermal histories: (a) as-implanted ^{56}Mn at room temperature, (b) after 10 min annealing in vacuum, and (c) after 3 h annealing in air.

In terms of the local structure of Mn_i (in T_{As} sites), there are essentially three possible situations to consider (cf. figure 4.7 on page 38): *isolated* Mn_i (coordinated by As and Ga in the first and second neighbor shell), Mn_i-Mn_s *pairs* (with a Mn_s substituting one of the Ga atoms in the second neighbor shell), and Mn_s-Mn_i-Mn_s *triplets* (with two Mn_s substituting Ga atoms in the second neighbor shell).

Thermal stability (i.e. activation energy for diffusion E_a) increases from isolated Mn to Mn_i-

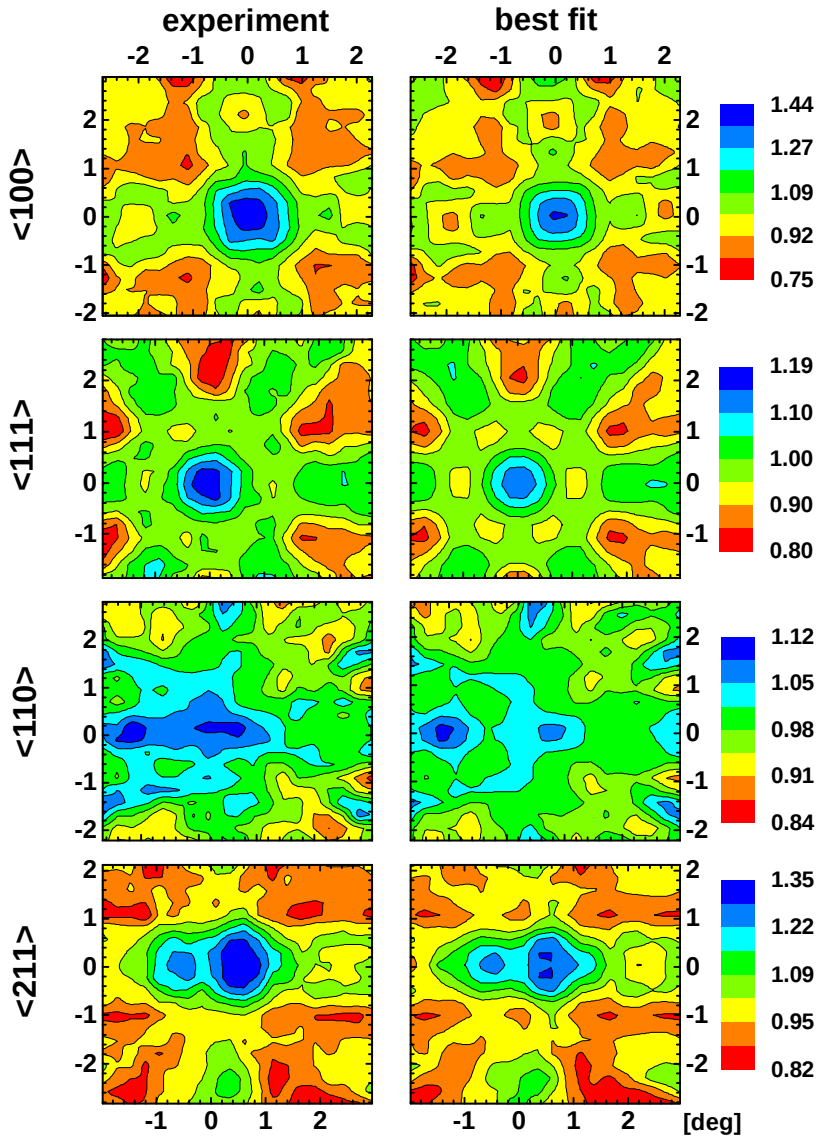

Figure 4.6: (a-d) Experimental β^- emission patterns of experiment C before thermal annealing, along the four measured directions, and best fits of theoretical patterns (e-h). The best fit is obtained for 79% of the ^{73}As atoms on S_{As} sites whether the reminder 21% is located in low-symmetry sites, most likely in disordered regions created upon ^{73}As implantation.

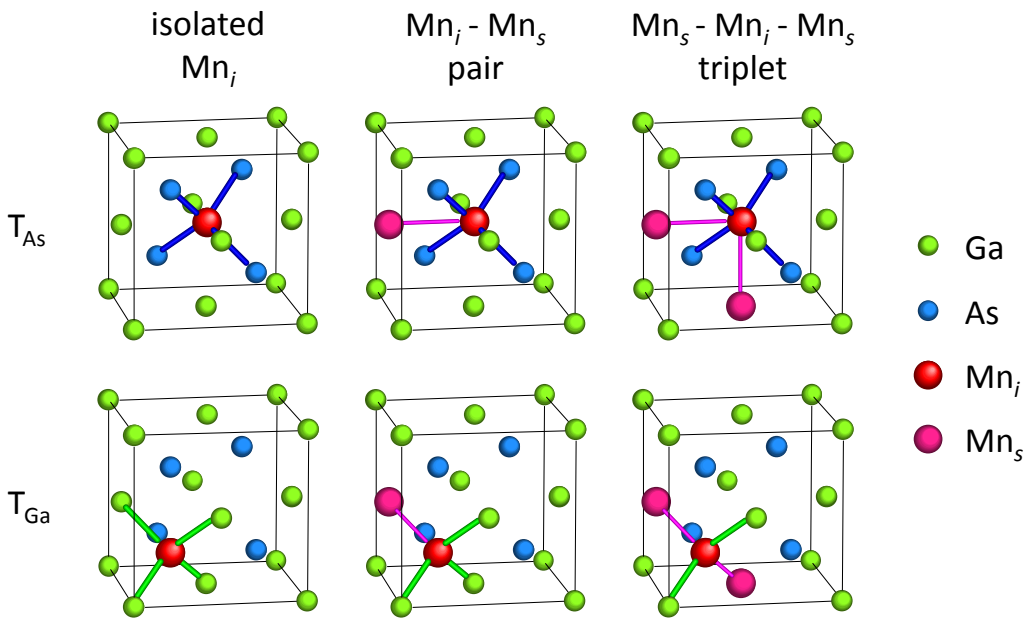

Figure 4.7: Representation of the relevant Mn_i sites and coordination: in T_{As} and T_{Ga} sites for isolated Mn_i, Mn_i-Mn_s pairs and Mn_s-Mn_i-Mn_s triplets. Our data shows that regardless of the coordination, Mn_i always occupies T_{As} sites (top).

Mn_s pairs to Mn_s-Mn_i-Mn_s triplets [71]: $E_a = E_m$ for isolated Mn, with E_m being the effective migration barrier in a T_{As}-T_{Ga}-T_{As} path; $E_a = E_m + E_b$ for pairs and triplets, with E_b being the binding energy of the complexes, which is larger for Mn_s-Mn_i-Mn_s triplets due to the Coulomb interaction between ionized Mn_i donors and the Mn_s acceptors.

Since the ^{56}Mn probes are randomly distributed upon implantation, and long range diffusion of Mn_s and Mn_i is suppressed at room temperature, we can expect the largest fraction of isolated Mn_i in the as-implanted state. However, at $200°$C Mn_i is mobile and, therefore, isolated Mn_i and Mn_i in pairs progressively populate the triplet form (the dissociation of Mn_i from Mn_s-Mn_i-Mn_s triplets is the limiting reaction in the long-range diffusion of Mn_i).

Considering that we observe vanishing T_{Ga} occupancy both before and after annealing, we can conclude that the T_{As} site is the most stable site regardless of Mn_i being isolated, in pairs or in triplets. In other words, regardless of the Mn_s coordination, the migration path of Mn_i between neighboring T_{As} and T_{Ga} sites is asymmetric, with T_{As} being the lower energy side. This picture is in qualitative agreement with previous *ab initio* calculations for the different coordination configurations [71].

An experimental assessment of the different energy barriers at play requires a more detailed investigation of the lattice location as a function of annealing temperature, which will be detailed in section 4.2. T_{As} occupancy is consistent with the expectation of having the Mn

cations (substitutional as well as interstitial) coordinated by As anions rather than charged Ga cations. For Mn_i-Mn_s complexes, however, it could be that the Coulomb attraction between oppositely charged Mn_{Ga} acceptors and Mn_i donors counteracted the repulsion between positively charged Mn_i and Ga cations, making the T_{Ga} site energetically favorable: since the distance between neighboring S_{Ga} and T_{Ga} sites (2.45 Å) is smaller than that between neighboring S_{Ga} and T_{As} sites (2.83 Å), the decrease in Coulomb energy by decreasing the Mn_{Ga}–Mn_i distance could compensate the increase in Coulomb energy of changing the Mn_i coordination to Ga cations. Our data shows that this is not the case, i.e. that the gain in energy associated with having the Mn_i cations coordinated by As anions always dominates, irrespective of the Mn_s coordination.

In short, we have shown that interstitial Mn occupies only T_{As} sites both before and after thermal annealing at $200°$C, which implies that T_{As} is the energetically favorable site regardless of the interstitial Mn atom being isolated or forming complexes with substitutional Mn. This information is crucial for the understanding of electric and magnetic self-compensation in (Ga,Mn)As, as well as the mechanisms of electric and magnetic activation by thermally induced out-diffusion of interstitial Mn.

4.2 Stability and diffusion of Mn

Following our work on the identification of the interstitial Mn site in ferromagnetic (Ga,Mn)As we now address the diffusion of both Mn_s and Mn_i in the materials' matrix in two different concentrations: a low concentration, with 1% Mn, and a high concentration, with 5% Mn.

In order to perform such study we resort to the emission channeling (EC) technique (described in section 3.2 on page 16), determining the lattice location and thermal stability of implanted radioactive ^{56}Mn probes at various annealing temperatures.

4.2.1 Experimental details

In this section we present two experiments on the lattice location and thermal stability of ^{56}Mn (half-life $t_{1/2} = 2.56$ h) implanted into (Ga,Mn)As thin films with different Mn concentrations (1% and 5% Mn). The 5% Mn sample was the same as the one used in experiment B described in section 4.1 on page 27 (200 nm thick, grown on a 200 nm AlAs buffer layer, on a GaAs substrate) and the 1% Mn sample consisted of a (Ga,Mn)As film with a thickness of 1500 nm grown directly on a GaAs substrate.

Both EC experiments were carried out with the same implantation parameters, i.e. implanting ^{56}Mn to a fluence of 7×10^{12} cm^{-2} with an energy of $E = 30$ keV and an angle of 17^{o} (resulting in a peak concentration of $x_p = 2.4 \times 10^{18}$ cm^{-3}, a projected range of $R_p = 21$ nm and a straggling of $\sigma = 11$ nm, i.e. with all the ^{56}Mn probes implanted within the films).

As in our previously reported experiments (cf. section 4.1), a control experiment was devised in order to monitor the degree of disorder upon implantation of the radioactive probes and subsequent annealing, i.e. in order to inspect an eventual layer degradation upon annealing. Accordingly, we determined the lattice location and thermal stability of As using radioactive ^{73}As ($t_{1/2} = 80$ d) implanted into a 5% Mn (Ga,Mn)As sample. The ^{73}As radioactive probes were implanted at a fluence of 5×10^{13} cm^{-2}, with an energy of $E = 50$ keV and an angle of 10° (resulting in a peak concentration of $x_p = 1.5 \times 10^{19}$ cm^{-3}, a projected range of $R_p = 26$ nm and a straggling of $\sigma = 13$ nm, i.e. with all the ^{73}As probes within the film).

The emission channeling measurements were carried out in the as-implanted state and in annealing steps of 50°C (100°C for the ^{73}As experiment) starting at 100°C. Each annealing step was performed in vacuum ($< 10^{-5}$ mbar) for 10 min. Angular-dependent emission patterns were recorded along four crystallographic axes ($<100>$, $<111>$, $<110>$ and $<211>$).

4.2.2 Lattice location and thermal stability

4.2.2.1 Lattice location

As in our prior work on ^{56}Mn lattice location in ferromagnetic (Ga,Mn)As (cf. section 4.1 on page 27), the S_{Ga}+T_{As} double occupancy patterns give by far the best fit to experimental data, showing that the probe atoms indeed occupy mainly the substitutional position with only a fraction in the T_{As} position. Other possibilities for the lattice location of the implanted ^{56}Mn impurities amount to negligible fractions in our fit ($< 5\%$ overall, <1% for T_{Ga} in particular).

When investigating the lattice location of the ^{73}As on 5% (Ga,Mn)As, we identified the substitutional S_{As} site as the best fit to the experimental data, with very small fractions (<5%) in other possible sites.

From these lattice site considerations we fitted all the experimental patterns with calculated ones, determining the site fractions as a function of annealing temperatures. In figure 4.8 we compile the fitted fractions for ^{56}Mn and ^{73}As probes. The discontinuities reflect ^{56}Mn re-implantation (discussed in the following).

4.2.2.2 Thermal stability

Before proceeding to a detailed analysis of the EC experimental data it is important to note that dechanneling of the emitted β^- electrons is enhanced when the radioactive probes diffuse deeper into the bulk of the material. On the other hand, when the radioactive probes diffuse all the way to the surface, channeling breaks down and the β^- emission becomes isotropic. Both these phenomena contribute to an increase in the *random fraction* and a decrease in the *fitted fraction*. Formation of secondary phases will also lead to dechanneling of the emitted electrons, which also contributes to increasing the random fraction.

In figure 4.8 on the facing page we can see that the fitted fractions of the radioactive ^{73}As probes increase up to $300°$C. This increase in the substitutional fraction indicates a recovery of the (Ga,Mn)As structure after the damage caused by implantation. A slight increase in the fitted fractions of ^{56}Mn for both concentrations probed in the same temperature range is also observed.

Analogously to our prior experiments in section 4.1, this increase can therefore be attributed to the increased crystallinity after thermal annealing rather than interstitial-to-substitutional

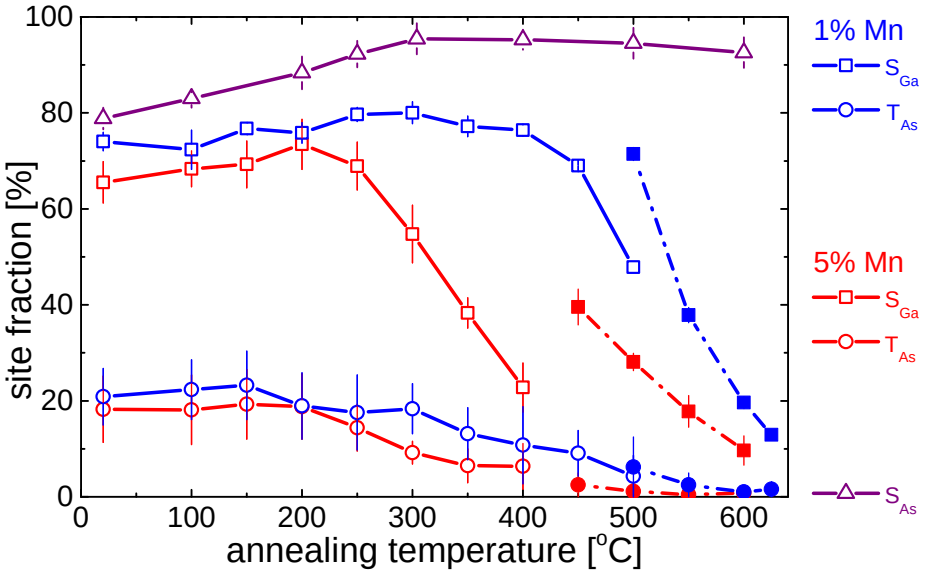

Figure 4.8: Fitted fractions of implanted ^{56}Mn and ^{73}As probes on (Ga,Mn)As samples doped with different concentrations of Mn. The squares represent the fitted substitutional fractions and the circles represent the fitted interstitial T_{As} fractions on the ^{56}Mn-implanted samples. The triplets represent the fitted substitutional fractions for the ^{73}As-implanted sample. Filled symbols represent the same fitted fractions as above after re-implantation of Mn.

conversion. This analysis puts us in a framework in which studying the stability of ^{56}Mn probes in (Ga,Mn)As becomes independent of the structure of the GaAs lattice, which remains unchanged when annealed to temperatures up to $600°$C. In other words, the observed phenomena detailed in the following are intrinsic of the Mn impurities in (Ga,Mn)As.

Turning our attention to the other two curves in figure 4.8, we observe that the fitted fractions of implanted ^{56}Mn probes decrease significantly after certain annealing temperature is reached. For the lower concentration, the ^{56}Mn probes occupying substitutional lattice sites start diffusing at a higher temperature (around 400-$450°$C in 1% Mn) than for the higher concentration (around 200-$250°$C in 5% Mn). The same behavior is observed for the probes occupying the interstitial position. For the 1% Mn case the diffusion temperature is around 300-$350°$C and for the 5% Mn case around 200-$250°$C. This diffusion behavior will be discussed in more detail in section 4.2.3.

4.2.2.3 Secondary-phases and re-implantation

The dramatic decrease in the fitted fractions of the substitutional Mn impurities we observe in figure 4.8 indicates an increase in the random fraction. According to literature,

(Ga,Mn)As forms nanoscale clusters when annealed at high temperatures [76, 77, 78, 81], and therefore we can then assume that this increase in the random fraction is due to the diffusion of substitutional Mn, eventually leading to the formation of secondary phases. This interpretation is consistent with ref. [11], where an optimal annealing temperature was identified ($\sim 200°$C), above which T_C decreases[4]. This was attributed diffusion and aggregation of Mn_s. In section 4.3 on page 55 we address this question in depth.

The formation of secondary phases is further supported by the Emission Channeling data at high annealing temperatures, after re-implanting radioactive ^{56}Mn probes in a regime in which the substitutional impurities have already precipitated into secondary phases. When implanting new probes, these will experience a lower effective concentration of Mn (locally). In other words, the local concentration of Mn impurities will be smaller which translates into less efficient segregation of the newly implanted probes, eventually leading to a higher substitutional fraction and a higher thermal stability (higher segregation temperature). This effect is observed in figure 4.8 on the preceding page by discontinuities in the fitted fraction above 450-$500°$C, temperatures at which we re-implanted ^{56}Mn.

4.2.3 Diffusion of Mn impurities

As seen in section 1.2.2.1, previous emission channeling work [64, 65] addressed the diffusion of Mn in the ultra-dilute regime (<0.05%) in GaAs. In this regime, interstitial Mn (in T_{As} sites) was found to be a free isolated interstitial, i.e. with no substitutional Mn (Mn_s) in the first neighbor shell, becoming mobile above $400°$C with an estimated activation energy of $E_a = 1.7 - 2.3$ eV. In the same studies, the substitutional Mn was found to diffuse at annealing temperatures around $700°$C with an activation energy of $E_a = 3$ eV.

According to our EC experiments described previously, the diffusion of Mn in GaAs doped with several % Mn is strikingly different than for the previously studied case [65]. For increasing Mn concentration in (Ga,Mn)As we observe that both interstitial and substitutional impurities start to diffuse at lower temperatures, with a noteworthy difference between the two regimes under study. We can therefore extrapolate that the mechanism that drives the Mn impurities diffusion is strongly dependent on impurity concentration.

In order to study the diffusion mechanisms in our samples, we estimated values for E_a for the interstitial and substitutional Mn cases, following a model similar to the one used for the ultra-dilute case [64, 65].

[4] The temperature for which the maximum T_C is achieved without secondary phase formation

4.2.3.1 Interstitial diffusion

Arrhenius model for thermally activated migration through interstitial positions

Within an Arrhenius model for the thermally activated migration, the change in fraction $f(T,t)$ of Mn on the T_{As} interstitial sites after an annealing step of duration Δt at a temperature T can be described by:

$$\frac{df(T,t)}{dt} = -\frac{N_t}{N} \tag{4.3}$$

where $N_t = \nu \Delta t$, with ν the jump frequency and Δt the annealing time, and N the average number of jumps a Mn_i atom must perform until it gets immobilized, i.e. until it does not contribute to the site fraction anymore, by diffusing too close to the surface, into the bulk of the material or by being trapped by a low crystallinity region, where dechanneling takes place.

In order to jump from one interstitial site to a neighboring interstitial site, an atom must overcome the potential energy barrier (or migration energy) E_a, as discussed in ref. [71][5]. At finite temperatures, the atom will have sufficient thermal energy to overcome a barrier E_a during a fraction of the time $\exp(E_a/k_BT)$. The jump frequency is then given by:

$$\nu = \nu_0 \exp\left[-\frac{E_a}{k_BT}\right] \tag{4.4}$$

where ν_0 is the attempt frequency, taken as $10^{12}\ \mathrm{s}^{-1}$, i.e. of the order of the lattice vibrations, k_B is the Boltzmann constant and T is the annealing temperature. Applying (4.4) to (4.3) and integrating over the annealing time Δt, we obtain:

$$f(T,\Delta t) = f_0 \exp[-\nu_0 \Delta t/N \exp(-E_a/k_BT)] \tag{4.5}$$

where f_0 is the site (T_{As}) fraction before the annealing step.

By taking $f = f_0/2$, E_a can be estimated through the following expression:

$$E_a = -\frac{1}{k_BT} \ln\left(\frac{N \ln 2}{\nu_0 \Delta t}\right) \tag{4.6}$$

Since no exact value for T when f reduces to $f_0/2$ is directly extractable from our EC data, a lower and upper bound for this value can be taken, leading to an interval for the activation energy E_a. In eq. (4.5) there are two unknown parameters, N and E_a. These parameters cannot be determined independently and therefore N has to be fixed in order to estimate

[5] For an isolated interstitial the limiting factor to its diffusion is a jump between two interstitial positions.

E_a. N is estimated by taking into consideration various diffusion scenarios for interstitial and substitutional impurities.

Diffusion mechanisms of Mn interstitials in (Ga,Mn)As

When a lattice contains at least two types of atoms A and B randomly distributed over the lattice sites, a type A atom will be in a cluster of one, two, three or more A atoms [106]. When growing (Ga,Mn)As samples in the dilute regime, with several % of Mn, the Mn impurities occupy mainly substitutional positions while a small fraction occupies interstitial positions [17]. With increasing Mn concentration, the probability for Mn_s–Mn_i (pairs) and Mn_s–Mn_i–Mn_s (triplets) [44, 71] complexes to be formed increases, leading to different diffusion mechanisms for interstitial Mn. In a concentration regime where both these complexes are present and where sufficient thermal energy has been provided, the interstitial Mn is likely to travel freely through interstitial sites, only becoming *trapped* when captured by these complexes. This will lead to a *hopping* behavior of the diffusing Mn between complexes which in turn leads to different activation energies for each trapping mechanism, affecting the effectiveness of the thermal annealing. The number of jumps N will then depend on the diffusion mechanism.

In the very low concentration regime [65], the interstitial Mn is predominantly a free interstitial, and the number of jumps N is given by the number of interstitial sites the impurity goes through until it is immobilized (cf. fig. 4.9a). At a few % Mn, the scenario changes completely as a significant fraction of the interstitial impurities will be in a pair or in a triangle [106] and the impurity will "hop" between these complexes, as demonstrated in figure 4.9b and 4.9c.

When considering an interstitial diffusion in which the impurity hops between pairs, the number of jumps N is given by the number of complexes the impurity goes through until it becomes immobilized. We do not consider the jumps between interstitial sites because in this scenario the energy required to dissociate a pair is much higher than for free interstitial diffusion, i.e. the intermediate jumps between isolated interstitial sites can be neglected. The same reasoning is applied to triplet complexes, as they are expected to have a higher dissociation energy than a pair [71].

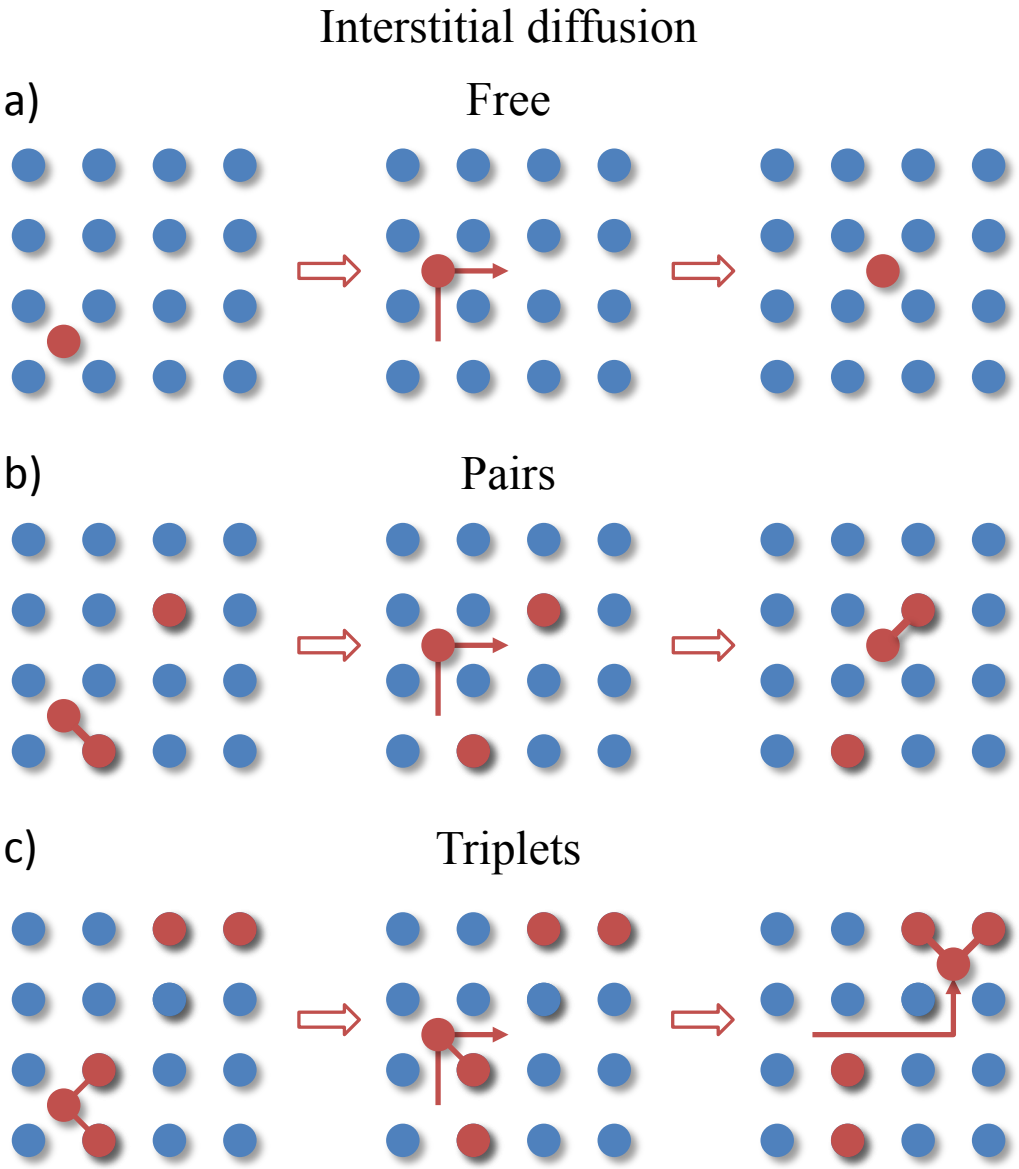

Figure 4.9: The different diffusion mechanisms for an interstitial impurity. In blue are the host lattice atoms and in red the impurity atoms. The number of jumps N is given by the number of a) interstitial sites the impurity runs through until immobilized; the number of "hops" between b) pairs and c) triplets until immobilized.

Number of jumps for interstitial diffusion

Based on these diffusion mechanisms, the number of jumps N can now be estimated as follows.

From ref. [106] we can obtain an estimate of the fraction of impurities in pairs (x_{pairs}) and in triplets (x_{triplets}), using the following expressions:

$$x_{\mathrm{pairs}} = (1-x)^{12} \tag{4.7}$$

$$x_{\mathrm{triplets}} = 12x(1-x)^{18} \tag{4.8}$$

where x is the impurities concentration. Knowing these fractions one can determine the distance between these complexes using:

$$d_i = \sqrt[3]{\frac{1}{c_{Mn}x_i}} \tag{4.9}$$

where c_{Mn} is the concentration of Mn, and $i = (\mathrm{pairs}, \mathrm{triplets})$. For a 3–dimensional random walk, the root mean square (rms) distance from the origin after N jumps is given by

$$\sigma_{3,i} = \left\langle r^2 \right\rangle^{1/2} = \sqrt{N} d_i \tag{4.10}$$

Within the "thin-film" approximation, the impurity distribution is uniform along two of the three directions, and therefore only the jumps in the last direction will contribute to a net diffusivity, i.e. one third of the jumps $N/3$. Expression (4.10) then reduces to:

$$\sigma_{1,i} = \sqrt{\frac{N}{3}} d_i \tag{4.11}$$

When performing the EC experiment the impurities are implanted at a projected range R_p. Long-range diffusion of the impurities has a strong effect on the fitted fractions, due to exponential dependence of β^- dechanneling on the emitter (^{56}Mn) depth. As stated in section 4.2.2.2, the *random fraction* increases when the probes diffuse closer to the surface or into the bulk. Accordingly, for our impurity probes we will take $\sigma_{1,i}$ equal to the projected range R_p.

We can now estimate the number of jumps N for each diffusion mechanisms:

$$N \approx 3\left(\frac{R_p}{d_i}\right)^2 \tag{4.12}$$

Activation energies

When considering the diffusion mechanisms stated above, the activation energy is given by the sum of a *binding* energy E_b and a *migration* energy E_m. The binding energy E_b is the energy necessary to break the bond between the interstitial Mn and the substitutional Mn in pairs or triplets. The migration energy E_m is the energy barrier between interstitial sites ($\mathrm{T_{As}} \rightarrow \mathrm{T_{Ga}} \rightarrow \mathrm{T_{As}}$).

In the very low concentration regime, there is only isolated $\mathrm{Mn_i}$ ($E_b = 0$) and the interstitial does not share any bond with a substitutional impurity. In this case $E_a = E_m$ [65]. At higher concentrations, the increased amount of Mn impurities and the Coulomb attraction between the $\mathrm{Mn_i}$ and $\mathrm{Mn_s}$ favors the formation of complexes. In this case the needed activation energy diffuse the interstitial Mn is given by the binding energy E_b and the mobility energy E_m.

$$E_a = E_m + E_b \tag{4.13}$$

Through EC experiments it is not possible to determine E_b and E_m independently, but it is possible to estimate E_a and infer how the energies vary with different systems.

The estimation of activation energies E_a is, however, not so trivial as depicted above, as other effects can take part in the energy barriers considered. Precipitation into secondary phases will have an effect on the number of jumps the interstitial impurities will perform as well as alter the local impurity concentration. Since an estimate for the number of jumps until an impurity is immobilized by a secondary phase is not possible, we consider the limit case $N = 1$ in our assessment for the activation energies.

		Activation Energies E_a (eV)		
% Mn	T_D (°C)	N_{pairs}	N_{triplets}	N_{limit}
1	$350 - 450$	$1.5 - 1.7$	$1.6 - 1.8$	$1.9 - 2.1$
5	$250 - 350$	$1.3 - 1.5$	$1.3 - 1.5$	$1.6 - 1.8$

Table 4.4: Estimated activation energies for interstitial Mn diffusion

In table 4.4 we compile the estimated values for the activation energy for the interstitial Mn – considering the difference scenarios. We observe that for the 1% Mn sample the activation energies range from 1.5 eV to 2.1 eV while for the sample with 5% Mn the activation energies are $1.3 - 1.8$ eV. For the isolated interstitial in the ultra-low concentration regime [65], the activation energies are $1.7 - 2.3$ eV.

The different diffusion scenarios that may play a role in (Ga,Mn)As have strong implications

in the magnetic properties of (Ga,Mn)As, and at higher concentrations ($x > 5\%$) they can be the limiting factor to the removal of interstitial by thermal annealing [11, 42, 44].

Impurity charge state and charge screening effects

A decrease in activation energy with increasing impurity concentration is observed and it is a consequence of the different mechanisms interplaying in the diffusion of interstitial Mn. As the impurities concentration increases, the interstitial Mn charge state changes [71] as well as the charge screening effects in the host atoms.

Interstitial Mn is a deep donor with three possible charge states: neutral, singly charged or doubly charged [49]. Based on refs. [44, 71] and our identification of the T_{As} lattice site for the interstitial Mn, we expect that this impurity is doubly positively charged. The charge state of the interstitial greatly influences its diffusion, as it determines the strength of its interaction with the host atoms, i.e. the energy barrier for its diffusion is higher with increasing charge state [71].

In the ultra-low concentration regime ($x < 0.05\%$) [65], the isolated interstitial impurity is doubly charged [44, 71] and has the highest activation energy ($1.7 - 2.3$ eV). As seen previously, for this regime $E_a = E_m$ because Mn_i is isolated. In the 1% Mn samples this scenario changes, as the formation of pairs and triplets with Mn_s will add E_b to the activation energy, $E_a = E_m + E_b$. However, we observe significant decrease in activation energy ($1.5-2.1$ eV), further decreasing for the 5% Mn case ($1.3-1.8$ eV). Since the binding energy E_b depends mainly on the atomic species involved, this decrease must be dominated by a decrease in the migration energy, i.e. in the energy barrier interstitial Mn has to overcome.

Naturally, the charge distribution on the host atoms has a strong influence on the diffusion of interstitial impurities and will be dependent on the impurity concentration. This effect can be ascertained by calculating the *Debye length*, $L_D = \sqrt{\varepsilon k_B T/e^2 p}$, where ε is the dielectric constant, k_B the Boltzmann's constant, e the elementary charge and p the hole density. The *Debye length* L_D is the characteristic length beyond which a charged defect is effectively screened.

Taking p determined by Hall-effect measurements [17], the Debye lengths for 1% Mn and 5% Mn are, respectively, 3.7 Å and 1.8 Å. These values are in the same order of magnitude as the nearest neighbor (NN) distance between the T_{As} interstitial site and S_{As} site (2.45 Å), which translates into strong charge-screening effects in these concentration regimes. In other words, a diffusing Mn_i impurity has its charge screened, and therefore has a lower

energy barrier to overcome. As a result, the migration energy E_m is significantly reduced and the activation energy E_a decreases.

Additionally, we observe that in the 5% Mn L_D is smaller than the distance between T_{As} and a S_{Ga} sites, which may lead to a smaller binding energy between pairs and triplets, further reducing the activation energy.

4.2.3.2 Substitutional diffusion

The diffusion of the substitutional impurities in (Ga,Mn)As occurs at higher temperatures and usually leads to the precipitation onto secondary phases. Under the same Arrhenius model as in the interstitial diffusion (cf. sec. 4.2.3.1), the activation energy for substitutional diffusion can be estimated.

The diffusion of substitutional Mn can be modeled by a Frank-Turnbull-like mechanism where the substitutional atom "jumps" from the substitutional site to an interstitial site and diffuses through interstitial sites away from the generated vacancy. For the concentration regimes considered, when the substitutional Mn starts to diffuse the interstitial is already highly mobile, and within the time interval that a substitutional atoms jumps to an interstitial positions, there are many more jumps between interstitial atoms in interstitial positions. Therefore, we can assume that only one jump is required ($N = 1$) to promote the diffusion of substitutional Mn.

% Mn	T_D [°C]	E_a [eV]
1	$500 - 550$	$2.3 - 2.6$
5	$350 - 400$	$1.9 - 2.0$

Table 4.5: Estimated activation energies for substitutional Mn diffusion

In table 4.5 we represent the estimated activation energies for substitutional diffusion. We observe that the activation energy decreases significantly with increasing impurity concentration. This has a strong influence on the thermal annealing procedures to reduce the interstitial Mn for higher impurity concentration as well as it promotes the precipitation into secondary phases at lower temperatures.

Diffusion mechanisms of substitutional Mn in (Ga,Mn)As

The decrease in activation energy for the diffusion of substitutional Mn seems counterintuitive at first as a substitutional impurity just needs to perform one jump to become mobile.

However, the mechanism behind the substitutional impurity diffusion is more complex. In 1984, D. Mathiot and J. Pfister have developed a model based on combination of normal vacancy/interstitial-assisted diffusion and diffusion in a percolation cluster formed by the substitutional impurity atoms [107]. Later in 1993, A. Larsen observed and described the same mechanism for impurities on heavily doped silicon [108]. When a substitutional

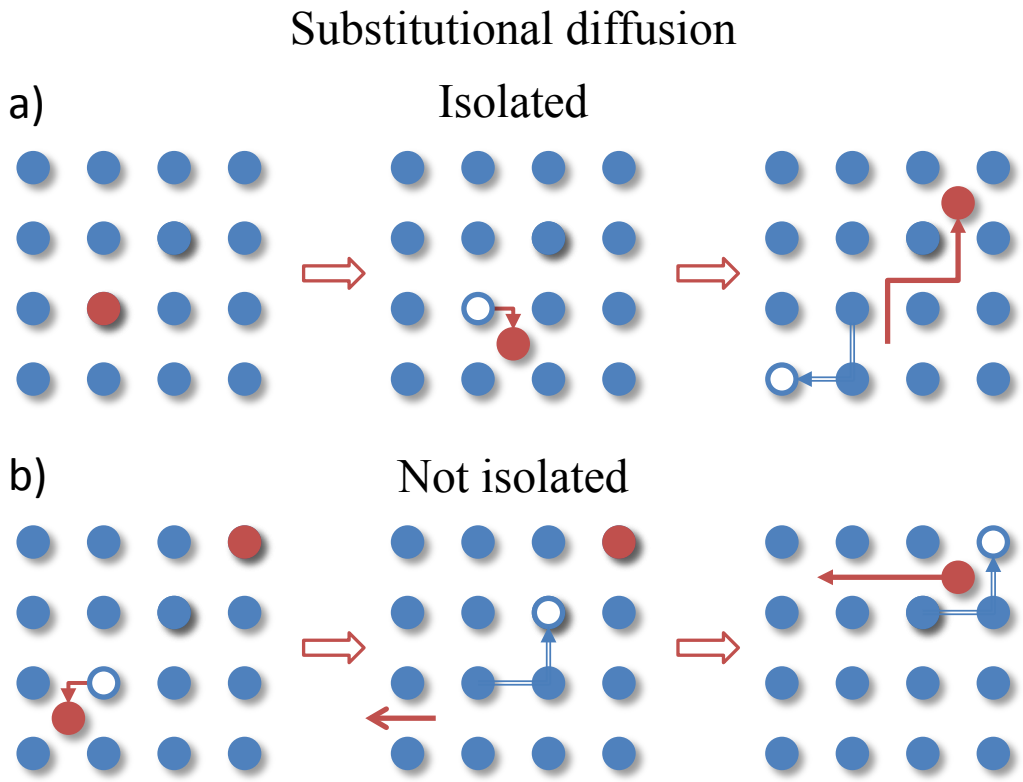

Figure 4.10: Schematic representation of the different diffusion mechanisms for a substitutional impurity. In blue are the host lattice atoms, in red the impurity atoms and in white the vacancies. In the a) isolated case the substitutional impurities are far apart and the vacancy-impurity (V-Mn_s) system has minimum energy. In the b) not isolated case the substitutional impurities are sufficiently close to start a percolation cluster upon diffusion.

impurity jumps from its lattice site, a vacancy-impurity V-Mn_s pair is created with a certain binding energy. This binding energy depends on the distance between the vacancy and the impurity atom. With increasing impurity concentration the distance between substitutional Mn impurities decreases. If substitutional Mn impurities are close enough, the vacancy created when a Mn atom jumps will be attracted to different Mn_s, reducing the effective binding energy in each V-Mn_s pair. Let us consider that for a substitutional impurity to complete one diffusion step the vacancy must diffuse to at least the third-nearest neighbor. If the concentration of substitutional impurity atoms becomes so high that there is a second substitutional atom on a fifth-nearest neighbor position, then the third-nearest neighbor

position, which the vacancy has to diffuse to in order to complete one diffusion step, is also a second-nearest neighbor to a substitutional impurity atom. This results in a lowering of the vacancy potential barrier height equal to the binding energy of the vacancy in the second-nearest neighbor position to the substitutional impurity atom. When a sufficient number of substitutional impurity atoms are connected this way, a percolation cluster will form. Considering that the vacancy can freely diffuse and the energy barrier it has to overcome is lowered, the substitutional impurity atoms will experience an accelerated diffusion via a simple vacancy exchange mechanism.

We hypothesize that it is this impurity-vacancy assisted diffusion, illustrated in figure 4.10, that leads to the observed decrease in the estimated activation energies for the diffusion of the substitutional Mn. By increasing the Mn impurity concentration and reducing distance between substitutional impurities, the energy barriers that vacancies have to overcome decrease, consequently decreasing the energy needed to remove a substitutional impurity from its lattice site.

4.2.4 Implications on the understanding of the structure and magnetism of (Ga,Mn)As

We can conclude that the thermal stability of Mn impurities in (Ga,Mn)As is concentration dependent. We observe that both the substitutional and interstitial fractions decrease at a lower annealing temperature for the 5% Mn when compared to the 1% Mn. This result has two essential consequences: (i) in 1% Mn, reduction of the Mn_i fraction only takes place at an annealing temperature around 400°C; and (ii) in 5% Mn, the substitutional fraction decreases at lower annealing temperatures (slightly above 200-250°C) than reported in literature for secondary phase formation. (i) can be explained by the absence of interstitial in 1% Mn MBE-grown (Ga,Mn)As. In fact, *ab initio* studies in Mn_i compensation [49] show that this impurity is formed upon growth – Mn atoms adsorb on the growing surface and diffuse into the sample. However, we observe that Mn_i is not mobile up to 400°C, providing evidence for the absence of interstitial Mn in (Ga,Mn)As thin films with less than 2% Mn [11, 17]. (ii) represents an unexpected regime for Mn impurity aggregation, presenting a scenario in which Mn impurities precipitate and aggregate at much lower temperatures than reported in literature (above 500°C [73]). Since this low temperature segregation may be the reason why annealing at temperatures little above 200°C leads to a decrease in magnetization and T_C of the material [11], it is important to investigate the properties of (Ga,Mn)As in this new regime in order to further advance the understanding of this dilute magnetic semiconductor.

4.3 Correlating local structure and magnetism

As introduced in chapter 1, (Ga,Mn)As displays different structural and magnetic properties depending on the annealing temperature. For instance, annealing close to the growth temperature partly removes the Mn_i impurities, reducing the lattice constant and increasing T_C along with increasing saturation magnetization and hole density [13, 44, 58, 59, 109]; while annealing at higher temperatures will cause the precipitation of Mn into secondary phases and superparamagnetic clusters [76, 77, 78, 81, 110].

In section 4.2 emission channeling experiments on 1% and 5% (Ga,Mn)As showed different diffusion mechanisms for the interstitial and substitutional impurities with increasing post-growth annealing temperatures. We observed that in 5% (Ga,Mn)As the substitutional Mn (Mn_s) becomes mobile at annealing temperatures between $200°$C and $300\ ^{\circ}$C, while in 1% (Ga,Mn)As this mobility threshold lies between the $400°$C and $500°$C (cf. figure 4.8 on page 43, section 4.2.3). Below these temperature ranges the substitutional Mn does not diffuse and the samples should be ferromagnetic while above it the precipitation into a secondary phase will occur. It is however, important to note that his mobility threshold is connected to the annealing time, through the Arrhenius equation (cf. equation (4.5) on page 45).

The aim of these experiments is to study two different magnetic and structural regimes: *ferromagnetic regime* (FM) and *secondary-phases regime* (SP). In the first regime we investigate the existence of ferromagnetism at low temperatures while maintaining their structure, and in the second we investigate the precipitation of Mn impurities.

In the following sections we will present and discuss these results, with a first section presenting the main results from the experiments on the structure of our (Ga,Mn)As samples (cf. sec. 4.3.2), laying the ground work for the following magneto-structural analysis of the samples in the FM regime (cf. sec. 4.3.3) and in the SP regime (cf. sec. 4.3.4). Within each regime we will analyze each concentration under study, the low concentration (1% Mn) and the high concentration (5% Mn).

4.3.1 Sample description

In order to investigate magnetic and structural properties of (Ga,Mn)As in the regimes previously mentioned, we prepared a series of the same thin film samples of (Ga,Mn)As with 1% and 5% Mn (with the same specifications as in section 4.2.1) subjected to different annealing temperatures.

It is critical to note however, that the diffusion considerations taken in section 4.2 on page 41 were based on the restrictions that come with using radioactive ^{56}Mn in an EC experiment, i.e. the annealing step and subsequent measurements had to be short due to the relatively short lifetime ($t_{1/2} = 2.56$ h) and in vacuum. Consequently, different annealing times have different impacts on the diffusion of Mn in (Ga,Mn)As, as seen from equation (4.5) on page 45 (cf. section 4.2.3.1). Annealing for a longer period of time will shift to lower temperatures the observed diffusion, while annealing in different atmospheres will only affect the passivation efficiency at the surface.

As a result, we studied a set of four samples of each of the concentrations considered in our EC experiment. For each concentration we kept one as-grown sample and subjected three others to thermal annealing at $200°$C and $300°$C for 100 hours in air, and at $600°$C for 10 minutes in vacuum.

4.3.2 Structural characterization

Based on our previous EC study of Mn impurity diffusion on (Ga,Mn)As, we expect the structural properties of our samples to vary upon thermal annealing at different temperatures [39, 84, 111].

To investigate these structural changes in (Ga,Mn)As we performed SR-XRD and EXAFS experiments on each of the samples described in sec. 4.3.1. The experimental details of these measurements are portrayed in chapter 3 on page 15.

4.3.2.1 Synchrotron radiation X-ray diffraction (SR-XRD)

Various measurements were performed on each of the samples:

High-resolution symmetric θ-2θ scans between $15°$ and $80°$ demonstrating the substrate and film peaks with barely no distinction[6] and θ-2θ scans in the vicinity of the (002) peak of GaAs to investigate the film relaxation upon annealing;

Grazing Incidence asymmetrical scans to investigate secondary-phase formation upon annealing.

Figure 4.11 on the facing page shows the reciprocal space maps near the (002) reflection of GaAs, in 5% Mn (Ga,Mn)As as-grown and annealed at various temperatures. From this

[6] Only the relevant part of these measurements is shown

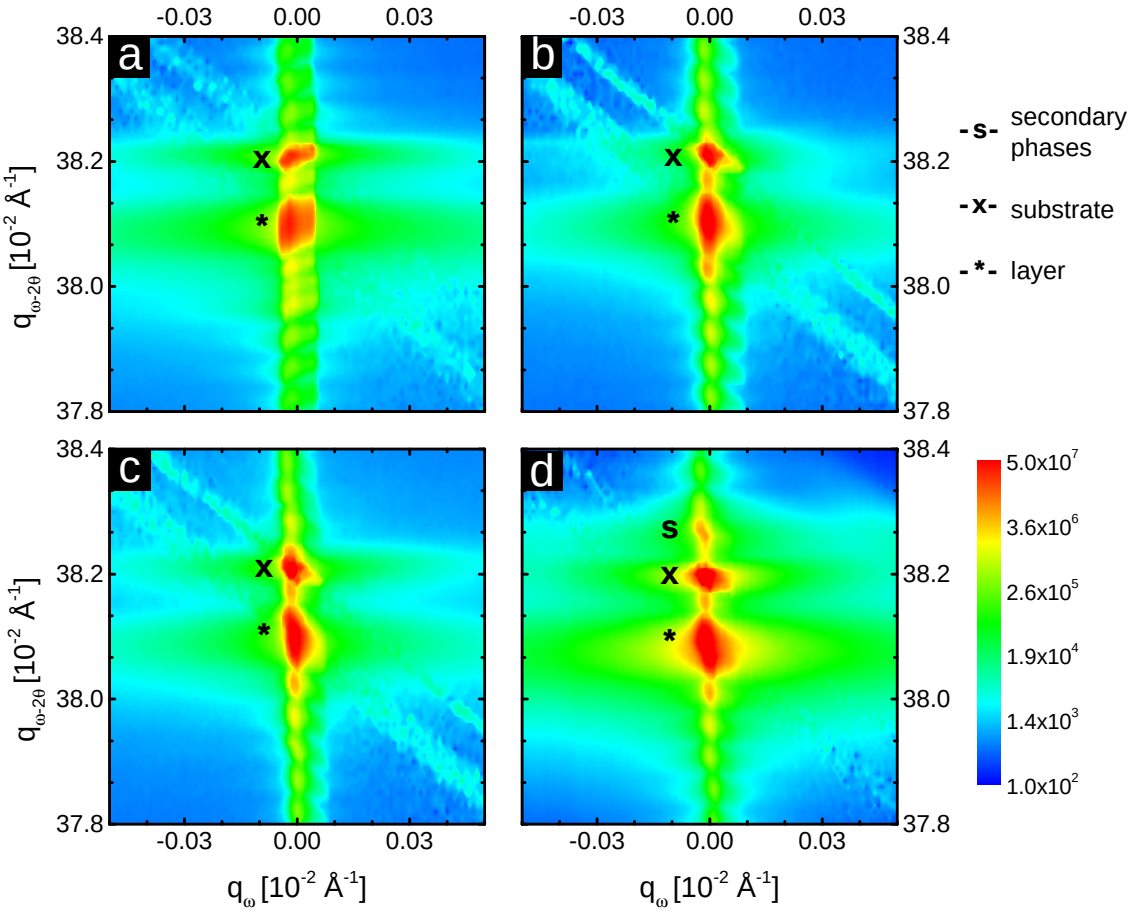

Figure 4.11: Reciprocal space maps near the (002) reflections in the 5% Mn samples: a) as-grown, b) annealed at $200\ ^{\circ}\mathrm{C}$, c) annealed at $300\ ^{\circ}\mathrm{C}$, and d) annealed at $600\ ^{\circ}\mathrm{C}$. The symbols X, * and S represent respectively the substrate, layer and secondary phases peaks.

reciprocal map we can obtain the high resolution θ-2θ scans, shown in figure 4.12 on the next page, for both concentrations – 1% Mn (left) and 5% Mn (right). In this figure, the peaks S, L and SP denote respectively the substrate peak, the (Ga,Mn)As peak and the secondary phases peak. This data will be detailed in sections 4.3.3.1 and 4.3.4.1.

Figure 4.13 on page 59 shows the GIXRD measurements with all the identified secondary phases for the samples annealed at $600^{\circ}\mathrm{C}$: MnAs in two distinct phases (zincblende and hexagonal) and orthorhombic As. These secondary phases will be discussed in more detail in section 4.3.4.1.

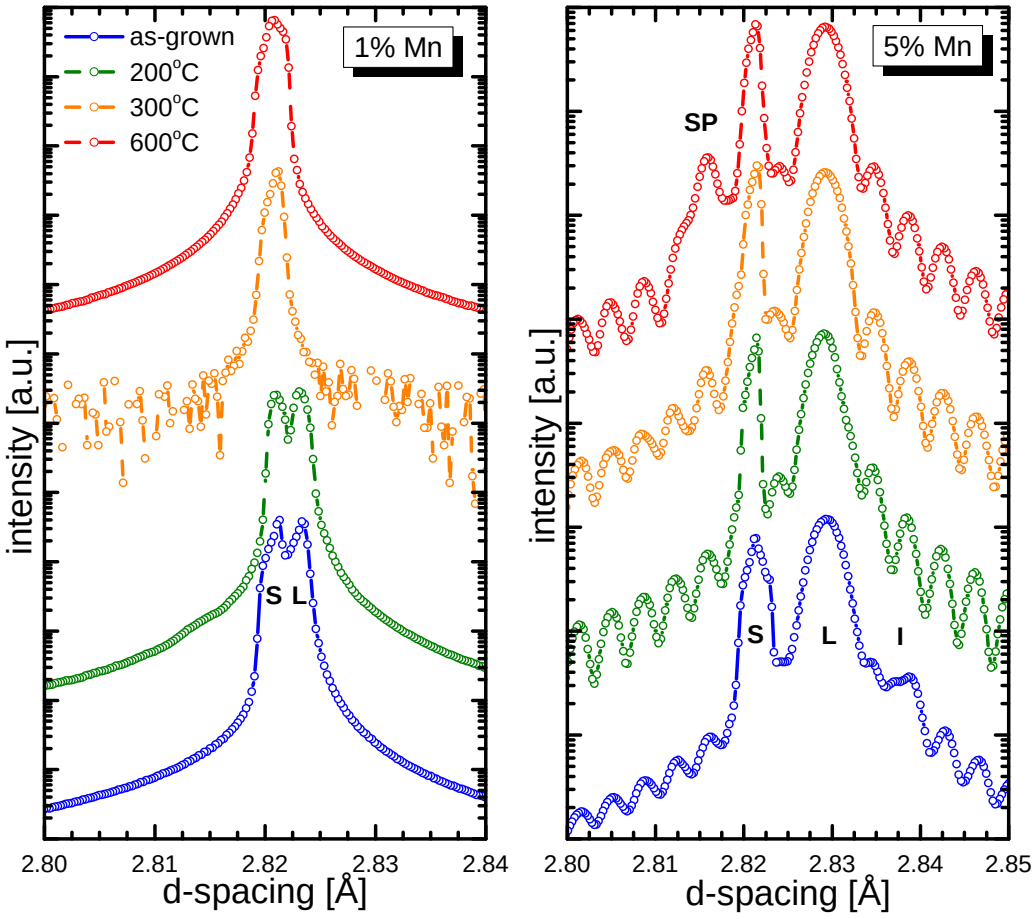

Figure 4.12: SR-HRXRD measurements around the <002> peak of GaAs on (Ga,Mn)As samples with 1% Mn and 5% Mn as-grown and annealed at $200°C$, $300°C$ and $600°C$. S, L, I and SP represent respectively the substrate and the film peaks, the interstitial and the secondary phases peaks.

4.3.2.2 Extended X-ray absorption fine structure (EXAFS)

The EXAFS experiment was carried out at BM26, ESRF, and consisted on the room-temperature study of the X-ray absorption near the K-edge of the Mn impurities. Figure 4.14 on page 60 shows the Fourier transform of the isolated fine structure as a function of non-phase corrected radial distance for Mn atoms in a (Ga,Mn)As matrix.

Figure 4.15 on page 61 summarizes the outcome of a 1^{st} shell analysis, allowing us to determine the Mn-As NN distance as well as the EXAFS Debye-Waller (DW) factor σ^2, which in turn gives us insight into the local structure of Mn impurities in (Ga,Mn)As, in particular, on the local disorder in these systems.

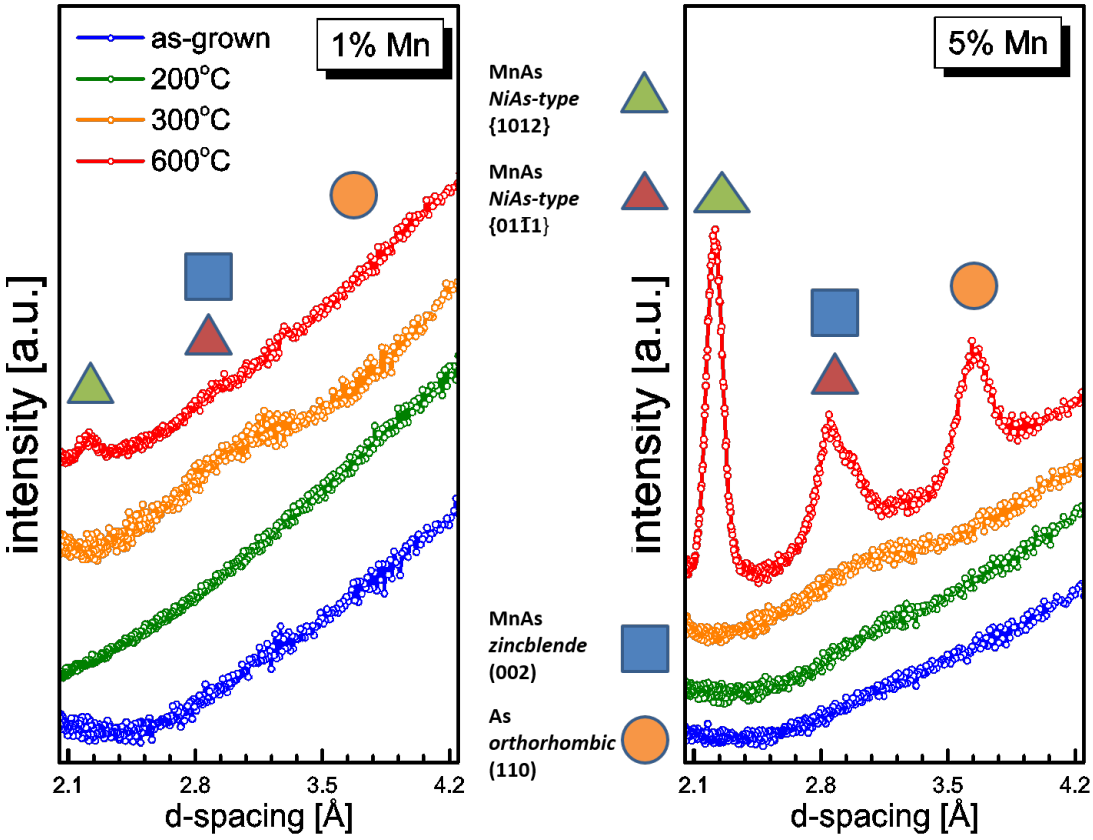

Figure 4.13: SR-GIXRD measurements (Ga,Mn)As samples with 1% Mn and 5% Mn as-grown and annealed at $200°$C, $300°$C and $600°$C. The emergence of secondary-phases peaks is evident for the samples annealed at $600°$C in the selected scan range and is represented by triangles for *NiAs-type* MnAs nanoclusters and by squares for *zincblende* MnAs nanoclusters. A peak corresponding to an *orthorhombic* As phase is also present and represented with a circle. Only the region of interest is displayed with no more peaks corresponding to secondary phases present in the remaining spectrum.

4.3.2.3 Remarks

The results presented in this section (4.3.2) set the ground work for a complete magneto-structural analysis of (Ga,Mn)As with 1% Mn and 5% Mn annealed at various temperatures. As is observable from these results, the structural changes in (Ga,Mn)As in the FM regime are small, since the removal of the interstitial has little effect on the overall structure.

Stronger structural modification is observed for the samples annealed at $300°$C and $600°$C. An increase in NN distance as well as in the EXAFS DW factor σ^2 in the EXAFS analysis (cf. fig. 4.15) indicate the formation of disordered Mn-rich regions at $300°$C and well defined crystallized secondary phases at $600°$C. In the SR-XRD measurements we observe a disappearance of the (Ga,Mn)As peak in the 1% Mn samples at $300°$C and $600°$C, and

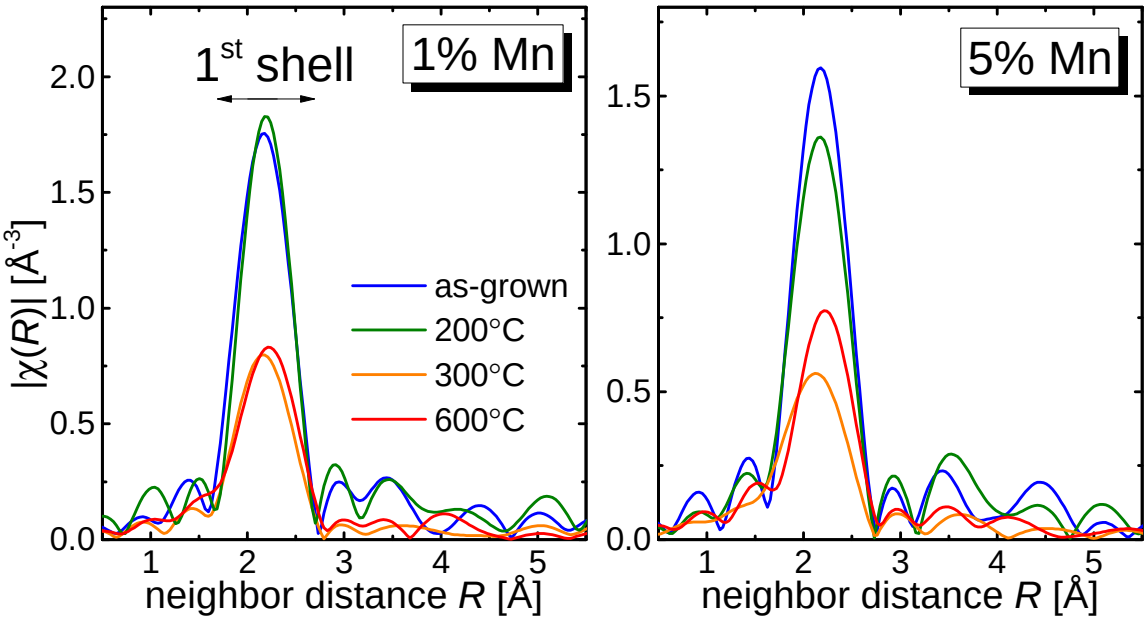

Figure 4.14: Spectra of the Fourier transform of the isolated fine structure as a function of non-phase corrected radial distance for Mn atoms in a (Ga,Mn)As matrix for different Mn concentrations.

an emergence of a secondary phase peak in the 5% Mn samples at $600°$C (cf. fig. 4.12).

These structural changes will be discussed in more detail in the following sections 4.3.3.1 for the ferromagnetic regime and 4.3.4.1 the for the secondary phase regime followed by their implications on the magnetic behavior.

4.3.3 Ferromagnetic regime

In section 4.2 we saw that the diffusion of Mn_i occurs at lower temperatures than Mn_s. Annealed below the diffusion temperature of Mn_s, (Ga,Mn)As should still be ferromagnetic, with small structural changes from the as-grown state.

From a magnetic point of view, the interactions that allow the existence of ferromagnetism in each concentration in this regime are different: in the low concentration ($x < 1.5\%$) the holes that mediate the magnetic interactions between Mn_s moments lie in an impurity band [42, 50] while in the higher concentration regime ($x > 1.5\%$) this impurity band is merged with the valence band [50, 112], leading to a ferromagnetic $p-d$ Zener exchange interaction. This is however a controversial point in the DMS field, specifically for (Ga,Mn)As [50].

However, in both these regimes the Mn interstitial can be present and couple antiferromagnetically with the substitutional impurities. Within the FM regime we intend to study the Mn

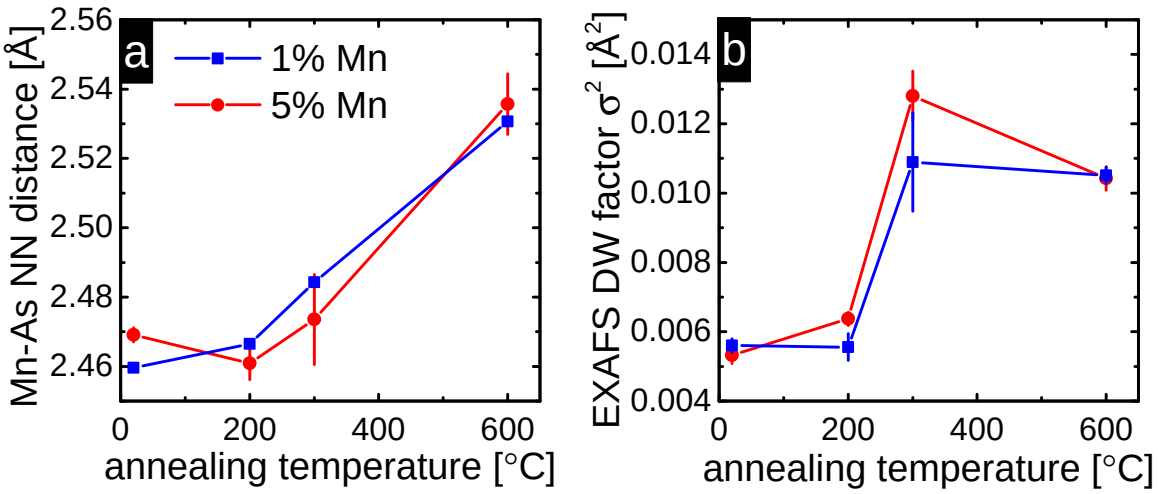

Figure 4.15: a) The best fit distance to the first nearest neighbors of Mn impurities in (Ga,Mn)As as a function of annealing temperature; b) the fitted EXAFS Debye-Waller factors for the first single scattering path of Mn absorbers in a (Ga,Mn)As crystal matrix as a function of annealing temperature.

interstitial removal by annealing close to growth temperature ($200\ ^{\circ}\mathrm{C}$) in both concentrations and analyzing the material's structure and magnetism. Therefore, in this section we will distinguish samples by *as-grown* and *annealed*, where *annealed* refers to the samples annealed at 200°C in air for 100 hours.

4.3.3.1 Structure

Within the FM regime we already noted that the structural changes are minimal. However it is worthy to evaluate these changes in order to draw a valid magneto-structural picture of (Ga,Mn)As.

From our SR-XRD experiments we observe that the measurements of the as-grown and of the annealed samples held similar results. The GIXRD measurements (figure 4.13 on page 59) showed no secondary phase formation, with no additional peaks present in the full scans, which was expected as in this temperature regime Mn_s is not mobile.

In figure 4.12 on page 58, however, small changes are observable at 5% Mn. In this concentration we observe that the layer peak (L) becomes sharper upon annealing with better defined interference fringes[7]. Also, the region where the apparent peak I resides disappears within the fringes. These differences in the experimental curves between the samples seem to indicate a small change in the structure of 5% (Ga,Mn)As when annealed

[7]These fringes are a result of the interference between the diffracted X-rays from the buffer layer with the diffracted X-rays from the (Ga,Mn)As layer.

close to the growth temperature.

As seen in section 1.2, interstitial Mn does not form when growing (Ga,Mn)As for concentrations below 2% Mn. Therefore, no change is expected in the material when annealed at $200\ ^{\circ}\mathrm{C}$. This is also visible in our HRXRD data, in figure 4.12 on page 58 where the as-grown and annealed scans display the same peaks with similar intensities.

4.3.3.2 Magnetism

By performing SQUID magnetometry measurements we are able to analyze the magnetic properties of our samples, most importantly the *Curie temperature* T_C, saturation magnetization, remanence and coercivity.

In order to determine these properties, we measured for each sample the magnetization as a function of applied magnetic field at 5 K and at $300\ \mathrm{K}$, the magnetization as a function of temperature at an applied field of 10 Oe after cooling under a saturating field (remanence curves), and magnetization as a function of temperature at an applied field of $100\ \mathrm{Oe}$ after a zero-field cooling and a 100 Oe field-cooling at the same magnetic field. All measurements were performed along the same direction as the applied magnetic fields, the [100]/[010].

For each concentration we obtained different results and accordingly we will divide the analysis in low concentration (1% Mn) and high concentration (5% Mn).

Low concentration

In figure 4.16 we can observe the M-H and M-T curves measured for 1% Mn in the FM regime. The as-grown sample as well as the annealed sample display ferromagnetic behavior with a saturation magnetization of $3.5\ \mu_B$, very close to the magnetization of uncompensated substitutional Mn, $4\ \mu_B$ (cf. [49]).

Both the ZFC-FC curves and the remanence present a peak in magnetization at around 17 K. This may be due to a changing magnetic anisotropy, which has been shown to be temperature dependent [102, 103].

No significant change is visible in the magnetic properties of 1% (Ga,Mn)As when comparing the as-grown with the annealed sample: the saturation magnetization remains the same ($M_{sat} = 3.5\ \mu_B$) as well as the Curie temperature ($T_C = 20\ \mathrm{K}$) at which the paramagnetic transition occurs. This further supports our emission channeling conclusion (cf. section 4.2.4) that interstitial Mn impurities do not form upon growth for this concentration

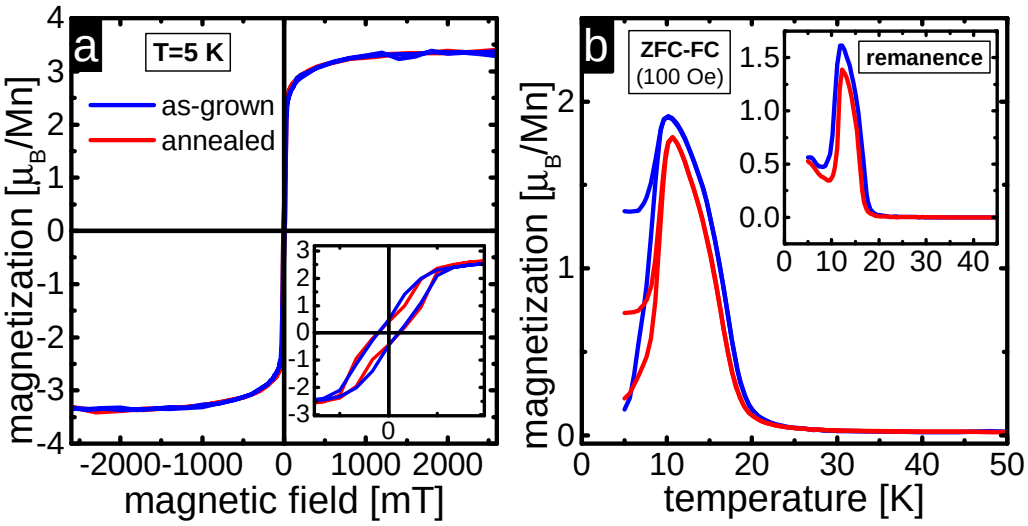

Figure 4.16: (a) Magnetization as a function of applied magnetic field; (b) ZFC-FC curves and remanence (inset) as a function of temperature for as-grown and $200°$C air annealed 1% (Ga,Mn)As.

regime[8], and therefore no Mn_i impurities are there to be removed when annealing.

High concentration

Figure 4.17 displays the results of SQUID magnetometry on the 5% Mn samples in FM regime. We observe a considerable increase in saturation magnetization from $2.4\ \mu_B$ to $3.6\ \mu_B$ from the as-grown to the annealed sample, accompanied by an enhancement of T_C from 50 K to 100 K (cf. figure 4.17b). This is due to the removal of Mn_i from the complexes considered in section 4.2.3.1), leaving more substitutional Mn impurities isolated, which in turn contribute to the net magnetization of the material. The coercive field as well as the shape of the hysteresis loops change significantly, indicating the changing magnetic anisotropy upon annealing.

As we can see in the metallic regime, post-growth annealing close to growth temperature can effectively promote the out diffusion and passivation of Mn_i contributing to an activation of the substitutional Mn and enhancing the magnetization and Curie Temperature.

[8] as it is not mobile at temperatures around $200°$C

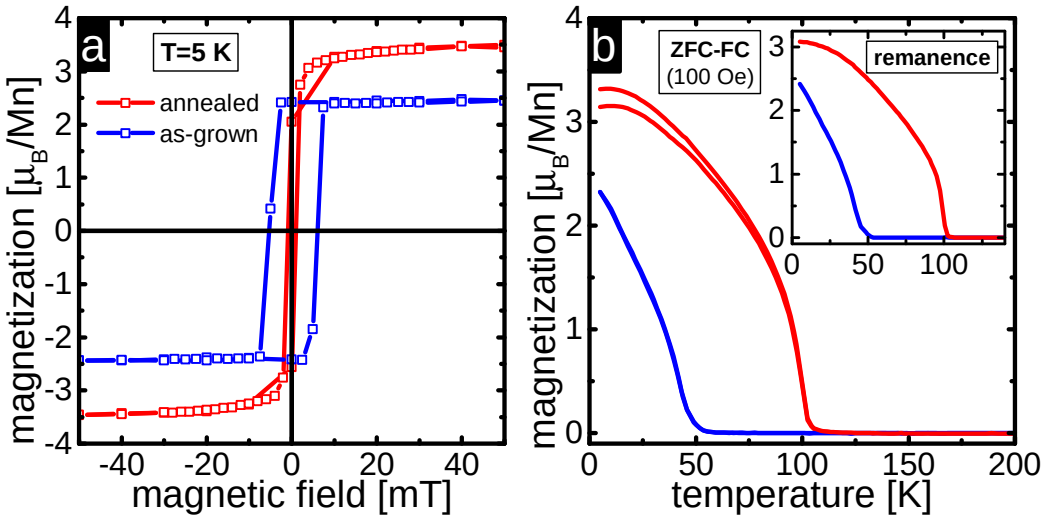

Figure 4.17: (a) Magnetization as a function of applied magnetic field; (b) ZFC-FC curves and remanence (inset) as a function of temperature for as-grown and $200°$C air annealed 5% (Ga,Mn)As.

4.3.3.3 Concentration dependence

In section 4.2.2 we saw that by annealing at a temperature around $200°$C the substitutional Mn impurities are not completely mobile for both concentrations under inspection, i.e. while in the 1% Mn samples the Mn_s is not mobile at $200°$C, in the 5% Mn samples some residual precipitation may have already occurred.

We also note that, as seen in section 1.2.2, annealing at this temperature will promote the diffusion of the interstitial Mn, passivating it at the surface and thereby we expect to see an increase in the net magnetization of our samples as well as their Curie Temperatures.

In figure 4.18 we compare the obtained magnetization curves for both concentrations for as-grown samples as well as for annealed samples within the FM regime. We observe that the 1% FM samples have a comparable net magnetization to the $200°$C annealed 5% Mn sample. As seen in sec. 4.2.4 and according to literature [17, 44], for Mn impurity concentration below 2% Mn the interstitial impurity does not form. With no self-compensation by the Mn_i impurities in the 1% Mn samples, the total magnetic moment per Mn impurity shall be close to the theoretically predicted value of $4\ \mu_B$ [105]. However, in a low concentration regime, where the sample is insulating, the amount of holes to mediate the ferromagnetism is smaller than at higher concentrations, therefore limiting the net magnetization of the sample. Also, the lower concentration of Mn_s defects results in a lower T_C, as seen in figure 4.18.

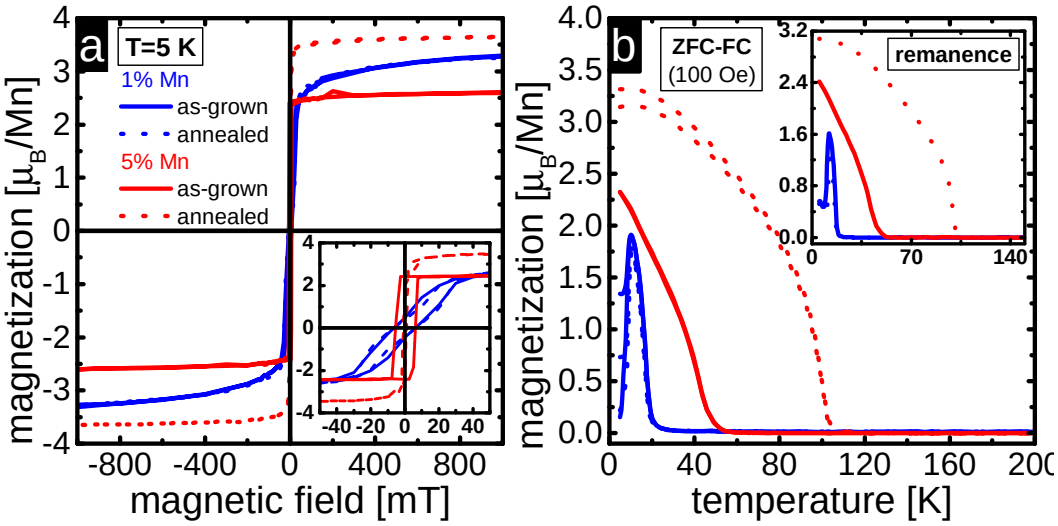

Figure 4.18: Magnetization curves for 1% and 5% (Ga,Mn)As samples as-grown and annealed respectively at $200°$C.

Another noteworthy observation is the anisotropy of the system in the two different concentration regimes: along [100]/[010] the magnetic hysteresis is disparate for the 1% Mn samples from the 5% Mn samples. The different magnetic anisotropy properties of the samples in both concentrations are mostly due to the different magnetic ordering mechanisms as described in section 4.3.3.

4.3.4 Secondary-phase regime

4.3.4.1 Structure

While for higher temperature annealing temperatures ($500°$-$600°$C) it is generally accepted that Mn precipitates into a secondary phase [76, 82], the low temperature regime (between $200°$C and $400°$C) is still poorly understood.

For the samples annealed at $300°$C, the GIXRD measurements did not reveal additional peaks, and the HRXRD measurements show the disappearance of the film peak L in the 1% Mn sample when compared to the samples within the FM regime[9]. This is indicative of a relaxation of the film to the GaAs lattice constant. Indeed, in figure 4.15 on page 61 we observe a slight increase in Mn-As NN distance, with a significant increase on the DW factor σ^2, which together indicate that the Mn impurities are forming disordered Mn-rich

[9]This measurement shows a higher background noise than all the others due to experimental difficulties during alignment

regions when the material is annealed at $300^{\circ}\mathrm{C}$, possibly without formation of a well defined secondary phase.

In the 5% Mn sample, the L peak is present in all measurements, but this is not indicative of the presence of the (Ga,Mn)As layer. Indeed, in the FM regime, this peak is due to the presence of the (Ga,Mn)As layer but is as well due to the presence of the buffer layer of AlAs. When the Mn impurities start to diffuse and form secondary phases, the intensity of this peak will be reduced as the film relaxes and only the AlAs layer will contribute for its intensity.

In samples annealed at 600°C we observed well defined secondary phases in both sets of samples (1% Mn and 5% Mn). On figure 4.12 a new peak (SP) has appeared on the left side of the substrate peak S in the 5% Mn sample, in contrast with other measurements on the same concentration. This new peak can be attributed to the formation of nanoscale clusters of MnAs. According to literature [78], the (Ga,Mn)As lattice relaxes to the GaAs lattice constant, with the Mn aggregation in nanoclusters with a smaller lattice parameter. This translates to a shift of the peak to higher angles or smaller interplanar distances. This peak SP has two possibilities consistent with literature: (a) it coincides with the peak $\{011\overline{1}\}$ for bulk hexagonal α-MnAs (*NiAs*–type), with $d = 2.793$ Å; and (b) it coincides with peak (002) of *zincblende*–type (ZB) MnAs. These small nanoclusters are strained relatively to the bulk α-MnAs for (a) and for ZB–type MnAs, displaying a reduction in d-spacing of 0.88% and $-.34\%$ respectively.

In the same figure, in 1% Mn such a peak is not visible, however the substrate peak becomes broader when compared to the measurement of the 300°C annealed sample. This may indicate that the formed nanoclusters have a smaller size and therefore induce less strain in the host lattice.

From figure 4.15, we observe that for an annealing temperature of 600°C the Mn-As NN distance is approximately $d_{NN} = 2.53$ Å with a DW factor $\sigma^2 = 0.011$ Å^2, which is very close to the Mn-As NN distance in bulk α-MnAs ($d_{NN,MnAs} = 2.57$ Å). This unambiguously provides evidence for the formation of a MnAs secondary phase when subjecting (Ga,Mn)As to a high temperature annealing of $600^{\circ}\mathrm{C}$.

Furthermore, from our measurements in GIXRD we were able to identify the different phases present in each of the studied samples. In figure 4.13, these phases are signaled with shapes (square, triangle and circle) and can be investigated. In the 1% Mn sample, we mainly were able to identify one MnAs secondary phase, corresponding to the $\{10\overline{1}2\}$ peak of *NiAs*–type MnAs clusters, i.e. nanoclusters of MnAs with hexagonal NiAs–like

structure. The presence of zincblende (ZB) nanoclusters could not be confirmed as these most likely have a direct epitaxial relationship with the GaAs host lattice, and therefore do not appear in grazing incidence measurements (asymmetric scans). Making use of the Scherrer equation, the size L of these nanoclusters can be estimated: $L = K/\beta \cos\theta$, where K is dimensionless shape factor (0.94 for GaAs), λ the X-ray wavelength, β the line broadening at half the maximum intensity (FWHM) and θ is the Bragg angle. For this concentration we estimate an average size of 6.8 nm for the NiAs-type MnAs nanoclusters.

Other types of secondary phases were identified in the 5% Mn sample. Two peaks of *NiAs-type* hexagonal nanoclusters are observed: the $\{10\bar{1}2\}$ peak and the $\{011\bar{1}\}$ peak, indicating the presence of nanoparticles with average sizes 3.2-5.5 nm. The presence of ZB MnAs nanoclusters is also possible, however they are not directly visible in our GIXRD measurements. Another phase was identified: a (110) peak of orthorhombic As (orange circle in figure 4.13). This phase is in accordance with various literature reports [77, 80, 78, 81], in which the hexagonal MnAs nanoclusters are usually accompanied by an As cluster, and sometimes voids.

4.3.4.2 Magnetism

When annealing above the substitutional Mn diffusion temperature the magnetic properties of (Ga,Mn)As change considerably by forming nanoscale superparamagnetic MnAs clusters [39, 73, 111, 113].

We will discuss these magnetic properties in the following sections by analyzing the SQUID magnetometry measurements we performed on our samples.

Low concentration

In figure 4.19 on the next page we show the M-H curves for the (Ga,Mn)As samples annealed at $300°$C and $600°$C. The latter curve is characteristic of a superparamagnetic (SPM) system below the blocking temperature, which is confirmed by the ZFC-FC curves (figure 4.19b).

As seen in the previous section (cf. section 4.3.4.1), in this sample the Mn atoms precipitated into a secondary phase, nanoscale superparamagnetic MnAs clusters. From the ZFC-FC curves in figure 4.19b one can verify that these superparamagnetic nanoclusters have a blocking temperature of $T_b = 17$ K.

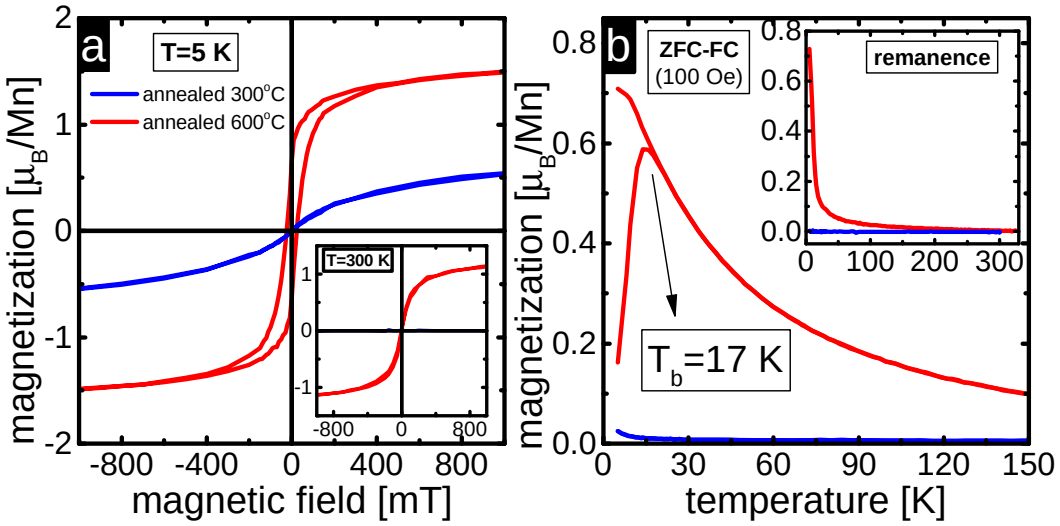

Figure 4.19: (a) Magnetization as a function of applied magnetic field at 5 K and at 300 K (inset); (b) ZFC-FC and remanence (inset) as a function of temperature for $300°$C and $600°$C annealed 1% (Ga,Mn)As.

For the sample annealed at $300°$C we observe a great reduction in magnetization from the sample annealed at $200°$C in the last section. However, some magnetization remains at very low temperature, possibly residual FM from (Ga,Mn)As or FM/SPM in Mn-rich regions.

High concentration

As in the low concentration case the magnetic properties of (Ga,Mn)As annealed at higher than growth temperature are those of a superparamagnetic system.

In figure 4.20 we observe typical M-T and M-H curves for these systems annealed at the highest annealing temperature: ferromagnetic-like hysteresis with small remanence and a ZFC-FC curve with a blocking temperature of $T_b = 25$ K and high T_C. This is in good agreement with the precipitation into nanoscale MnAs clusters as seen before (cf. sections. 4.3.2 and 4.3.4.1).

For the sample annealed at $300°$C the magnetization as a function of applied field curves display some superparamagnetic behavior, indicative of residual FM from (Ga,Mn)As or FM/SPM from the Mn segregation into disordered Mn-rich regions, without formation of nanoclusters with a well-defined structure.

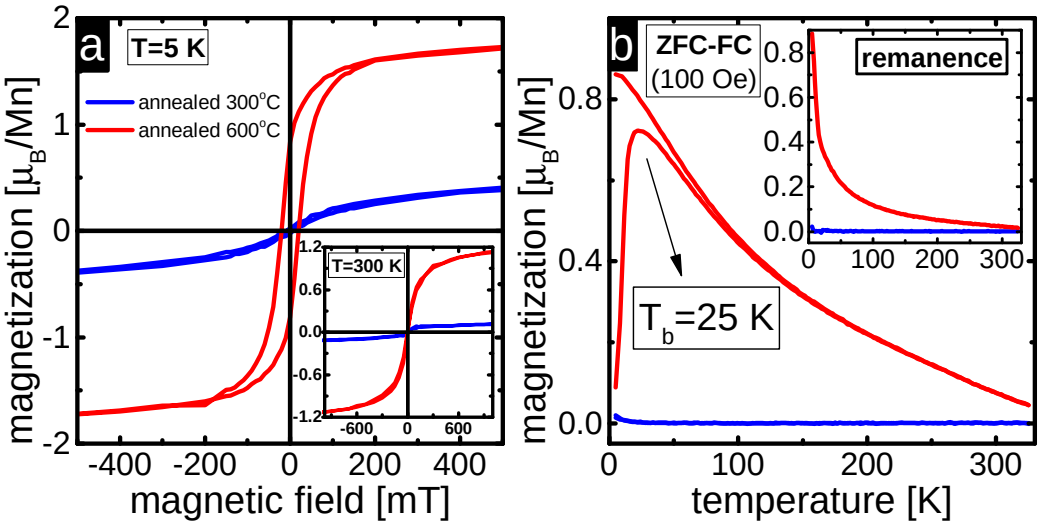

Figure 4.20: (a) Magnetization as a function of applied magnetic field at 5 K and at 300K (inset) ; (b) ZFC-FC curves and remanence (inset) as a function of temperature for 300°C air annealed and 600°C vacuum annealed 5% (Ga,Mn)As.

4.3.4.3 Concentration dependence

In perfect agreement with our structural analysis in section 4.3.4.1 we observe for both concentrations that by annealing at 300°C in air for 100 hours, the ferromagnetism essentially vanishes. Annealing at this temperature, where the Mn_s is mobile, does not allow the existence of ferromagnetic ordering, as seen in figure 4.21. Also, there is little evidence for formation of nanoscale clusters/disordered Mn-rich regions as superparamagnetic hysteresis loops appear for both concentrations (at low temperature), with no remanence for the whole measured temperature range.

Distinctly, both 600°C vacuum annealed samples display typical superparamagnetic behavior, with higher magnetization for the 5% Mn sample with about the same coercivity. These results confirm the presence of nanoclusters as observed in the XRD data (cf. sec. 4.3.4.1). As in various superparamagnetic systems with clusters or nanoparticles, the blocking temperature of the ZFC-FC curves scales with the size of the clusters [114], as magnetization reversal is proportional to the volume of the clusters. Therefore, one can expect the average cluster size for the 5% Mn sample to be bigger than for the 1% Mn sample, as the latter displays a lower T_b. We can also speculate that in the 5% Mn sample the size distribution is larger, i.e. the clusters present a more size variety than in the 1% Mn sample. In fact the type and size of the nanoclusters should have an effect on the layer's magnetic properties. Yokoyama *et al* [76] observed that the net magnetization per

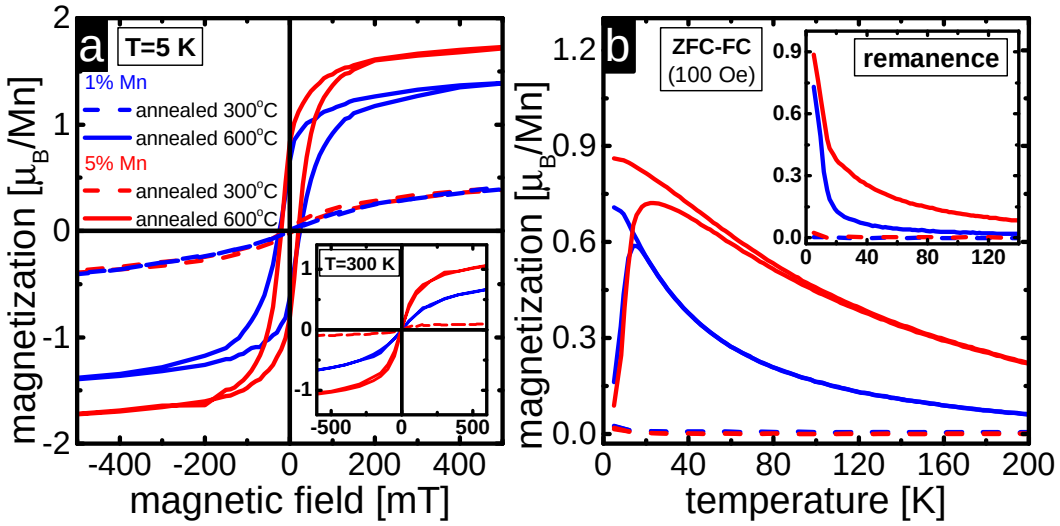

Figure 4.21: Magnetization curves for 1% and 5% (Ga,Mn)As samples annealed respectively at $300°$C and $600°$C.

cubic centimeter as well as the Curie temperature T_C of GaAs:MnAs of the NiAs-type is higher than for the ZB–type. Accordingly, we expect that our samples contain clusters of both types, with a smaller size distribution of mainly ZB nanoclusters for the 1% Mn sample while the 5% Mn sample contains significantly more clusters of NiAs-type. This is in stark contrast with our structural data, where the estimated cluster size for 1% Mn sample is larger than for the 5% Mn. This can be explained by the formation of crystallites, which is in fact what is measured in a GIXRD experiment. In other words, in the 1% Mn sample the MnAs clusters of NiAs–type are several and with an average size larger than the one of clusters in the 5% Mn sample. Combining these conclusions with our SQUID data we can extrapolate that our 5% Mn sample has predominantly nanocluster of the NiAs-type while the 1% Mn sample contains mainly ZB–type clusters.

5 Conclusion

This MSc thesis addressed three key aspects of the *model* DMS (Ga,Mn)As: (1) the identification of Mn interstitial site in ferromagnetic (Ga,Mn)As as well as (2) the thermal stability of the different lattice sites occupied by Mn impurities for different Mn concentrations, and (3) its influence on the material's structure and magnetism.

Regarding the interstitial Mn site (1), we identified unambiguously it as the T_{As} site, both before and after thermal annealing at 200°C. The T_{As} site is therefore the energetically favorable site regardless of the interstitial Mn atom being isolated or forming complexes with substitutional Mn. This information is crucial for the understanding of electric and magnetic self-compensation in (Ga,Mn)As, as well as the mechanisms of electric and magnetic activation by thermally induced out-diffusion of interstitial Mn.

Regarding the thermal stability of Mn impurities in (Ga,Mn)As (2), our results show that compared to the substitutional Mn, interstitial Mn becomes mobile at lower temperatures, for both low (1%) and high (5%) Mn concentration. Moreover, the diffusion temperatures are lower for the high concentration than for the low concentration case. Accordingly, the activation energy for substitutional and interstitial Mn decreases with increasing Mn concentration. For the substitutional we obtained an activation energy of 2.3-2.6 eV for 1% Mn and 1.9-2.0 eV for 5% Mn, and for the interstitial, 1.5-2.1 eV for 1% Mn and 1.3-1.8 eV for 5%. These values reflect the complex diffusion mechanisms that interplay in (Ga,Mn)As. For substitutional diffusion, the decrease of activation energy is associated with a decrease of the binding energy of impurities to the substitutional site, i.e. increasing impurity concentration leads to a decrease in distance between Mn_s, which enhances the vacancy-assisted diffusion of the substitutional Mn. For the interstitial, the decrease relates to charge screening effects, i.e. increasing impurity concentration, increases the metallicity of the material and decreases the Coulomb interactions between the diffusing interstitials and the host atoms. Consequently the charge of the diffusing species is screened, requiring less energy to overcome the migration barriers between interstitial sites. These results can be translated into two relevant findings: (i) at typical growth temperatures (200-300°C) interstitial Mn is mobile for high Mn concentration (5%) but not for low concentration (1%); and

(ii) substitutional Mn impurities become mobile at lower temperatures than those previously reported. Finding (i) sheds new light on the formation mechanism of interstitial Mn during LT-MBE growth. It shows that interstitial Mn only forms for Mn concentrations at which it is mobile during growth. As such, this finding constitutes strong experimental evidence for a previously proposed (but never demonstrated) mechanism in which interstitial Mn is not incorporated simultaneously with substitutional Mn but by diffusion of Mn atoms from the sample surface into the bulk of the film (which can only occur if the interstitial is mobile in the film bulk at the growth temperature). Finding (ii) uncovers an unexpectedly low temperature regime in which the Mn impurities become mobile at high impurity concentrations, i.e. annealing at temperatures as low as 200-250°C induces Mn diffusion and segregation.

In (3) we conducted a comprehensive study of the interplay between local structure and magnetism in the different annealing regimes considered in (2). Annealing at $\sim 200^{\circ}$C resulted in the reduction of interstitial Mn fraction only for the high Mn concentration, leading to an increase in T_C and magnetization, while for the low concentration no improvement in ferromagnetic behavior is observed, further supporting the scenario in which the interstitial Mn does not form during LT-MBE growth for Mn concentrations below 2%. Complementing result (ii) in (2), annealing at $\sim 300^{\circ}$C induced precipitation of Mn into disordered Mn-rich regions for both concentration regimes, effectively annihilating the ferromagnetism. Additionally, annealing at a temperature of 600°C led to the formation of a well defined secondary-phases, consisting of superparamagnetic MnAs nanoclusters of mainly two-types: zincblende, coherent to the GaAs matrix, and hexagonal NiAs-type, strained and not coherent with host matrix.

This comprehensive study revealed itself as a powerful complement to the emission channeling technique in order to explore and investigate the structural and magnetic properties of (Ga,Mn)As. This *toolset* of characterization techniques presents itself as a dynamic and thorough investigation method for studying dilute magnetic systems, such as the case of dilute magnetic semiconductors and oxides.

Outlook

The main implications of the results presented in this thesis concern the influence of the local structure on ferromagnetic (Ga,Mn)As. For low impurity concentrations the impurities are essentially substitutional, with high thermal stability allowing for a full activation of the magnetic moments. Increasing concentration lowers the mobility threshold, increasing diffusion, leading to the formation of interstitials upon growth, which compensate substitutional

Mn both magnetically and electrically. Passivating the interstitial Mn by annealing at low temperatures increases the magnetization and Curie temperature. However, with increasing concentration, the temperature gap interstitial removal and Mn segregation narrows down significantly, requiring a careful design of the activation annealing procedure (temperature and duration).

This increased understanding of the complex interplay between local structure and ferromagnetism in (Ga,Mn)As has the potential to inspire new strategies to increase the substitutional Mn concentration and consequently the Curie temperature of this model DMS system. Such strategies may include development of improved sample preparation methods and/or post-growth treatment for more efficient incorporation of Mn in substitutional sites as well as minimization of interstitial Mn. Also, the intricate physics uncovered on this specific system motivates a wider investigation of the III-Mn-V DMS family, where one can evaluate e.g. the effect of the III-V band-gap, the position of the Mn acceptor level and the degree of hole localization. Unraveling the interplaying mechanisms between the structural and magnetic properties of these DMS materials constitutes an important step in the understanding of the fundamental physics that lie behind them and the technological applications that lie beyond.

> *"It might be, therefore, expected that studies of magnetically doped semiconductors (...) will continue to bring unanticipated and inspiring discoveries in the years to come."*
>
> Tomasz Dietl and Hideo Ohno, 2014 [39]

Publications

Articles submitted or to be submitted to international, peer-reviewed journals

- "Unambiguous identification of the interstitial Mn site in ferromagnetic (Ga,Mn)As"
  L.M.C. Pereira, T. Lima, U. Wahl, V. Augustyns, J.G. Correia, K.W. Edmonds, B.L. Gallagher, R.P. Campion, J.P. Araújo, K. Temst, A. Vantomme
  Submitted to *Applied Physics Letters*

- "Concentration-dependent thermal stability of Mn impurities in (Ga,Mn)As"
  T. Lima,U. Wahl, V. Augustyns, J.G. Correia, K.W. Edmonds, B.L. Gallagher, R.P. Campion, J.P. Araújo, K. Temst, A. Vantomme, L.M.C. Pereira
  To be submitted to *Physical Review B*

- "Concentration and temperature dependent Mn segregation in (Ga,Mn)As"
  T. Lima, V. Augustyns, K.W. Edmonds, B.L. Gallagher, R.P. Campion, D. Banerjee, C. Baehtz, M.J. Van Bael, J.P. Araújo, K. Temst, A. Vantomme, L.M.C. Pereira
  To be submitted to *Journal of Applied Physics*

Communications in international, peer-reviewed conferences

- "Lattice location and thermal stability of Mn in ferromagnetic (Ga,Mn)As"
  L.M.C. Pereira, T. Lima, U. Wahl, V. Augustyns, J.G. Correia, K.W. Edmonds, B.L. Gallagher, R.P. Campion, K. Temst, A. Vantomme
  Poster presented at the *INTERMAG 2014 - IEEE International Magnetics Conference*, 4-8 May 2014, Dresden, Germany

Bibliography

[1] D. D. Awschalom, L. C. Bassett, A. S. Dzurak, E. L. Hu, and J. R. Petta, "Quantum spintronics: engineering and manipulating atom-like spins in semiconductors," *Science (New York, N.Y.)*, vol. 339, pp. 1174–9, Mar. 2013.

[2] S. D. Bader and S. S. P. Parkin, "Spintronics," in *Annual Review of Condensed Matter Physics, vol 1* (J. Langer, ed.), pp. 71–88, Annual Reviews, 2010.

[3] H. Ohno, "Making Nonmagnetic Semiconductors Ferromagnetic," *Science*, vol. 281, pp. 951–956, Aug. 1998.

[4] D. D. Awschalom and M. E. Flatté, "Challenges for semiconductor spintronics," *Nature Physics*, vol. 3, pp. 153–159, Mar. 2007.

[5] J. K. Furdyna, "Diluted magnetic semiconductors," *Journal of Applied Physics*, vol. 64, no. 4, p. R29, 1988.

[6] H. Ohno, H. Munekata, T. Penney, S. von Molnár, and L. Chang, "Magnetotransport properties of p-type (In,Mn)As diluted magnetic III-V semiconductors," *Physical Review Letters*, vol. 68, pp. 2664–2667, Apr. 1992.

[7] H. Ohno, A. Shen, F. Matsukura, A. Oiwa, A. Endo, S. Katsumoto, and Y. Iye, "(Ga,Mn)As: A new diluted magnetic semiconductor based on GaAs," *Applied Physics Letters*, vol. 69, no. 3, p. 363, 1996.

[8] S. Ghosh and P. Bhattacharya, "Surface-emitting spin-polarized $In_{0.4}Ga_{0.6}As$/GaAs quantum-dot light-emitting diode," *Applied Physics Letters*, vol. 80, no. 4, p. 658, 2002.

[9] D. Chiba, F. Matsukura, and H. Ohno, "Electric-field control of ferromagnetism in (Ga,Mn)As," *Applied Physics Letters*, vol. 89, no. 16, p. 162505, 2006.

[10] K. C. Hall, J. P. Zahn, A. Gamouras, S. March, J. L. Robb, X. Liu, and J. K. Furdyna, "Ultrafast optical control of coercivity in GaMnAs," *Applied Physics Letters*, vol. 93, no. 3, p. 032504, 2008.

[11] M. Wang, R. P. Campion, A. W. Rushforth, K. W. Edmonds, C. T. Foxon, and B. L. Gallagher, "Achieving high Curie temperature in (Ga,Mn)As," *Applied Physics Letters*, vol. 93, no. 13, p. 132103, 2008.

[12] V. Novák, K. Olejník, J. Wunderlich, M. Cukr, K. Výborný, A. W. Rushforth, K. W. Edmonds, R. P. Campion, B. L. Gallagher, J. Sinova, and T. Jungwirth, "Curie Point Singularity in the Temperature Derivative of Resistivity in (Ga,Mn)As," *Physical Review Letters*, vol. 101, p. 077201, Aug. 2008.

[13] K. Olejník, M. Owen, V. Novák, J. Mašek, A. Irvine, J. Wunderlich, and T. Jungwirth, "Enhanced annealing, high Curie temperature, and low-voltage gating in (Ga,Mn)As: A surface oxide control study," *Physical Review B*, vol. 78, p. 054403, Aug. 2008.

[14] M. Wang, K. Edmonds, B. Gallagher, A. Rushforth, O. Makarovsky, A. Patanè, R. Campion, C. Foxon, V. Novak, and T. Jungwirth, "High Curie temperatures at low compensation in the ferromagnetic semiconductor (Ga,Mn)As," *Physical Review B*, vol. 87, p. 121301, Mar. 2013.

[15] T. Schallenberg and H. Munekata, "Preparation of ferromagnetic (In,Mn)As with a high Curie temperature of 90K," *Applied Physics Letters*, vol. 89, no. 4, p. 042507, 2006.

[16] T. Dietl, "Origin and control of ferromagnetism in dilute magnetic semiconductors and oxides (invited)," *Journal of Applied Physics*, vol. 103, no. 7, p. 07D111, 2008.

[17] T. Jungwirth, K. Wang, J. Mašek, K. Edmonds, J. König, J. Sinova, M. Polini, N. Goncharuk, A. MacDonald, M. Sawicki, A. Rushforth, R. Campion, L. Zhao, C. Foxon, and B. Gallagher, "Prospects for high temperature ferromagnetism in (Ga,Mn)As semiconductors," *Physical Review B*, vol. 72, p. 165204, Oct. 2005.

[18] T. Dietl, "Zener Model Description of Ferromagnetism in Zinc-Blende Magnetic Semiconductors," *Science*, vol. 287, pp. 1019–1022, Feb. 2000.

[19] Y. Matsumoto, "Room-Temperature Ferromagnetism in Transparent Transition Metal-Doped Titanium Dioxide," *Science*, vol. 291, pp. 854–856, Jan. 2001.

[20] K. Sato and H. Katayama-Yoshida, "Ferromagnetism in a transition metal atom doped ZnO," *Physica E: Low-dimensional Systems and Nanostructures*, vol. 10, pp. 251–255, May 2001.

[21] C. Liu, F. Yun, and H. Morkoç, "Ferromagnetism of ZnO and GaN: A Review," *Journal of Materials Science: Materials in Electronics*, vol. 16, pp. 555–597, Sept. 2005.

[22] S. J. Pearton, W. H. Heo, M. Ivill, D. P. Norton, and T. Steiner, "Dilute magnetic semiconducting oxides," *Semiconductor Science and Technology*, vol. 19, pp. R59–R74, Oct. 2004.

[23] S. Pearton, C. Abernathy, D. Norton, A. Hebard, Y. Park, L. Boatner, and J. Budai, "Advances in wide bandgap materials for semiconductor spintronics," *Materials Science and Engineering: R: Reports*, vol. 40, pp. 137–168, Feb. 2003.

[24] K. Sato, L. Bergqvist, J. Kudrnovský, P. H. Dederichs, O. Eriksson, I. Turek, B. Sanyal, G. Bouzerar, H. Katayama-Yoshida, V. A. Dinh, T. Fukushima, H. Kizaki, and R. Zeller, "First-principles theory of dilute magnetic semiconductors," *Reviews of Modern Physics*, vol. 82, pp. 1633–1690, May 2010.

[25] A. Ney, T. Kammermeier, V. Ney, K. Ollefs, and S. Ye, "Limitations of measuring small magnetic signals of samples deposited on a diamagnetic substrate," *Journal of Magnetism and Magnetic Materials*, vol. 320, pp. 3341–3346, Dec. 2008.

[26] M. A. Garcia, E. Fernandez Pinel, J. de la Venta, A. Quesada, V. Bouzas, J. F. Fernandez, J. J. Romero, M. S. Martin Gonzalez, and J. L. Costa-Kramer, "Sources of experimental errors in the observation of nanoscale magnetism," *Journal of Applied Physics*, vol. 105, no. 1, p. 013925, 2009.

[27] S. Zhou, K. Potzger, G. Talut, H. Reuther, J. von Borany, R. Grotzschel, W. Skorupa, M. Helm, J. Fassbender, N. Volbers, M. Lorenz, and T. Herrmannsdorfer, "Fe-implanted ZnO: Magnetic precipitates versus dilution," *Journal of Applied Physics*, vol. 103, no. 2, p. 023902, 2008.

[28] A. Bonanni, A. Navarro-Quezada, T. Li, M. Wegscheider, Z. Matěj, V. Holý, R. Lechner, G. Bauer, M. Rovezzi, F. D'Acapito, M. Kiecana, M. Sawicki, and T. Dietl, "Controlled Aggregation of Magnetic Ions in a Semiconductor: An Experimental Demonstration," *Physical Review Letters*, vol. 101, p. 135502, Sept. 2008.

[29] W. Stefanowicz, D. Sztenkiel, B. Faina, A. Grois, M. Rovezzi, T. Devillers, F. D'Acapito, A. Navarro-Quezada, T. Li, R. Jakieła, M. Sawicki, T. Dietl, and A. Bonanni, "Structural and paramagnetic properties of dilute $Ga_{1-x}Mn_xN$," *Physical Review B*, vol. 81, p. 235210, June 2010.

[30] A. Ney, T. Kammermeier, K. Ollefs, S. Ye, V. Ney, T. C. Kaspar, S. A. Chambers, F. Wilhelm, and a. Rogalev, "Anisotropic paramagnetism of Co-doped ZnO epitaxial films," *Physical Review B*, vol. 81, p. 054420, Feb. 2010.

[31] S. Granville, B. J. Ruck, F. Budde, H. J. Trodahl, and G. V. M. Williams, "Nearest-neighbor Mn antiferromagnetic exchange in $Ga_{1-x}Mn_xN$," *Physical Review B*, vol. 81, p. 184425, May 2010.

[32] A. Ney, K. Ollefs, S. Ye, T. Kammermeier, V. Ney, T. Kaspar, S. Chambers, F. Wilhelm, and a. Rogalev, "Absence of Intrinsic Ferromagnetic Interactions of Isolated and Paired Co Dopant Atoms in $Zn_{1-x}Co_xO$ with High Structural Perfection," *Physical Review Letters*, vol. 100, p. 157201, Apr. 2008.

[33] P. Sati, C. Deparis, C. Morhain, S. Schäfer, and a. Stepanov, "Antiferromagnetic Interactions in Single Crystalline $Zn_{1-x}Co_xO$ Thin Films," *Physical Review Letters*, vol. 98, p. 137204, Mar. 2007.

[34] Q. Xu, S. Zhou, D. Markó, K. Potzger, J. Fassbender, M. Vinnichenko, M. Helm, H. Hochmuth, M. Lorenz, M. Grundmann, and H. Schmidt, "Paramagnetism in Co-doped ZnO films," *Journal of Physics D: Applied Physics*, vol. 42, p. 085001, Apr. 2009.

[35] E. Sarigiannidou, F. Wilhelm, E. Monroy, R. Galera, E. Bellet-Amalric, A. Rogalev, J. Goulon, J. Cibert, and H. Mariette, "Intrinsic ferromagnetism in wurtzite (Ga,Mn)N semiconductor," *Physical Review B*, vol. 74, p. 041306, July 2006.

[36] K. Zhao, Z. Deng, X. C. Wang, W. Han, J. L. Zhu, X. Li, Q. Q. Liu, R. C. Yu, T. Goko, B. Frandsen, L. Liu, F. Ning, Y. J. Uemura, H. Dabkowska, G. M. Luke, H. Luetkens, E. Morenzoni, S. R. Dunsiger, A. Senyshyn, P. Böni, and C. Q. Jin, "New diluted ferromagnetic semiconductor with Curie temperature up to 180 K and isostructural to the '122' iron-based superconductors.," *Nature communications*, vol. 4, p. 1442, Jan. 2013.

[37] T. Jungwirth, V. Novák, X. Martí, M. Cukr, F. Máca, A. B. Shick, J. Mašek, P. Horodyská, P. Němec, V. Holý, J. Zemek, P. Kužel, I. Němec, B. L. Gallagher, R. P. Campion, C. T. Foxon, and J. Wunderlich, "Demonstration of molecular beam epitaxy and a semiconducting band structure for I-Mn-V compounds," *Physical Review B*, vol. 83, p. 035321, Jan. 2011.

[38] J. G. Checkelsky, J. Ye, Y. Onose, Y. Iwasa, and Y. Tokura, "Dirac-fermion-mediated ferromagnetism in a topological insulator," *Nature Physics*, vol. 8, pp. 729–733, Aug. 2012.

[39] T. Dietl and H. Ohno, "Dilute ferromagnetic semiconductors: Physics and spintronic structures," *Reviews of Modern Physics*, vol. 86, pp. 187–251, Mar. 2014.

[40] "More than just room temperature.," *Nature materials*, vol. 9, p. 951, Dec. 2010.

[41] T. Dietl, "A ten-year perspective on dilute magnetic semiconductors and oxides.," *Nature materials*, vol. 9, pp. 965–74, Dec. 2010.

[42] M. Dobrowolska, K. Tivakornsasithorn, X. Liu, J. K. Furdyna, M. Berciu, K. M. Yu, and W. Walukiewicz, "Controlling the Curie temperature in (Ga,Mn)As through location of the Fermi level within the impurity band.," *Nature materials*, vol. 11, pp. 444–9, May 2012.

[43] J. Blinowski and P. Kacman, "Spin interactions of interstitial Mn ions in ferromagnetic GaMnAs," *Physical Review B*, vol. 67, p. 121204, Mar. 2003.

[44] K. Edmonds, P. Bogusławski, K. Wang, R. Campion, S. Novikov, N. Farley, B. Gallagher, C. Foxon, M. Sawicki, T. Dietl, M. Buongiorno Nardelli, and J. Bernholc, "Mn Interstitial Diffusion in (Ga,Mn)As," *Physical Review Letters*, vol. 92, p. 037201, Jan. 2004.

[45] J. Mašek and F. Máca, "Interstitial Mn in (Ga,Mn)As: Binding energy and exchange coupling," *Physical Review B*, vol. 69, p. 165212, Apr. 2004.

[46] F. Glas, G. Patriarche, L. Largeau, and a. Lemaître, "Determination of the Local Concentrations of Mn Interstitials and Antisite Defects in GaMnAs," *Physical Review Letters*, vol. 93, p. 086107, Aug. 2004.

[47] R. Myers, B. Sheu, A. Jackson, A. Gossard, P. Schiffer, N. Samarth, and D. Awschalom, "Antisite effect on hole-mediated ferromagnetism in (Ga,Mn)As," *Physical Review B*, vol. 74, p. 155203, Oct. 2006.

[48] D. E. Bliss, W. Walukiewicz, J. W. Ager, E. E. Haller, K. T. Chan, and S. Tanigawa, "Annealing studies of low-temperature-grown GaAs:Be," *Journal of Applied Physics*, vol. 71, no. 4, p. 1699, 1992.

[49] S. Erwin and A. Petukhov, "Self-Compensation in Manganese-Doped Ferromagnetic Semiconductors," *Physical Review Letters*, vol. 89, p. 227201, Nov. 2002.

[50] N. Samarth, "Ferromagnetic semicondutors: Battle of the bands.," *Nature materials*, vol. 11, pp. 360–1, May 2012.

[51] C. Zener, "Interaction between the d-Shells in the Transition Metals. II. Ferromagnetic Compounds of Manganese with Perovskite Structure," *Physical Review*, vol. 82, pp. 403–405, May 1951.

[52] T. Dietl, A. Haury, and Y. Merle d'Aubigné, "Free carrier-induced ferromagnetism in structures of diluted magnetic semiconductors," *Physical Review B*, vol. 55, pp. R3347–R3350, Feb. 1997.

[53] I. Vurgaftman, J. R. Meyer, and L. R. Ram-Mohan, "Band parameters for III–V compound semiconductors and their alloys," *Journal of Applied Physics*, vol. 89, no. 11, p. 5815, 2001.

[54] X. Liu, Y. Sasaki, and J. Furdyna, "Ferromagnetic resonance in $Ga_{1-x}Mn_xAs$: Effects of magnetic anisotropy," *Physical Review B*, vol. 67, p. 205204, May 2003.

[55] U. Welp, V. K. Vlasko-Vlasov, A. Menzel, H. D. You, X. Liu, J. K. Furdyna, and T. Wojtowicz, "Uniaxial in-plane magnetic anisotropy of $Ga_{1-x}Mn_xAs$," *Applied Physics Letters*, vol. 85, no. 2, p. 260, 2004.

[56] K. Wang, K. Edmonds, R. Campion, L. Zhao, C. Foxon, and B. Gallagher, "Anisotropic magnetoresistance and magnetic anisotropy in high-quality (Ga,Mn)As films," *Physical Review B*, vol. 72, p. 085201, Aug. 2005.

[57] S. Mack, R. C. Myers, J. T. Heron, A. C. Gossard, and D. D. Awschalom, "Stoichiometric growth of high Curie temperature heavily alloyed GaMnAs," *Applied Physics Letters*, vol. 92, no. 19, p. 192502, 2008.

[58] T. Hayashi, Y. Hashimoto, S. Katsumoto, and Y. Iye, "Effect of low-temperature annealing on transport and magnetism of diluted magnetic semiconductor (Ga, Mn)As," *Applied Physics Letters*, vol. 78, no. 12, p. 1691, 2001.

[59] K. M. Yu, W. Walukiewicz, T. Wojtowicz, J. Denlinger, M. A. Scarpulla, X. Liu, and J. K. Furdyna, "Effect of film thickness on the incorporation of Mn interstitials in $Ga_{1-x}Mn_xAs$," *Applied Physics Letters*, vol. 86, no. 4, p. 042102, 2005.

[60] M. Adell, J. Adell, L. Ilver, J. Kanski, J. Sadowski, and J. Domagala, "Mn enriched surface of annealed (GaMn)As layers annealed under arsenic capping," *Physical Review B*, vol. 75, p. 054415, Feb. 2007.

[61] R. Shioda and K. Ando, "Local structures of III-V diluted magnetic semiconductors $Ga_{1-x}Mn_xAs$ studied using extended x-ray-absorption fine structure," *Physical Review B*, vol. 58, no. 3, pp. 1100–1102, 1998.

[62] K. Yu, W. Walukiewicz, T. Wojtowicz, I. Kuryliszyn, X. Liu, Y. Sasaki, and J. Furdyna, "Effect of the location of Mn sites in ferromagnetic $Ga_{1-x}Mn_xAs$ on its Curie temperature," *Physical Review B*, vol. 65, p. 201303, Apr. 2002.

[63] R. Bacewicz, A. Twaróg, A. Malinowska, T. Wojtowicz, X. Liu, and J. Furdyna, "Local structure of Mn in (Ga,Mn)As probed by X-ray absorption spectroscopy," *Journal of Physics and Chemistry of Solids*, vol. 66, pp. 2004–2007, Nov. 2005.

[64] L. M. C. Pereira, U. Wahl, S. Decoster, J. G. Correia, M. R. da Silva, A. Vantomme, and J. P. Araujo, "Direct identification of interstitial Mn in heavily p-type doped GaAs and evidence of its high thermal stability," *Applied Physics Letters*, vol. 98, no. 20, p. 201905, 2011.

[65] L. M. C. Pereira, U. Wahl, S. Decoster, J. G. Correia, L. M. Amorim, M. R. da Silva, J. P. Araújo, and A. Vantomme, "Stability and diffusion of interstitial and substitutional Mn in GaAs of different doping types," *Physical Review B*, vol. 86, p. 125206, Sept. 2012.

[66] K. Lawniczak-Jablonska, J. Libera, A. Wolska, M. Klepka, R. Jakiela, and J. Sadowski, "The ratio of interstitial to substitutional site occupation by Mn atoms in GaAs estimated by EXAFS," *Radiation Physics and Chemistry*, vol. 78, pp. S80–S85, Oct. 2009.

[67] A. Wolska, K. Lawniczak-Jablonska, M. Klepka, R. Jakiela, J. Sadowski, I. Demchenko, E. Holub-Krappe, A. Persson, and D. Arvanitis, "XANES studies of Mn K and L-3, L-2 edges in the (Ga, Mn) As layers modified by high temperature annealing," *Acta Physica Polonica. A*, vol. 114, no. 2, pp. 357–366, 2008.

[68] V. Holy, X. Marti, L. Horak, O. Caha, V. Novak, M. Cukr, and T. U. Schulli, "Density of Mn interstitials in (Ga,Mn)As epitaxial layers determined by anomalous x-ray diffraction," *Applied Physics Letters*, vol. 97, no. 18, p. 181913, 2010.

[69] L. Horák, Z. Sobáň, and V. Holý, "Study of Mn interstitials in (Ga, Mn)As using high-resolution x-ray diffraction.," *Journal of physics. Condensed matter : an Institute of Physics journal*, vol. 22, p. 296009, July 2010.

[70] T. L. Lee, C. Bihler, W. Schoch, W. Limmer, J. Daeubler, S. Thieß, M. S. Brandt, and J. Zegenhagen, "Fourier transform imaging of impurities in the unit cells of crystals: Mn in GaAs," *Physical Review B*, vol. 81, p. 235207, June 2010.

[71] V. Baykov, P. Korzhavyi, and B. Johansson, "Diffusion of Interstitial Mn in the Dilute Magnetic Semiconductor (Ga,Mn)As: The Effect of a Charge State," *Physical Review Letters*, vol. 101, p. 177204, Oct. 2008.

[72] H. Raebiger, M. Ganchenkova, and J. von Boehm, "Diffusion and clustering of substitutional Mn in (Ga,Mn)As," *Applied Physics Letters*, vol. 89, no. 1, p. 012505, 2006.

[73] J. De Boeck, R. Oesterholt, A. Van Esch, H. Bender, C. Bruynseraede, C. Van Hoof, and G. Borghs, "Nanometer-scale magnetic MnAs particles in GaAs grown by molecular beam epitaxy," *Applied Physics Letters*, vol. 68, no. 19, p. 2744, 1996.

[74] M. Moreno, A. Trampert, B. Jenichen, L. Daweritz, and K. H. Ploog, "Correlation of structure and magnetism in GaAs with embedded Mn(Ga)As magnetic nanoclusters," *Journal of Applied Physics*, vol. 92, no. 8, p. 4672, 2002.

[75] M. Moreno, V. Kaganer, B. Jenichen, A. Trampert, L. Däweritz, and K. Ploog, "Micromechanics of MnAs nanocrystals embedded in GaAs," *Physical Review B*, vol. 72, p. 115206, Sept. 2005.

[76] M. Yokoyama, H. Yamaguchi, T. Ogawa, and M. Tanaka, "Zinc-blende-type MnAs nanoclusters embedded in GaAs," *Journal of Applied Physics*, vol. 97, no. 10, p. 10D317, 2005.

[77] A. Kwiatkowski, D. Wasik, M. Kaminska, R. Bozek, J. Szczytko, A. Twardowski, J. Borysiuk, J. Sadowski, and J. Gosk, "Structure and magnetism of MnAs nanocrystals embedded in GaAs as a function of post-growth annealing temperature," *Journal of Applied Physics*, vol. 101, no. 11, p. 113912, 2007.

[78] J. Sadowski, J. Z. Domagala, R. Mathieu, A. Kovács, T. Kasama, R. E. Dunin-Borkowski, and T. Dietl, "Formation process and superparamagnetic properties of (Mn,Ga)As nanocrystals in GaAs fabricated by annealing of (Ga,Mn)As layers with low Mn content," *Physical Review B*, vol. 84, p. 245306, Dec. 2011.

[79] K. Lawniczak-Jablonska, J. Libera, A. Wolska, M. T. Klepka, P. Dluzewski, J. Sadowski, D. Wasik, A. Twardowski, A. Kwiatkowski, and K. Sato, "The source of room temperature ferromagnetism in granular GaMnAs layers with zinc blende clusters," *physica status solidi (RRL) - Rapid Research Letters*, vol. 5, pp. 62–64, Feb. 2011.

[80] A. Kovacs, J. Sadowski, T. Kasama, J. Domagała, R. Mathieu, T. Dietl, and R. E. Dunin-Borkowski, "Voids and Mn-rich inclusions in a (Ga,Mn)As ferromagnetic semiconductor investigated by transmission electron microscopy," *Journal of Applied Physics*, vol. 109, no. 8, p. 083546, 2011.

[81] a. Kovács, J. Sadowski, T. Kasama, M. Duchamp, and R. E. Dunin-Borkowski, "Effect of post-growth annealing on secondary phase formation in low-temperature-grown

Mn-doped GaAs," *Journal of Physics D: Applied Physics*, vol. 46, p. 145309, Apr. 2013.

[82] M. Sawicki, K. Wang, K. Edmonds, R. Campion, A. Rushforth, C. Foxon, B. Gallagher, and T. Dietl, "Coercivity enlargement in (Ga,Mn)As thin films with small amount of MnAs nanoclusters," *Journal of Magnetism and Magnetic Materials*, vol. 310, pp. 2126–2128, Mar. 2007.

[83] R. Campion, K. Edmonds, L. Zhao, K. Wang, C. Foxon, B. Gallagher, and C. Staddon, "The growth of GaMnAs films by molecular beam epitaxy using arsenic dimers," *Journal of Crystal Growth*, vol. 251, pp. 311–316, Apr. 2003.

[84] A. MacDonald, P. Schiffer, and N. Samarth, "Ferromagnetic semiconductors: moving beyond (Ga, Mn) As," *Nature Materials*, pp. 195–202, 2005.

[85] W. Matz, N. Schell, G. Bernhard, F. Prokert, T. Reich, J. Clauß ner, W. Oehme, R. Schlenk, S. Dienel, H. Funke, F. Eichhorn, M. Betzl, D. Pröhl, U. Strauch, G. Hüttig, H. Krug, W. Neumann, V. Brendler, P. Reichel, M. A. Denecke, and H. Nitsche, "ROBL – a CRG beamline for radiochemistry and materials research at the ESRF," *Journal of Synchrotron Radiation*, vol. 6, pp. 1076–1085, Nov. 1999.

[86] J. Lindhard, "Influence of Crystal Lattice on Motion of Energetic Charged Particles," *Matematisk-fysiske meddelelser udgivet af det Kongelige Danske videnskabernes selskab*, vol. 34, p. 14, 1965.

[87] H. Hofsäss and G. Lindner, "Emission channeling and blocking," *Physics Reports*, vol. 201, no. 3, pp. 121–183, 1991.

[88] M. R. Silva, U. Wahl, J. G. Correia, L. M. Amorim, and L. M. C. Pereira, "A versatile apparatus for on-line emission channeling experiments.," *The Review of scientific instruments*, vol. 84, p. 073506, July 2013.

[89] J. Correia, "Radioactive ion beams and techniques for solid state research," *Nuclear Instruments and Methods in Physics Research Section B: Beam Interactions with Materials and Atoms*, vol. 136-138, pp. 736–743, Mar. 1998.

[90] H. Hofsäss, U. Wahl, and S. G. Jahn, "Impurity lattice location and recovery of structural defects in semiconductors studied by emission channeling," *Hyperfine Interactions*, vol. 84, pp. 27–41, Dec. 1994.

[91] H. Hofsäss, "Emission channeling," *Hyperfine Interactions*, vol. 97-98, pp. 247–283, Dec. 1996.

[92] U. Wahl, "Advances in electron emission channeling measurements in semiconductors," *Hyperfine Interactions*, vol. 129, pp. 349–370, 2000.

[93] U. Wahl. Phd. thesis, Universitat Konstanz, 1992.

[94] B. De Vries. Phd. thesis, Katholieke Universiteit Leuven, 2006.

[95] S. Agostinelli, J. Allison, K. Amako, J. Apostolakis, H. Araujo, P. Arce, M. Asai, D. Axen, S. Banerjee, G. Barrand, F. Behner, L. Bellagamba, J. Boudreau, L. Broglia, A. Brunengo, H. Burkhardt, S. Chauvie, J. Chuma, R. Chytracek, G. Cooperman, G. Cosmo, P. Degtyarenko, A. Dell'Acqua, G. Depaola, D. Dietrich, R. Enami, A. Feliciello, C. Ferguson, H. Fesefeldt, G. Folger, F. Foppiano, A. Forti, S. Garelli, S. Giani, R. Giannitrapani, D. Gibin, J. Gómez Cadenas, I. González, G. Gracia Abril, G. Greeniaus, W. Greiner, V. Grichine, A. Grossheim, S. Guatelli, P. Gumplinger, R. Hamatsu, K. Hashimoto, H. Hasui, A. Heikkinen, A. Howard, V. Ivanchenko, A. Johnson, F. Jones, J. Kallenbach, N. Kanaya, M. Kawabata, Y. Kawabata, M. Kawaguti, S. Kelner, P. Kent, A. Kimura, T. Kodama, R. Kokoulin, M. Kossov, H. Kurashige, E. Lamanna, T. Lampén, V. Lara, V. Lefebure, F. Lei, M. Liendl, W. Lockman, F. Longo, S. Magni, M. Maire, E. Medernach, K. Minamimoto, P. Mora de Freitas, Y. Morita, K. Murakami, M. Nagamatu, R. Nartallo, P. Nieminen, T. Nishimura, K. Ohtsubo, M. Okamura, S. O'Neale, Y. Oohata, K. Paech, J. Perl, A. Pfeiffer, M. Pia, F. Ranjard, A. Rybin, S. Sadilov, E. Di Salvo, G. Santin, T. Sasaki, N. Savvas, Y. Sawada, S. Scherer, S. Sei, V. Sirotenko, D. Smith, N. Starkov, H. Stoecker, J. Sulkimo, M. Takahata, S. Tanaka, E. Tcherniaev, E. Safai Tehrani, M. Tropeano, P. Truscott, H. Uno, L. Urban, P. Urban, M. Verderi, A. Walkden, W. Wander, H. Weber, J. Wellisch, T. Wenaus, D. Williams, D. Wright, T. Yamada, H. Yoshida, and D. Zschiesche, "Geant4—a simulation toolkit," *Nuclear Instruments and Methods in Physics Research Section A: Accelerators, Spectrometers, Detectors and Associated Equipment*, vol. 506, pp. 250–303, July 2003.

[96] J. Allison, K. Amako, J. Apostolakis, H. Araujo, P. Arce Dubois, M. Asai, G. Barrand, R. Capra, S. Chauvie, R. Chytracek, G. Cirrone, G. Cooperman, G. Cosmo, G. Cuttone, G. Daquino, M. Donszelmann, M. Dressel, G. Folger, F. Foppiano, J. Generowicz, V. Grichine, S. Guatelli, P. Gumplinger, A. Heikkinen, I. Hrivnacova, A. Howard, S. Incerti, V. Ivanchenko, T. Johnson, F. Jones, T. Koi, R. Kokoulin, M. Kossov, H. Kurashige, V. Lara, S. Larsson, F. Lei, O. Link, F. Longo, M. Maire, A. Mantero, B. Mascialino, I. McLaren, P. Mendez Lorenzo, K. Minamimoto, K. Murakami, P. Nieminen, L. Pandola, S. Parlati, L. Peralta, J. Perl, A. Pfeiffer, M. Pia, A. Ribon, P. Rodrigues, G. Russo, S. Sadilov, G. Santin, T. Sasaki, D. Smith,

N. Starkov, S. Tanaka, E. Tcherniaev, B. Tome, A. Trindade, P. Truscott, L. Urban, M. Verderi, A. Walkden, J. Wellisch, D. Williams, D. Wright, and H. Yoshida, "Geant4 developments and applications," *IEEE Transactions on Nuclear Science*, vol. 53, pp. 270–278, Feb. 2006.

[97] U. Wahl, J. Correia, A. Czermak, S. Jahn, P. Jalocha, J. Marques, A. Rudge, F. Schopper, J. Soares, A. Vantomme, and P. Weilhammer, "Position-sensitive Si pad detectors for electron emission channeling experiments," *Nuclear Instruments and Methods in Physics Research Section A: Accelerators, Spectrometers, Detectors and Associated Equipment*, vol. 524, pp. 245–256, May 2004.

[98] L. M. C. Pereira, J. P. Araújo, M. J. Van Bael, K. Temst, and a. Vantomme, "Practical limits for detection of ferromagnetism using highly sensitive magnetometry techniques," *Journal of Physics D: Applied Physics*, vol. 44, p. 215001, June 2011.

[99] J. F. Ziegler, J. P. Biersack, and M. D. Ziegler, "SRIM, the stopping and range of ions in matter," Maryland, USA: Lulu Press, 2009.

[100] F. Máca and J. Mašek, "Electronic states in $Ga_{1-x}Mn_xAs$: Substitutional versus interstitial position of Mn," *Physical Review B*, vol. 65, p. 235209, June 2002.

[101] K. Edmonds, N. Farley, T. Johal, G. van der Laan, R. Campion, B. Gallagher, and C. Foxon, "Ferromagnetic moment and antiferromagnetic coupling in (Ga,Mn)As thin films," *Physical Review B*, vol. 71, p. 064418, Feb. 2005.

[102] M. Birowska, C. Śliwa, J. A. Majewski, and T. Dietl, "Origin of Bulk Uniaxial Anisotropy in Zinc-Blende Dilute Magnetic Semiconductors," *Physical Review Letters*, vol. 108, p. 237203, June 2012.

[103] M. Sawicki, F. Matsukura, A. Idziaszek, T. Dietl, G. Schott, C. Ruester, C. Gould, G. Karczewski, G. Schmidt, and L. Molenkamp, "Temperature dependent magnetic anisotropy in (Ga,Mn)As layers," *Physical Review B*, vol. 70, p. 245325, Dec. 2004.

[104] J.-L. Primus, H. Fritzsche, M. Malfait, M. J. Van Bael, J. De Boeck, and K. Temst, "Magnetic anisotropy and magnetization reversal in $Ga_{1-x}Mn_xAs$ layers studied by polarized neutron reflectometry," *Journal of Applied Physics*, vol. 97, no. 12, p. 123909, 2005.

[105] P. Korzhavyi, I. Abrikosov, E. Smirnova, L. Bergqvist, P. Mohn, R. Mathieu, P. Svedlindh, J. Sadowski, E. Isaev, Y. Vekilov, and O. Eriksson, "Defect-Induced Magnetic Structure in $(Ga_{1-x}Mn_x)As$," *Physical Review Letters*, vol. 88, p. 187202, Apr. 2002.

[106] R. E. Behringer, “Number of Single, Double, and Triple Clusters in a System Containing Two Types of Atoms,” *The Journal of Chemical Physics*, vol. 29, no. 3, p. 537, 1958.

[107] D. Mathiot and J. C. Pfister, “Dopant diffusion in silicon: A consistent view involving nonequilibrium defects,” *Journal of Applied Physics*, vol. 55, no. 10, p. 3518, 1984.

[108] A. N. Larsen, K. K. Larsen, P. E. Andersen, and B. G. Svensson, “Heavy doping effects in the diffusion of group IV and V impurities in silicon,” *Journal of Applied Physics*, vol. 73, no. 2, p. 691, 1993.

[109] S. J. Potashnik, K. C. Ku, S. H. Chun, J. J. Berry, N. Samarth, and P. Schiffer, “Effects of annealing time on defect-controlled ferromagnetism in $Ga_{1-x}Mn_xAs$,” *Applied Physics Letters*, vol. 79, no. 10, p. 1495, 2001.

[110] M. Moreno, B. Jenichen, V. Kaganer, W. Braun, A. Trampert, L. Däweritz, and K. Ploog, “MnAs nanoclusters embedded in GaAs studied by x-ray diffuse and coherent scattering,” *Physical Review B*, vol. 67, p. 235206, June 2003.

[111] T. Dietl and H. Ohno, “Ferromagnetic III–V and II–VI Semiconductors,” *MRS Bulletin*, vol. 28, pp. 714–719, Jan. 2011.

[112] T. Jungwirth, J. Sinova, A. H. MacDonald, B. L. Gallagher, V. Novák, K. W. Edmonds, A. W. Rushforth, R. P. Campion, C. T. Foxon, L. Eaves, E. Olejník, J. Mašek, S.-R. E. Yang, J. Wunderlich, C. Gould, L. W. Molenkamp, T. Dietl, and H. Ohno, “Character of states near the Fermi level in (Ga,Mn)As: Impurity to valence band crossover,” *Physical Review B*, vol. 76, p. 125206, Sept. 2007.

[113] A. Bonanni and T. Dietl, “A story of high-temperature ferromagnetism in semiconductors.,” *Chemical Society reviews*, vol. 39, pp. 528–39, Mar. 2010.

[114] H. G. Silva, H. L. Gomes, Y. G. Pogorelov, L. M. C. Pereira, G. N. Kakazei, J. B. Sousa, J. P. Araujo, J. F. L. Mariano, S. Cardoso, and P. P. Freitas, “Magnetic and transport properties of diluted granular multilayers,” *Journal of Applied Physics*, vol. 106, no. 11, p. 113910, 2009.